TIN-BISMUTH LOW TEMPERATURE SOLDER SYSTEMS - DEVELOPMENT AND FUNDAMENTAL UNDERSTANDING

by

Yaohui Fan

A Dissertation

Submitted to the Faculty of Purdue University

In Partial Fulfillment of the Requirements for the degree of

Doctor of Philosophy

School of Materials Engineering

West Lafayette, Indiana

August 2021

THE PURDUE UNIVERSITY GRADUATE SCHOOL

STATEMENT OF COMMITTEE APPROVAL

Dr. Carol A. Handwerker, Chair

School of Materials Engineering

Dr. John E. Blendell

School of Materials Engineering

Dr. Ganesh Subbarayan-Shastri

School of Mechanical Engineering

Dr. Eric P. Kvam

School of Materials Engineering

Approved by:

Dr. David F. Bahr

ACKNOWLEDGMENTS

The PhD study at Purdue University is an unforgettable experience in both scientific research and life. I really enjoyed my PhD life here because of the beautiful view and the good academic atmosphere on the campus, but also the kind the friendly people that I met here. II could not accomplish such achievements as well as this dissertation without the help and support of these people.

First and foremost, I would like to express my sincerest gratitude to my thesis advisor, Dr. Carol A. Handwerker for the continuous support of my PhD study and related research. During the last four years, Dr. Handwerker spent countless days and nights inspiring me for the research ideas, discussing and solving problems together with me, despite an incredibly busy schedule. Her keen insights and many years of professional experience made me become a professional and independent researcher in this area. She helped me not only in the academic areas, but also in many other ways, such as being a nice person, and try to be interactive with all the other experts in the academic field. She helped me out of the hardest time during the beginning of my PhD life. For me, she is not only my advisor, but also my dear friend for life. Without her I could not have this achievement now, she is no doubt the best advisor a student can have.

Besides my advisor, I would like to thank the rest of my thesis committee: Dr. John E. Blendell, Dr. Ganesh Subbarayan-Shastri and Dr. Eric P. Kvam for their kind help, insightful comments and encouragement throughout the last four years of my PhD study, also for the suggestions and inspirations which greatly widen my vision from many areas besides my main research focus.

My thanks also go to Dr. Nilesh U. Badwe, Dr. Raiyo F. Aspandiar and other colleagues from Intel Corporation, as well as Dr. Ranjit Pandher, Dr. Morgana Ribas, Dr. Carl Bilgrien and other colleagues from MacDermid Alpha for their funding and cooperation. During our collaboration since 2018, we spent a really nice time working together to push the frontier of low temperature soldering further, and they are always happy to help not only on the materials but on experiment consulting. I also gained a broader view and friendship with these experts in surface mount technology area thanks to their kind help on technical support and assistance in my research.

I was very luck to have developed the friendship with my colleagues and friends at Purdue University, from not only my research group, but also from School of Materials Engineering and

Mechanical Engineering. My special thanks to Dr. Thomas Reeve, Dr. John Holaday and Dr. Xianyi Hu who helped me make a good start and transition at the beginning of my PhD life. I also want to send my sincere acknowledgement to Dr. Travis Dale, Ms. Sukshitha Achar and Mr. Colin Greene for their collaboration and help on the mechanical testing for my thesis. I wish to express my deepest thanks to my friends in Materials Engineering, Mr. Duo Huang, Dr. Yifan Zhang, Dr. Jiaqi Li, Dr. Chengzi Huang for their encouragement and help during my PhD life. I also want to thank my group members: Dr. David Lowing, Dr. Matthew Michie, Dr. Joseph Andler, Ms. Elizabeth Mcclamrock, Dr. Xi Chen, Ms. Alyssa Yaeger, Mr. Ruwen Zheng, Ms. Ziyun Huang, Mr. Yifan Wu, Ms. Congying Wang, Ms. Hannah Fowler, Mr. John Obamedo, Ms. Anna Murrayfor providing me with technical support and assistance in my research. Their companionship has made my life in Purdue an enjoyable and memorable one.

I save my final thanks for my family. I am very grateful to my parents Mr. Jili Fan and Ms. Zhong Liu, my girlfriend Ms. Han Zhao, and again my advisor Dr. Carol A. Handwerker for their endless love, understanding, encouragement and support. During my five years of study at Purdue University, I experienced difficulties and wrinkles in my life. I was once depressed and afraid to embrace the unknown future during the flow of time. But all of you encouraged me and pulled me out of my most difficult times at the beginning of my PhD life. Your support and love became my sword and shield, and because of you, I started to make fine achievements in not only academia but also my daily life. I started to be confident and strong for the difficulties and waves in my life. Thanks to you, I had an irreplaceable memory here. And I am really happy to devote the best period of my life pursuing things I truly love and with the people I truly care.

TABLE OF CONTENTS

LIST OF TABLES 8
LIST OF FIGURES 9
LIST OF ABBREVIATIONS 15
ABSTRACT 16
1. A MODEL STUDY OF MICROSTRUCTURE EVOLUTION AND BI DIFFUSION IN SN-BI LOW TEMPERATURE SOLDERING SYSTEMS 18
1.1 Abstract 18
1.2 Introduction 18
1.3 Experimental 23
1.4 Results and Discussion 24
1.4.1 Thermodynamic model simulation of Sn-Bi system 24
1.4.2 Microstructure evolution during two-phase annealing 25
1.4.3 Phase transformation during two-phase annealing 31
1.4.4 Bi segregation model establishment 34
1.5 Conclusions 35
1.6 Acknowledgment 36
1.7 References 36
1.8 Appendix 38
2. INFLUENCE OF PAD SURFACE FINISH ON THE MICROSTRUCTURE EVOLUTION AND INTERMETALLIC COMPOUND GROWTH IN HOMOGENEOUS TIN-BISMUTH AND TIN-BISMUTH-SILVER SOLDER INTERCONNECTS 40
2.1 Abstract 40
2.2 Introduction 40
2.3 Experimental 44
2.4 Results and Discussion 47
2.4.1 Thermodynamic Calculations of Intermetallic Compound Growth during Reflow/Solidification and Solid-state Annealing 47
Sn-58Bi and Sn-57Bi-1Ag on Cu-OSP 47
Sn-58Bi and Sn-57Bi-1Ag on ENIG 47

Sn-58Bi and Sn-57Bi-1Ag on ENIG (one side) and Cu-OSP (other side) 48
2.4.2 Microstructure Evolution Experiments 49
Sn-58Bi and Sn-57Bi-1Ag on Cu-OSP 49
Sn-58Bi and Sn-57Bi-1Ag on ENIG 50
2.4.3 Ag_3Sn Effect on Interfacial Intermetallic Growth Rate and Bi Coarsening for Sn-Bi Solders 55
2.4.4 Mechanical Characterization and Gold Embrittlement Effect in Sn-58Bi and Sn-57Bi-1Ag Solder Interconnects on ENIG 57
2.4.5 Elimination of $(Ni,Au)Sn_4$ Formation in Sn-58Bi and Sn-57Bi-1Ag Solder Interconnects 61
2.4.6 Intermetallic Compound Growth Rate Calculation for Sn-58Bi and Sn-57Bi-1Ag Solder Interconnects 61
2.5 Conclusions 64
2.6 Acknowledgment 65
2.7 References 65
2.8 Appendix 70
3. MICROALLOYING EFFECTS ON INTERMETALLIC COMPOUND GROWTH AND MECHANICAL RELIABILITY OF TIN-BISMUTH SOLDER JOINTS 72
3.1 Abstract 72
3.2 Introduction 72
3.3 Experimental 77
3.4 Results and Discussion 79
3.4.1 Thermodynamic Calculations of Intermetallic Compound Growth during Reflow/Solidification and Solid-state Annealing 79
Intermetallic Compounds in SnBiSb, SnBiCu and SnBiIn 80
SnBiSb, SnBiCu and SnBiIn on Cu-OSP 80
SnBiSb, SnBiCu and SnBiIn on ENIG 80
3.4.2 Microstructure Coarsening of SnBiSb, SnBiCu and SnBiIn during Aging 81
3.4.3 Intermetallic Compound Growth of SnBiSb, SnBiCu and SnBiIn on Cu-OSP 84
3.4.4 Intermetallic Compound Growth of SnBiSb, SnBiCu and SnBiIn on ENIG 87
3.4.5 Mechanical Characterization & Failure Analysis of SnBiSb, SnBiCu Joints 90

3.5 Conclusions 94
3.6 Acknowledgment 95
3.7 References 95
3.8 Appendix 100
4. MICROALLOYING EFFECTS ON INTERMETALLIC COMPOUND GROWTH AND MECHANICAL RELIABILITY OF TIN-BISMUTH SOLDER JOINTS 102
4.1 Abstract 102
4.2 Introduction 102
4.3 Experimental 106
4.4 Results and Discussion 109
4.4.1 Thermodynamic Calculations of HRL1 Solder 109
4.4.2 Microstructure Evolution of Hybrid Systems during Reflow 110
4.4.3 Bi Diffusion and Sn Grain Growth in Hybrid Assemblies during Solid-State Aging 111
4.4.4 Intermetallic Compound Growth on ENIG Surface Finish of Homogeneous Joints during Reflow 115
4.4.5 Mechanical Characterization in Homogeneous Interconnects on ENIG & OSP Surface Finishes 117
4.5 Conclusions 121
4.6 Acknowledgment 122
4.7 References 122
PUBLICATIONS 127

LIST OF TABLES

Table 1.1. EDS results of Bi composition in different areas of Sn-Bi solder system after annealing 30

Table 2.1. Intermetallic compound layer thickness in Sn-57Bi-1Ag joints during aging on different sides..... 56

Table 2.2. Summary of intermetallic growth rate constants for Sn-58Bi and Sn-57Bi-1Ag solders on Cu-OSP surface finish with different configurations at 125°C 64

Table 2.3. Summary of intermetallic growth rate constants for Sn-58Bi and Sn-57Bi-1Ag solders on ENIG surface finish with different configurations at 125°C 64

LIST OF FIGURES

Figure 1.1. Schematic illustration of component warpage and different defects formed during reflow soldering 19

Figure 1.2. a) A schematic illustration of hybrid joints before reflow, where Sn-Bi LTS paste replaces Sn-Ag-Cu solder paste during surface mount procedure; b) typical microstructure of a Sn-Bi LTS-Sn-Ag-Cu hybrid joint after reflow showing the Bi diffusion region and the un-melted Sn-Ag-Cu solder ball region 20

Figure 1.3. a) A schematic illustration of Sn-Bi homogeneous joints before reflow, where Sn-Bi LTS paste substitutes both Sn-Ag-Cu solder paste and Sn-Ag-Cu solder ball during surface mount procedure; b) microstructure of a Sn-57Bi-1Ag homogeneous joint after reflow 20

Figure 1.4. (a) A schematic illustration of TLPS process where overall Bi composition falls into binary phase region during isothermal hold; (b) a conceptual model of TLPS in Sn-Bi solder paste at high-Bi content area; (c) close look of radial concentration gradient of Bi precipitates in non-equilibrium situation 22

Figure 1.5. Volume fraction of liquid in Sn-30Bi mixture during equilibrium at different annealing temperatures 24

Figure 1.6. Stable phases in Sn-30Bi mixtures at different annealing temperatures 25

Figure 1.7. Backscattered SEM pictures for Sn-30 wt.%Bi samples heated to 145°C and then cooled down to room temperature at different rates with (a) air quench, and (b) 10°C/min cooling rate 27

Figure 1.8. Microstructure of Sn-30 wt.% Bi samples annealed at 165°C for (a) 0 min; (b) 5 min; (c) 60 min; and (d) 240 min 28

Figure 1.9. Microstructure and Sn orientation structures of Sn-30 wt.% Bi samples heated to 145°C with (a, b) air quench with no isothermal hold; and (c, d) cooled down with 10°C/min with no isothermal hold; and Sn-30 wt.% Bi samples heated to 165°C and then cooled down with 10°C/min with the isothermal hold time of (e, f) 0 min; (g, h) 5 min; (i, j) 60min; and (k, l) 240 min 28

Figure 1.10. DSC traces of Sn-30 wt.% Bi Sn-Bi mixture held at 165°C for 5 minutes 31

Figure 1.11. (a) Schematic illustration on Sn-Bi phase diagram showing higher isothermal hold temperature results in lower Bi solubility in Sn and lower precipitation temperature during cooling; (b) the linear relationship between Bi precipitation temperature and isothermal hold temperature; (c) the linear relationship between Bi precipitation temperature and corresponding solvus temperature 32

Figure 1.12. The remaining volume fraction of liquid in Sn-30 wt.% Bi samples after different annealing time at 165°C, showing increasing amount of liquid during annealing process 33

Figure 1.13. Bi composition change in Sn solid solution during annealing process due to Bi segregation at Sn grain boundaries 35

Figure 1.14. DSC traces of (a) Sn-10 wt.% Sn-Bi mixture; (b) Sn-20 wt.% Sn-Bi mixture; (c) Sn-30 wt.% Bi Sn-Bi mixture; and (d) Sn-40 wt.% Bi Sn-Bi mixture held at peak temperature for 5 minutes 39

Figure 2.1. Schematic illustration of component warpage and different defects formed during reflow soldering 41

Figure 2.2. a) A schematic illustration of hybrid joints before reflow, where Sn-Bi LTS paste replaces Sn-Ag-Cu solder paste during surface mount procedure; b) typical microstructure of a Sn-Bi LTS-Sn-Ag-Cu hybrid joint after reflow showing the Bi diffusion region and the un-melted Sn-Ag-Cu solder ball region 42

Figure 2.3. a) A schematic illustration of Sn-Bi homogeneous joints before reflow, where Sn-Bi LTS paste substitutes both Sn-Ag-Cu solder paste and Sn-Ag-Cu solder ball during surface mount procedure; b) microstructure of a Sn-57Bi-1Ag homogeneous joint after reflow 42

Figure 2.4. Schematic illustration of a) Sn-58Bi and Sn-57Bi-1Ag solder test specimens with 730 μm diameter pads arranged in a 7 x 7, 1.27 mm pitch grid. The eight red circles indicate the locations of the solder joints in the top view of the printed circuit board (top). Schematic cross section of an assembled single solder joint (bottom); and b) schematic illustration of the mechanical tester for shear testing 46

Figure 2.5. Microstructures of Sn-58Bi/Cu interface of Cu-OSP/Sn-58Bi/Cu-OSP a) after reflow and b) after 250 h of solid-state annealing at 125˚C. and Sn-57Bi-1Ag/Cu interface of Cu-OSP/Sn-57Bi-1Ag/Cu-OSP c) after reflow and d) after 250 h of solid-state annealing at 125˚C 49

Figure 2.6. Intermetallic compound layer thickness as a function of annealing time at 125°C for Sn-58Bi and Sn-57Bi-1Ag solders on boards with Cu-OSP- Cu-OSP and Cu-OSP-ENIG surface finishes 50

Figure 2.7. Microstructure after reflow of interfacial intermetallic layers for a) ENIG/Sn-58Bi/ENIG; b) ENIG/Sn-57Bi-1Ag/ENIG; and microstructure in the bulk solder showing AuSn4 for c) ENIG/Sn-58Bi/ENIG; and d) ENIG/Sn-57Bi-1Ag/ENIG 51

Figure 2.8. Microstructures after solid state annealing at 125˚C: a) ENIG/Sn-58Bi/ENIG after 75 h annealing; b) higher magnification image of a); c) ENIG/Sn-58Bi/ENIG after 250 h annealing; d) higher magnification image of c). Higher magnification images of interfacial layer structures of ENIG/Sn-58Bi/ENIG solder interconnects showing Bi wetting along $(Ni,Au)Sn_4$ grain boundaries after e) 75 h annealing and f) 250 h annealing 52

Figure 2.9. 3D x-ray microscope images of ENIG/Sn-58Bi/ENIG solder joint after annealing at 125°C, a) a cross-section of the solder interconnect showing large voids (black regions) formed inside the $(Ni,Au)Sn_4$ during annealing; b) 3-D reconstruction of the solder joint, with the large voids formed inside the $(Ni,Au)Sn_4$ shown in orange 53

Figure 2.10. Microstructure of Sn-57Bi-1Ag-Ni interface of ENIG-Sn-57Bi-1Ag-ENIG after annealing at 125˚C for a) 75 h and b) 250 h 53

Figure 2.11. Theoretical $(Ni_{1-x}Au_x)Sn_4$ layer thickness as a function of x, the Au fraction, The top dotted line is the observed thickness after 250h aging of Sn-58Bi on ENIG at 125˚C; the bottom dotted line is for Sn-57Bi-1Ag on ENIG for the same conditions 54

Figure 2.12. Microstructure of a) Cu- OSP-Sn-57Bi-1Ag- Cu-OSP solder joint after reflow showing Ag_3Sn segregation on one side of the joint; and b) ENIG-Sn-57Bi-1Ag-ENIG solder joint after reflow showing Ag_3Sn segregation on one side of the joint..... 56

Figure 2.13. Microstructure of coarsened eutectic Bi inside a) Cu-OSP-Sn-58Bi- Cu-OSP; b) Cu-OSP-Sn-58Bi- Cu-OSP; c) ENIG-Sn-57Bi-1Ag-ENIG; and d) ENIG-Sn-57Bi-1Ag-ENIG solder interconnects after 250 hours of aging at 125°C..... 57

Figure 2.14. Microstructure of a) fatigue-loaded ENIG/Sn-58Bi/ENIG solder interconnects after 250h of solid-state annealing; b) higher magnification image at Sn-58Bi/Ni interface of a) showing the details of the fracture path; c) fatigue-tested ENIG/Sn-57Bi-1Ag/ENIG solder interconnects after 250h of solid-state annealing; and d) higher magnification image at Sn-57Bi-1Ag/Ni interface of c) showing the details of the fracture surface..... 58

Figure 2.15. Stress-strain curves of first fatigue loading cycle of ENIG/Sn-58Bi/ENIG and ENIG/Sn-57Bi-1Ag/ENIG solder joints after both reflow and 250 h of aging at 125°C..... 59

Figure 2.16. Microstructure of fractured solder interconnects after fatigue testing: a) Cu-OSP/Sn-58Bi/Cu-OSP after reflow; b) Cu-OSP/Sn-58Bi/Cu-OSP after 250 h aging at 125°C; c) Cu-OSP/Sn-57Bi-1Ag/Cu-OSP after reflow; and d) Cu-OSP/Sn-57Bi-1Ag/Cu-OSP after 250 h aging at 125°C..... 60

Figure 2.17. Fatigue reliability and N_{50} cycles for Sn-58Bi, Sn-57Bi-1Ag and Sn3.0Ag0.5Cu after reflow and 250 h of aging at 125˚C on a) ENIG and b) Cu-OSP surface finishes..... 60

Figure 2.18. Microstructures at a) Sn-58Bi/Ni interface of ENIG/Sn-58Bi/Cu/OSP solder joints after reflow; b) Sn-58Bi/Ni interface of ENIG/Sn-58Bi/Cu-OSP solder interconnects after 250 h of annealing at 125˚C; c) Sn-57Bi-1Ag-Ni interface of ENIG/Sn-57Bi-1Ag/Cu-OSP solder interconnects after reflow; and d) Sn-57Bi-1Ag-Ni interface of ENIG/Sn-57Bi-1Ag/Cu-OSP solder interconnects after 250 h of at 125˚C..... 62

Figure 2.19. Intermetallic compound layer thickness change during solid-state annealing (125°C) for a) Sn-58Bi and Sn-57Bi-1Ag solders on ENIG surface finishes under different configurations, and b) enlarged lower part of Figure 2.19a)..... 63

Figure 2.20. Isothermal sections of Sn-Bi-Cu ternary system during a) reflow (180°C), and b) solid-state annealing (125°C) showing possible intermetallic phases formation during either process..... 70

Figure 2.21. Isothermal sections of Sn-Bi-Ni ternary system during a) reflow (180°C), and b) solid-state annealing (125°C) showing possible intermetallic phases formation during either process 71

Figure 2.22. Isothermal sections of Sn-Ni-Au ternary system during a) reflow (180°C), and b) solid-state annealing (125°C) showing possible intermetallic phases formation during either process..... 71

Figure 3.1. Schematic illustration of component warpage and different defects formed during reflow soldering..... 73

Figure 3.2. a) A schematic illustration of hybrid joints before reflow, when Sn-Bi LTS pastes substitutes SAC solder paste during surface mount procedure; b) typical microstructure of a LTS-SAC hybrid joint after reflow showing the Bi diffusion region and the un-melted SAC region . 74

Figure 3.3. a) A schematic illustration of Sn-Bi homogeneous joints before reflow, when Sn-Bi LTS pastes substitutes both SAC solder paste and SAC BGA during surface mount procedure; b) microstructure of a Sn57Bi1Ag homogeneous joint after reflow 74

Figure 3.4. Schematic illustration of SnBi low temperature solder test specimens. The eight red circles indicate the locations of the solder joints in the top view of the printed circuit board (top). The cross section of an assembled single solder joint (bottom) 78

Figure 3.5. Microstructure of a) Sn58Bi after reflow; b) Sn58Bi after 250 hours of aging at 125°C; c) Sn58BiSbNi after reflow; d) Sn58BiSbNi after 250 hours of aging at 125°C; e) Sn40BiCuNi after reflow; f) Sn40BiCuNi after 250 hours of aging at 125°C; g) Sn56.5Bi0.5In after reflow; and h) Sn56.5Bi0.5In after 250 hours of aging at 125°C 82

Figure 3.6. EDS mapping of a) Sn58BiSbNi after reflow and b) Sn56.5Bi0.5In after reflow showing Sb and In distribution in Sn 83

Figure 3.7. Microstructure of solder-Cu interface of intermetallic layers of OSP-Sn58BiSbNi-OSP solder interconnects a) after reflow and b) after 250 hours of solid-state annealing at 125°C. OSP-Sn40BiCuNi-OSP solder interconnects c) after reflow and d) after 250 hours of solid-state annealing at 125°C. OSP-Sn56.5Bi0.5In-OSP solder interconnects e) after reflow and f) after 250 hours of solid-state annealing at 125°C 85

Figure 3.8. Intermetallic compound layer thickness change for Sn58Bi, Sn58BiSbNi, Sn40BiCuNi and Sn56.5Bi0.5In solders on OSP surface finish during solid state annealing at a) 85°C and b) 125°C 86

Figure 3.9. Microstructure of a) solder-Ni interface of intermetallic layers of ENIG-Sn58BiSbNi-ENIG solder interconnects after reflow; b) solder-Ni interface of intermetallic layers of ENIG-Sn58BiSbNi-ENIG solder interconnects after 250 hours of solid-state annealing at 125°C; c) solder-Ni interface of ENIG-Sn40BiCuNi-ENIG solder interconnects after reflow; d) solder-Ni interface of ENIG-Sn40BiCuNi-ENIG solder interconnects after 250 hours of solid-state annealing at 125°C; e) solder-Ni interface of intermetallic layers of ENIG-Sn56.5Bi0.5In-ENIG solder interconnects after reflow; and f) solder-Ni interface of intermetallic layers of ENIG-Sn56.5Bi0.5In-ENIG solder interconnects after 250 hours of solid-state annealing at 125°C..... 88

Figure 3.10. Microstructure of a) solder-Ni interface of intermetallic layers of ENIG-Sn58BiSbNi-ENIG solder interconnects after 250 hours of solid-state annealing at 85°C and b) solder-Ni interface of intermetallic layers of ENIG-Sn58BiSbNi-ENIG solder interconnects after 250 hours of solid-state annealing at 85°C followed by 2 months of storage at -10°C, which caused the formation of the (Au,Ni)Sn_4 layer 89

Figure 3.11. Intermetallic compound layer thickness change for Sn58Bi, Sn58BiSbNi, Sn40BiCuNi and Sn56.5Bi0.5In solders on ENIG surface finish during solid state annealing at a) 85°C and b) 125°C 89

Figure 3.12. Microstructure of a) fatigue-loaded OSP-Sn58BiSbNi-OSP solder interconnects after reflow; b) higher magnification image at solder-Cu interface of a) showing the details of fractures; c) fatigue-loaded OSP-Sn58BiSbNi-OSP solder interconnects after 250°C of solid-state annealing; and d) higher magnification image at solder-Cu interface of c) showing the details of fractures; e) fatigue-loaded OSP-Sn40BiCuNi-OSP solder interconnects after reflow; f) higher magnification

image at solder-Cu interface of e) showing the details of fractures; g) fatigue-loaded OSP-Sn40BiCuNi-OSP solder interconnects after 250°C of solid-state annealing; and h) higher magnification image at solder-Cu interface of g) showing the details of fractures 91

Figure 3.13. Microstructure of a) fatigue-loaded ENIG-Sn58BiSbNi-ENIG solder interconnects after reflow; b) higher magnification image at solder-Ni interface of a) showing the details of fractures; c) fatigue-loaded ENIG-Sn58BiSbNi-ENIG solder interconnects after 250°C of solid-state annealing; and d) higher magnification image at solder-Ni interface of c) showing the details of fractures; e) fatigue-loaded ENIG-Sn40BiCuNi-ENIG solder interconnects after reflow; f) higher magnification image at solder-Ni interface of e) showing the details of fractures; g) fatigue-loaded ENIG-Sn40BiCuNi-ENIG solder interconnects after 250°C of solid-state annealing; and h) higher magnification image at solder-Ni interface of g) showing the details of fractures 93

Figure 3.14. Fatigue reliability and N_{50} cycles for Sn58Bi, Sn57Bi1Ag, Sn3.0Ag0.5Cu, Sn58BiSbNi and Sn40BiCuNi after reflow and 250 hours of aging at 125°C on a) OSP and b) ENIG surface finishes 94

Figure 3.15. Thermodynamic simulation of phases at equilibrium in a) Sn58BiSbNi; b) Sn40BiCuNi and c) Sn56.5Bi0.5In..... 100

Figure 4.1. Schematic illustration of component warpage and different defects formed during reflow soldering 103

Figure 4.2. a) A schematic illustration of hybrid joints before reflow, when Sn-Bi LTS pastes substitutes SAC solder paste during surface mount procedure; b) typical microstructure of a LTS-SAC hybrid joint after reflow showing the Bi diffusion region and the un-melted SAC region 104

Figure 4.3. a) A schematic illustration of Sn-Bi homogeneous joints before reflow, when Sn-Bi LTS pastes substitutes both SAC solder paste and SAC BGA during surface mount procedure; b) microstructure of a Sn57Bi1Ag homogeneous joint after reflow 104

Figure 4.4. Schematic illustration of Sn-58Bi and Sn-57Bi-1Ag solder test specimens. The eight red circles indicate the locations of the solder joints in the top view of the printed circuit board (top). The cross section of an assembled single solder joint (bottom)..... 109

Figure 4.5. Solidification path simulation of a) Sn57.6Bi0.4Ag and b) HRL1 from 20°C to 200°C 110

Figure 4.6. Microstructure of a) Sn57.6Bi0.4Ag/Sn0.7Cu solder paste mixtures annealed at 165°C for 0 minute; b) Sn57.6Bi0.4Ag/Sn0.7Cu solder paste mixtures annealed at 165°C for 4 hours; c) HRL1/Sn0.7Cu solder paste mixtures annealed at 165°C for 0 minute and d) HRL1/Sn0.7Cu solder paste mixtures annealed at 165°C for 4 hours 111

Figure 4.7. Microstructure of a) Cu-Sn58Bi-SAC305 hybrid assemblies after reflow; b) Cu-Sn58Bi-SAC305 hybrid assemblies after 1 week of aging at 125°C; c) Cu-HRL1-SAC305 hybrid assemblies after reflow and d) Cu-HRL1-SAC305 hybrid assemblies after 1 week of aging at 125°C 112

Figure 4.8. Microstructure of Bi diffusion front in a) Cu-Sn58Bi-SAC305 and b) Cu-HRL1-SAC305 hybrid assemblies after 1 week of aging at 125°C..... 113

Figure 4.9. a) Microstructure of Bi diffusion front in Cu-Sn58Bi-SAC305 hybrid assemblies after 1 week of aging at 125°C; b) tin EBSD map of a); c) microstructure of Bi diffusion front in Cu-HRL1-SAC305 hybrid assemblies after 1 week of aging at 125°C; d) tin EBSD map of c); e) microstructure of Bi diffusion front in Cu-Sn58Bi-SAC305 hybrid assemblies after 1500 hours of aging at 125°C; f) tin EBSD map of e); g) microstructure of Bi diffusion front in Cu-HRL1-SAC305 hybrid assemblies after 1500 hours of aging at 125°C and h) tin EBSD map of g) 114

Figure 4.10. Microstructure of a) solder-Ni interface of intermetallic layers of ENIG-Sn58Bi-ENIG solder interconnects after reflow; b) solder-Ni interface of intermetallic layers of ENIG-Sn58Bi-ENIG solder interconnects after 250 hours of solid-state annealing at 125°C; c) solder-Ni interface of ENIG-Sn57Bi1Ag-ENIG solder interconnects after reflow; d) solder-Ni interface of ENIG-Sn57Bi1Ag-ENIG solder interconnects after 250 hours of solid-state annealing at 125°C; e) solder-Ni interface of intermetallic layers of ENIG-HRL1-ENIG solder interconnects after reflow and f) solder-Ni interface of intermetallic layers of ENIG-HRL1-ENIG solder interconnects after 250 hours of solid-state annealing at 125°C 116

Figure 4.11. Microstructure of a) fatigue-loaded ENIG-Sn58Bi-ENIG solder interconnects after 250°C of solid-state annealing; b) higher magnification image at Sn58Bi-Ni interface of a) showing the details of fractures; c) fatigue-loaded ENIG-Sn57Bi1Ag-ENIG solder interconnects after 250°C of solid-state annealing; and d) higher magnification image at Sn57Bi1Ag-Ni interface of c) showing the details of fractures 118

Figure 4.12. Microstructure of fractured a) ENIG-HRL1-ENIG joint after reflow and b) ENIG-HRL1-ENIG joint after 250 hours aging at 125°C 118

Figure 4.13. Microstructure of fractured a) OSP-Sn58Bi-OSP after reflow; b) OSP-Sn58Bi-OSP after 250 hours aging at 125°C; c) OSP-Sn57Bi1Ag-OSP after reflow; d) OSP-Sn57Bi1Ag-OSP after 250 hours aging at 125°C solder interconnects after fatigue testing; e) OSP-HRL1-OSP after reflow and f) OSP-HRL1-OSP after 250 hours aging at 125°C 120

Figure 4.14. Fatigue reliability and N_{50} cycles for Sn58Bi, Sn57Bi1Ag and HRL1 on ENIG and OSP surface finishes after a) reflow and b) 250 hours of aging at 125°C 121

LIST OF ABBREVIATIONS

Sn: tin

Bi: bismuth

Cu: copper

Ag: silver

Au: gold

Ni: nickel

LTS: low temperature soldering

OSP: organic surface protection, or organic solderability preservative

ENIG: electroless nickel immersion gold

SAC: tin-silver-copper alloy

SAC305: a tin-silver-copper alloy containing 3.0wt% of silver, 0.5% of copper and the rest tin

ABSTRACT

Low reflow temperature solder interconnect technology based on Sn-Bi alloys is currently being considered as an alternative for Sn-Ag-Cu solder alloys to form solder interconnects at significantly lower melting temperatures than required for Sn-Ag-Cu alloys.

A new low temperature interconnect technology based on Sn-Bi alloys is being considered for attaching Sn-Ag-Cu (SAC) solder BGAs to circuit boards at temperatures significantly lower than for homogeneous SAC joints. Microstructure development studies of reflow and annealing, including Bi diffusion and precipitation, are important in understanding mechanical reliability and failures paths in the resulting heterogeneous joints. Experiments in several SAC-SnBi geometries revealed that Bi concentration profiles deviate from local equilibrium expected from the phase diagram, with much higher local concentrations and lower volume fractions of liquid than expected during short-time high temperature anneals in the two-phase region. As annealing time increased and Sn grain coarsening occurred, the compositions and fractions revert to the phase diagram, suggesting an "anti-Scheil" effect. A Bi interface segregation model based on Bi segregation at Sn grain boundaries was developed to explain the Bi distribution characteristics in Sn during two-phase annealing process.

Besides hybrid joints, microstructural evolution after reflow and aging, especially of intermetallic compound (IMC) growth at solder/pad surface finish interfaces in homogeneous SnBi LTS joints, is also important to understanding fatigue life and crack paths in the solder joints. This study describes intermetallic growth in homogeneous solder joints of Sn-Bi eutectic alloy and Sn-Bi-Ag alloys formed with electroless nickel-immersion gold (ENIG) and Cu-organic surface protection (Cu-OSP) surface finishes. Experimental observations revealed that, during solid state annealing following reflow, the 50nm Au from the ENIG surface finish catalyzed rapid $(Au,Ni)Sn_4$ intermetallic growth at the Ni-solder interface in both Sn-Bi and Sn-Bi-Ag homogeneous joints, which led to significant solder joint embrittlement during fatigue testing. Further study found that the growth rate of $(Au,Ni)Sn_4$ intermetallic could be reduced by In and Sb alloying of SnBi solders and is totally eliminated with Cu addition. Fatigue testing revealed Au embrittlement is always present in solder joints without Cu, even with In and Sb additions due to $(Au,Ni)Sn_4$ formation. The fatigue reliability of Cu-containing alloys is better on ENIG due to the formation of $(Ni,Cu,Au)_6Sn_5$ at the solder-surface finish interface instead of $(Au,Ni)Sn_4$.

With the development of SnBi LTSs, a new generation alloy called HRL1 stands out for its outstanding reliability during thermal cycling and drop shock testing. This study focused on microstructure evolution in SnBi eutectic, SnBiAg eutectic and HRL1 solders (MacDermid Alpha) homogeneous joints and hybrid joints with SAC305 formed with ENIG and Cu-OSP surface finishes. Experimental results revealed that with more microalloying elements, HRL1 has significantly refined microstructure and slower Sn grain growth rate during solid-state aging compared with SnBi and SnBiAg eutectic alloys. Intermetallic compound growth study showed that during solid state annealing following reflow, the (50nm) Au from the ENIG finish catalyzed rapid $(Au,Ni)Sn_4$ intermetallic growth at the Ni-solder interface in both Sn-Bi and Sn-Bi-Ag homogeneous joints, which led to significant solder joint embrittlement during creep and fatigue loading. However, $(Au,Ni)Sn_4$ growth and gold embrittlement was completely eliminated for HRL1 due to Cu additions in it, and HRL1 has significantly better fatigue reliability than SnBi and SnBiAg eutectic alloys on both OSP and ENIG surface finishes.

1. A MODEL STUDY OF MICROSTRUCTURE EVOLUTION AND BI DIFFUSION IN SN-BI LOW TEMPERATURE SOLDERING SYSTEMS

1.1 Abstract

A new low temperature interconnect technology based on Sn-Bi alloys is being considered for attaching Sn-Ag-Cu (SAC) solder BGAs to circuit boards at temperatures significantly lower than for homogeneous SAC joints. Microstructure development studies of reflow and annealing, including Bi diffusion and precipitation, are important in understanding mechanical reliability and failures paths in the resulting heterogeneous joints. Experiments in several SAC-SnBi geometries revealed that Bi concentration profiles deviate from local equilibrium expected from the phase diagram, with much higher local concentrations and lower volume fractions of liquid than expected during short-time high temperature anneals in the two-phase region. As annealing time increased and Sn grain coarsening occurred, the compositions and fractions revert to the phase diagram, suggesting an "anti-Scheil" effect. A Bi interface segregation model based on Bi segregation at Sn grain boundaries was developed to explain the Bi distribution characteristics in Sn during two-phase annealing process.

Keywords: Low temperature soldering, tin-bismuth system, microstructure evolution, diffusion model

1.2 Introduction

Three-dimensional (3D) packaging technologies, specifically, large area Heterogeneously Integrated System-in Package (SIP) technologies, are critical for achieving modern high performance, high bandwidth systems [1]. As these SIPs grow in area, warpage of the substrates leading to either solder joint bridging (short circuit) or gaps (open circuit) becomes a significant reliability concern [2]. Since the extent of warpage is directly proportional to solder reflow temperature, there is a need to reduce the peak reflow temperature by using alternative "low temperature" solder alloys. Tin-silver-copper (SAC) alloys, the industry standard, require peak reflow temperatures of approximately 240°C due to their high eutectic temperature (217°C). Such high reflow temperatures have been observed to cause serious warpage-induced defects, such as separation of SAC solder balls from SAC solder paste before melting (217°C) to form head-on-

pillow (HoP) defects along the edges of the IC and bridging in the center [3,4]. A schematic illustration of chip warpage and some of the resulting defects are shown in Figure 1.1. In HoP, the connections between solder on the board side and the ball are weak, based only on Van der Waals forces. Therefore, when the component encounters large thermal or mechanical stresses during use, HoP defects can cause electrical failure in the component [5]. Solder joints in the center of the packaging may also form bridging defects, which could cause short circuit and component failure.

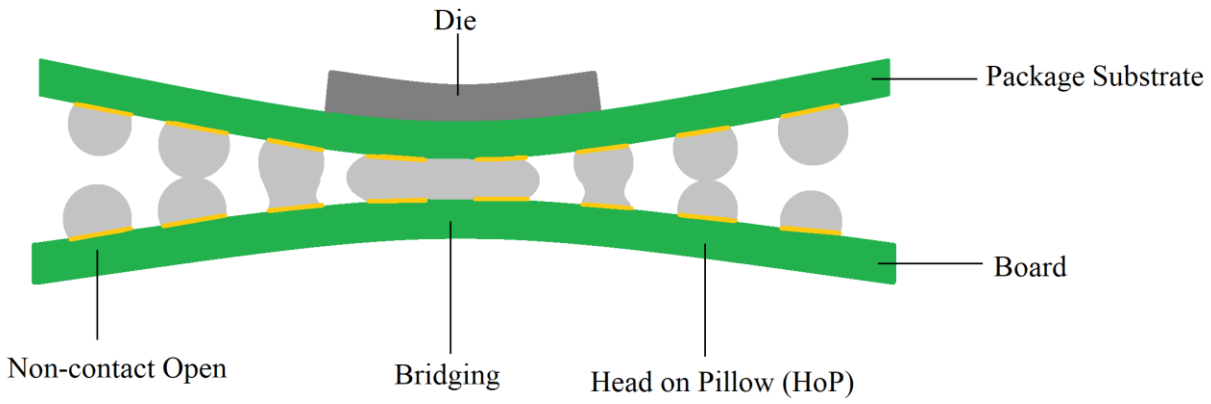

Figure 1.1. Schematic illustration of component warpage and different defects formed during reflow soldering

As a result, low temperature soldering (LTS) systems have been recommended as a solution to reduce heating-induced warpage [6-13]. Solders based on eutectic Sn-Bi alloys are popular candidates for low temperature soldering due to their low eutectic temperature [14], as well as low cost and toxicity. Two different use modes of the low-temperature Sn-Bi alloys are being considered: (1) Sn-Bi alloy solder paste used instead of Sn-Ag-Cu solder paste to assemble components with Sn-Ag-Cu solder balls to form "hybrid" joints after soldering, as shown in Figure 1.2 and (2) both the ball and the paste are Sn-Bi alloys to form homogeneous joints after reflow, as shown in Figure 1.3. For both use modes, assembly necessitates initial balling of the component, followed by melting of Sn-Bi alloy pastes to attach the component to the board. For the Sn-Bi eutectic alloy with a eutectic melting temperature of 139°C, a reflow temperature of approximately 160-190°C is required, lowering the peak reflow temperature by 50-80°C relative to the Sn-Ag-Cu alloy reflow.

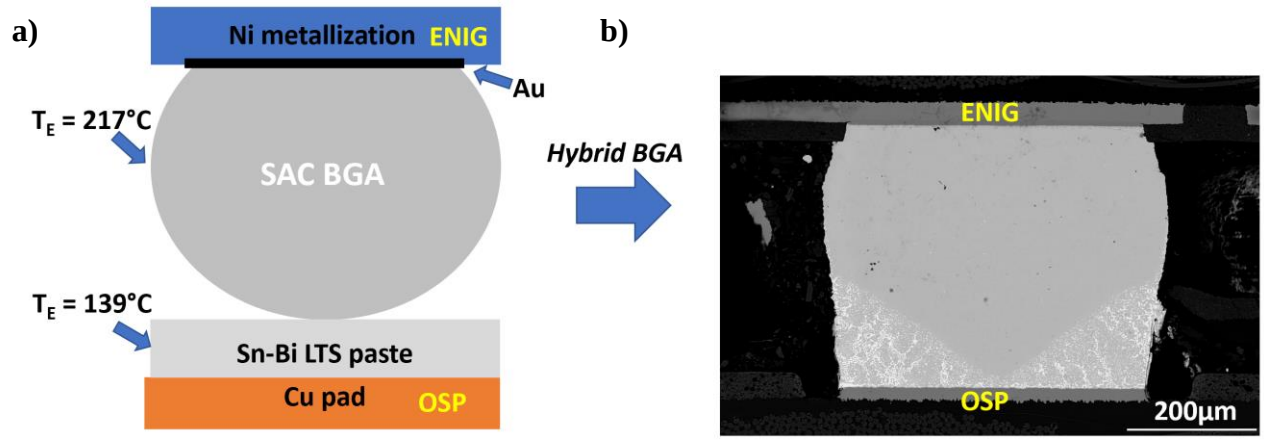

Figure 1.2. a) A schematic illustration of hybrid joints before reflow, where Sn-Bi LTS paste replaces Sn-Ag-Cu solder paste during surface mount procedure; b) typical microstructure of a Sn-Bi LTS-Sn-Ag-Cu hybrid joint after reflow showing the Bi diffusion region and the un-melted Sn-Ag-Cu solder ball region

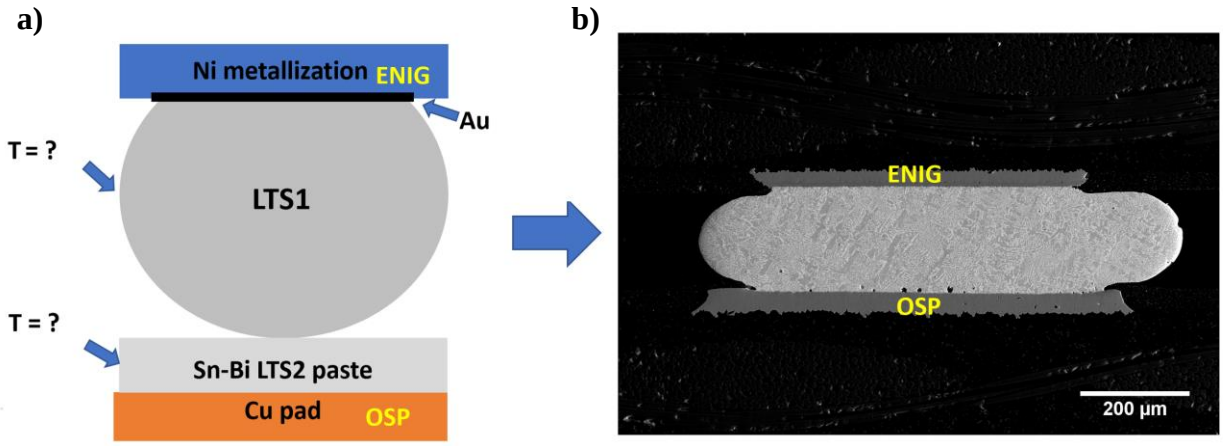

Figure 1.3. a) A schematic illustration of Sn-Bi homogeneous joints before reflow, where Sn-Bi LTS paste substitutes both Sn-Ag-Cu solder paste and Sn-Ag-Cu solder ball during surface mount procedure; b) microstructure of a Sn-57Bi-1Ag homogeneous joint after reflow

Therefore, the understanding for microstructure evolution in Sn-Bi binary systems is necessary to better achieve low temperature soldering. Based on traditional thermodynamic model and normal diffusion model, the microstructure evolution inside the system during reflow process could be predicted. Before reflow, the system contains Sn-Bi eutectic solder paste, and SAC solder, which contains no Bi in it. During heating, eutectic Sn-Bi solder will melt first and wet Sn particles. During isothermal hold, the overall composition of the system falls into the binary phase region

(liquid and Sn solid solution) on Sn-Bi phase diagram, as illustrated in Figure 1.4(a), after the initial melting of Sn-Bi eutectic particles, Sn starts to dissolve into the liquid, as a result, total fraction of liquid will increase at this moment, and the composition of the liquid phase begins to shift towards liquidus line, as illustrated in progress ① in Figure 1.4(a). When the liquid composition reaches the liquidus composition, Bi starts to diffuse into pure Sn to form Sn-Bi solid solution. The excess Sn in the liquid phase will precipitate on the surface of Sn as Sn-Bi solid solution in order to keep the liquid composition fixed on the liquidus line, as shown in step ② in Figure 1.4(a). During this stage, the amount of the liquid phase will decrease until the system reaches equilibrium, the amount of liquid and solid phases will follow the lever rule on the phase diagram. Therefore, in this situation, the liquid will never fully solidify during isothermal hold. During cooling, in the liquid phase, Sn-Bi solid solution will solidify first, when the temperature reaches eutectic temperature, Bi and Sn-Bi solid solution will solidify together to form a lamellar eutectic structure. The solid phase, on the other hand, will reach the solvus line during cooling, and the excess Bi in Sn-Bi solid solution will continue to precipitate out through further cooling due to solubility change, as shown in step ③ in Figure 1.4(a). A schematic illustration of this diffusion model is shown in Figure 1.4(b). Normally during practical situations, equilibrium status is hard to achieve due to short isothermal hold time, which is known as Scheil effect. As a result, Bi in the liquid phase does not have enough time to diffuse all way into Sn. Therefore, after cooling, a concentration gradient could usually be seen in Sn-Bi solid solution, as illustrated in Figure 1.4(c).

From the normal diffusion model, the microstructure evolution during reflow process should have the following characteristics: (1) during annealing, the remaining volume fraction of liquid phase in the system will slowly decrease till equilibria; (2) the Bi composition in Sn will slowly increase during annealing until the Bi composition reaches the solubility limit (solidus line); (3) the Bi composition in Sn-Bi solid solution should never exceed the solubility limit.

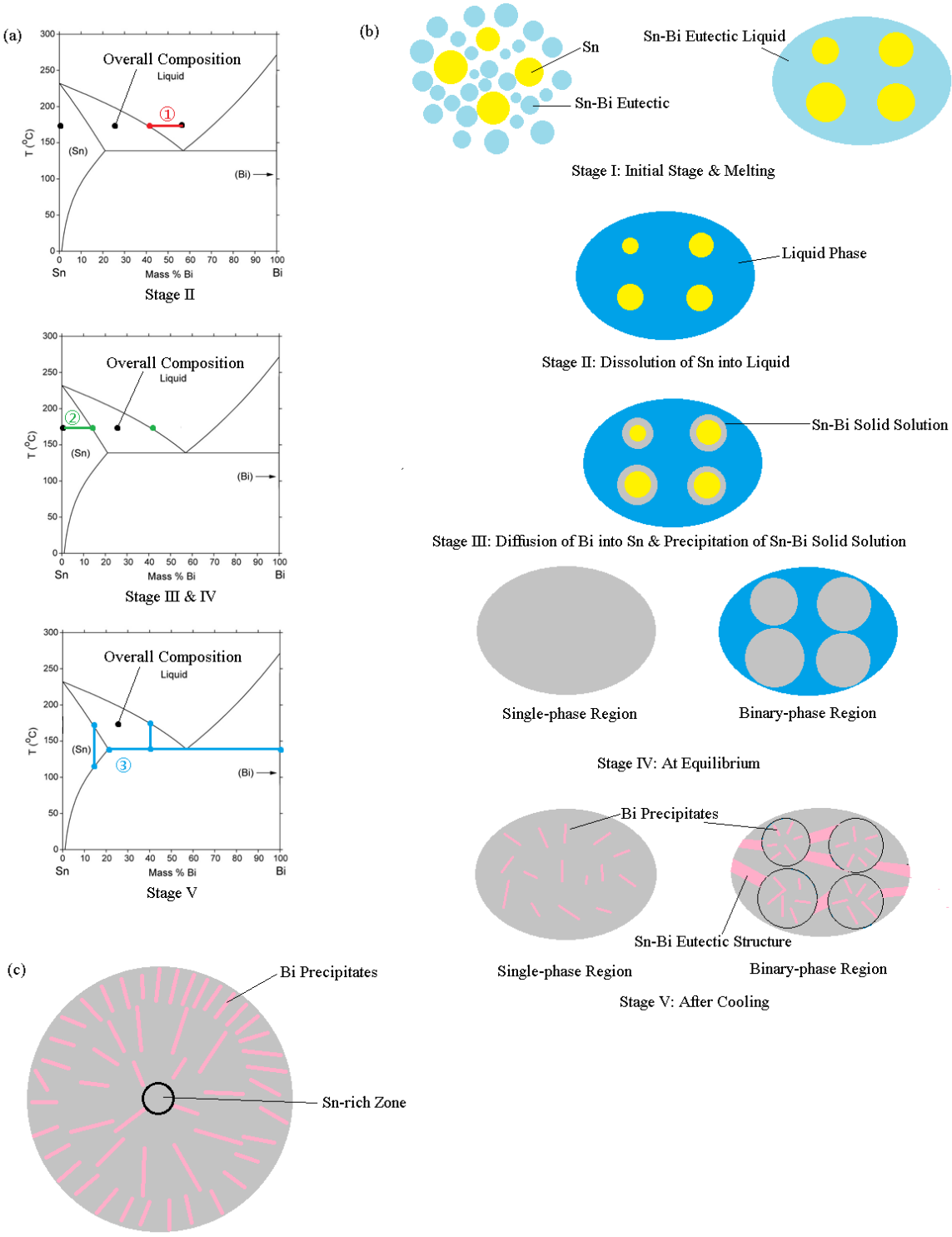

Figure 1.4. (a) A schematic illustration of TLPS process where overall Bi composition falls into binary phase region during isothermal hold; (b) a conceptual model of TLPS in Sn-Bi solder paste at high-Bi content area; (c) close look of radial concentration gradient of Bi precipitates in non-equilibrium situation

Differential scanning calorimetry (DSC) has been considered as a new method to accurately quantify the kinetics the kinetics of interface motion in solid/liquid diffusion couple [13]. DSC has its own advantage in monitoring real-time change in different transient liquid phase sintering (TLPS) systems [14], as well as quantitatively characterize the kinetics of isothermal solidification and the remaining liquid fraction in the system [15]. Previous research results have contributed a lot in the comprehensive understanding of Sn-Bi binary TLPS systems [14, 16-19]. However, some area in Sn-Bi TLPS system is still missing: (1) previous study mainly focused on the study of ternary Sn-Bi-X (X represents other metal, such as Pb, Cu and Ni) systems, more work still needs to be finished on binary Sn-Bi TLPS system; (2) previous study mainly focused on systems with low-Bi compositions (wt.% Bi≤10%). The melting and solidification characteristics of higher-Bi content TLPS systems are still mysterious and need to be studied urgently; (3) although a comprehensive understanding of the melting characteristics of Sn-Bi TLPS systems has been established, there is no previous study focused on the cooling process. The solidification and phase transformation during cooling need to be discovered.

In this study, microstructure development and Bi diffusion characteristics in Sn-Bi systems with different Bi compositions will be carefully studied. DSC is utilized in demonstrating the melting, re-solidification and cooling characteristics of Sn-Bi binary systems with different Bi compositions. Different heating files are used to determine the microstructure development in solder pastes. Scanning electron microscope (SEM), energy dispersive X-ray spectroscopy (EDS) and electron backscattered diffraction (EBSD) are used to help observe the microstructure evolution, Bi diffusion characteristics and Sn grain growth rates after reaction and compare with thermodynamic model and normal diffusion model predictions. A model of Bi diffusion into Sn during heating and annealing will also be established.

1.3 Experimental

Two commercial solder pastes of different compositions were used to form the Sn-Bi solder paste mixtures: eutectic Sn-57.6wt.%Bi-0.4wt.%Ag (KOKI Co Ltd.), and Sn-0.7wt.%Cu (Nihon Superior®) with an average particle diameter of 25μm. The solder pastes were carefully weighed and stirred by hand followed by a centrifugal mixing to achieve an even distribution of solder particles.The experiments described here were performed with paste mixtures with an overall Bi composition of 30 wt.%. Differential scanning calorimetry (TA® Q-100 DSC) was used to

measure the heat flow curves as a function of temperature, time, and ramp rate. of different samples. After DSC, all the samples were carefully mounted in epoxy and polished with diamond suspension (Allied High Tech). Quanta 650 FEG SEM was used to observe the microstructure evolution and Bi diffusion characteristics in all the samples. EDS and EBSD were utilized to study the Bi composition in different parts of the samples, and the Sn grain growth during isothermal hold process.

1.4 Results and Discussion

1.4.1 Thermodynamic model simulation of Sn-Bi system

For Sn-Bi binary systems, the theoretical phase transformation and equilibrium volume fraction of liquid during isothermal hold could be calculated using thermodynamics. The volume fraction of liquid in Sn-Bi mixture system at different isothermal hold temperatures could be calculated by binary phase diagram, as shown in Figure 1.5 below. For this study, most of the samples were held at 145°C and 165°C, which have the equilibrium liquid volume fraction of 28% and 48%, respectively.

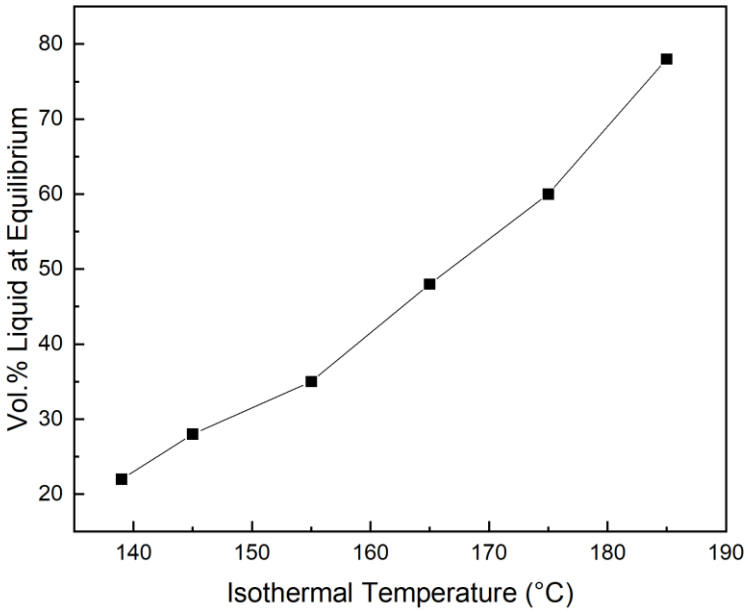

Figure 1.5. Volume fraction of liquid in Sn-30Bi mixture during equilibrium at different annealing temperatures

Stable phases during equilibrium at different temperatures in Sn-30Bi mixtures could be simulated by Thermo-Calc, which are shown in Figure 1.6 below. Since the original pastes contain Cu and Ag, Cu_6Sn_5 and Ag_3Sn intermetallic compounds could be picked up inside the system. However, the influence of intermetallic compounds on the system could be ignored due to the low amount of Cu and Ag inside the solder pastes. At 145°C and 165°C, the stable phases inside the system are liquid, (Sn) (Sn-Bi solid-solution) and Cu_6Sn_5.

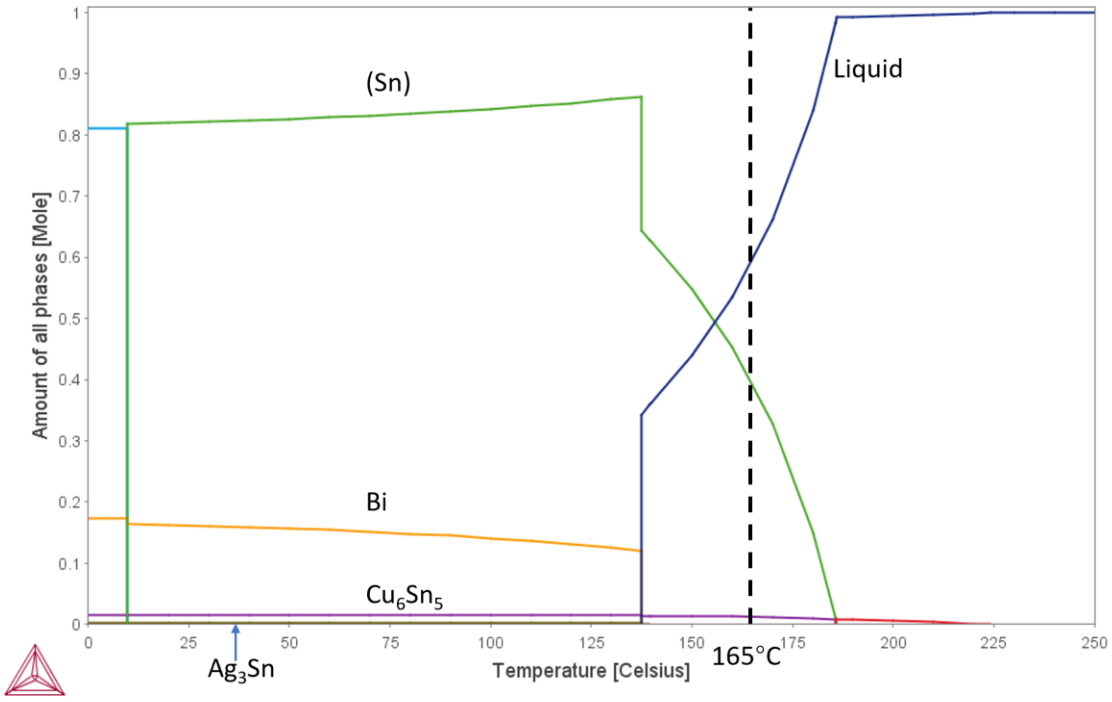

Figure 1.6. Stable phases in Sn-30Bi mixtures at different annealing temperatures

1.4.2 Microstructure evolution during two-phase annealing

Different heating profiles were used to characterize the microstructure development in solder pastes: (1) in order to determine the Bi diffusion rate into Sn when the initial liquid phase forms, the samples were heated to a peak temperature of 145℃ with a heating rate of 20℃/min, and then cooled down to room temperature with a cooling rate of 10℃/min and air quench without isothermal hold; (2) the samples were heated to a peak temperature of 165℃ with a heating rate of 20℃/min, and held at the peak temperature for 0, 5, 60 and 240 minutes respectively, and then cooled down to room temperature with a cooling rate of 10°C/min.

To qualitatively determine Bi diffusivity into Sn when the initial liquid phase forms, two different heating rates were utilized on Sn-30 wt.% samples: the samples were heated to a peak temperature of 145℃ with a heating rate of 20℃/min, and then cooled down to room temperature with a cooling rate of (1) 10℃/min, and (2) air quench without isothermal hold. The backscattered images for the samples after two heating profiles could be seen in Figure 1.7. The original structures of Sn and Sn-Bi eutectic solder particles could still be seen in the air-quenched samples, due to the short time-above-liquidus (TAL=18s). However, the Bi diffusion into Sn could already be seen in the quenched sample, since some fine Bi precipitates have already appeared at the surface of Sn particles. If a normal cooling rate is utilized (10℃/min, TAL=54s), after cooling, all the original Sn particles were filled with fine Bi precipitates, and barely any Sn-Bi eutectic structures could be seen in the system.

A qualitative calculation could be performed to estimate the effective diffusion coefficient of Bi into Sn when the liquid phase forms. According to the diffusion distance equation:

$$x = \sqrt{6Dt},$$

Taking the average radius of the solder paste particles (12.5μm), and the total time above liquidus (TAL=54s), the effective coefficient for Bi to diffuse 12.5μm in Sn in 54 seconds is:

$$D = \frac{x^2}{6t} = \frac{(12.5\times10^{-4}\ cm)^2}{6\times54\ s} = 4.82 \times 10^{-9}\ cm^2/s.$$

However, after 54 seconds of TAL, Bi has fully diffused through Sn particles. Therefore, the actual effective Bi diffusion coefficient should be even larger than $4.82 \times 10^{-9}\ cm^2/s$, since it took no more than 54 seconds for Bi to diffuse through Sn.

According to the previous results of Delhaise and Perovic [20], the diffusion coefficient of Bi in Sn at 145°C should be $4.12\times 10^{-10}\ cm^2$, which is much lower than the calculated value. The reason for the difference is Delhaise's research mainly focused on solid-state diffusion of Bi in Sn. When the liquid phase forms, the Bi diffusion in Sn will be much faster.

The results showed that Bi has a really high diffusion rate into Sn when the initial liquid phase forms.

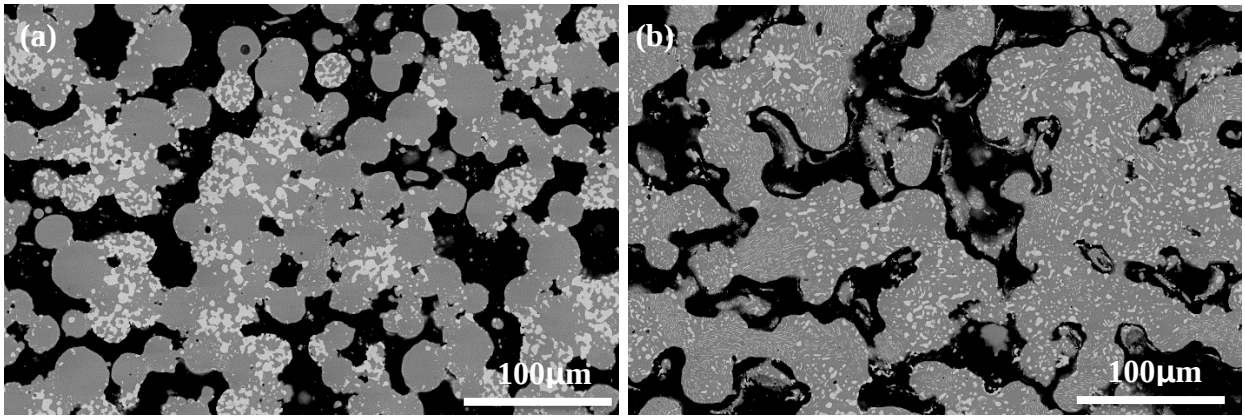

Figure 1.7. Backscattered SEM pictures for Sn-30 wt.%Bi samples heated to 145°C and then cooled down to room temperature at different rates with (a) air quench, and (b) 10°C/min cooling rate

The backscattered images for Sn-30 wt.% Bi samples annealed at 165°C for different amount of time are shown in Figure 1.8 below. From the microstructure, during annealing, more and more Sn-Bi lamellar eutectic structure could be seen after cooling, and the size of Sn dendrites surrounded by the eutectic structure also increased fast during annealing. The Bi precipitates inside Sn-Bi solid solution have two different morphologies: the needle-shaped, oriented fine Bi precipitates, and the larger, spheroidal Bi precipitated surrounding the fine needle-shaped Bi precipitates.

In order to determine why the morphology difference of Bi precipitates exist in the system, and the grain growth rate of Sn-Bi solid solution during annealing, EBSD mapping was utilized in these samples. The scanning mainly focused on the Sn-Bi solid solution region, and all the results are shown in Figure 1.9. From the EBSD results, in original Sn particles, Sn had a fine, polycrystalline grain structure with an average grain size around 10 μ m. During annealing, Sn grain size grew dramatically. In Sn-30 wt.% Bi sample heated to 165°C and directly cooled down with no annealing (TAL=4 min), very large Sn grains have already formed in the system, but still with a large amount of finer Sn grains. The finer Sn grains grow into huge grains after 4 hours of annealing with an average grain size increasing to 35μm. For Bi precipitates, the needle-shaped, oriented fine Bi precipitates appear inside the Sn grains, while the larger, spheroidal Bi precipitates could usually be seen at the grain boundaries, or the regions where the fine, polycrystalline Sn exists.

In order to understand the microstructure evolution and how the Bi diffuses into Sn during the reaction process, an establishment of Bi diffusion model into Sn will be discussed in the following section.

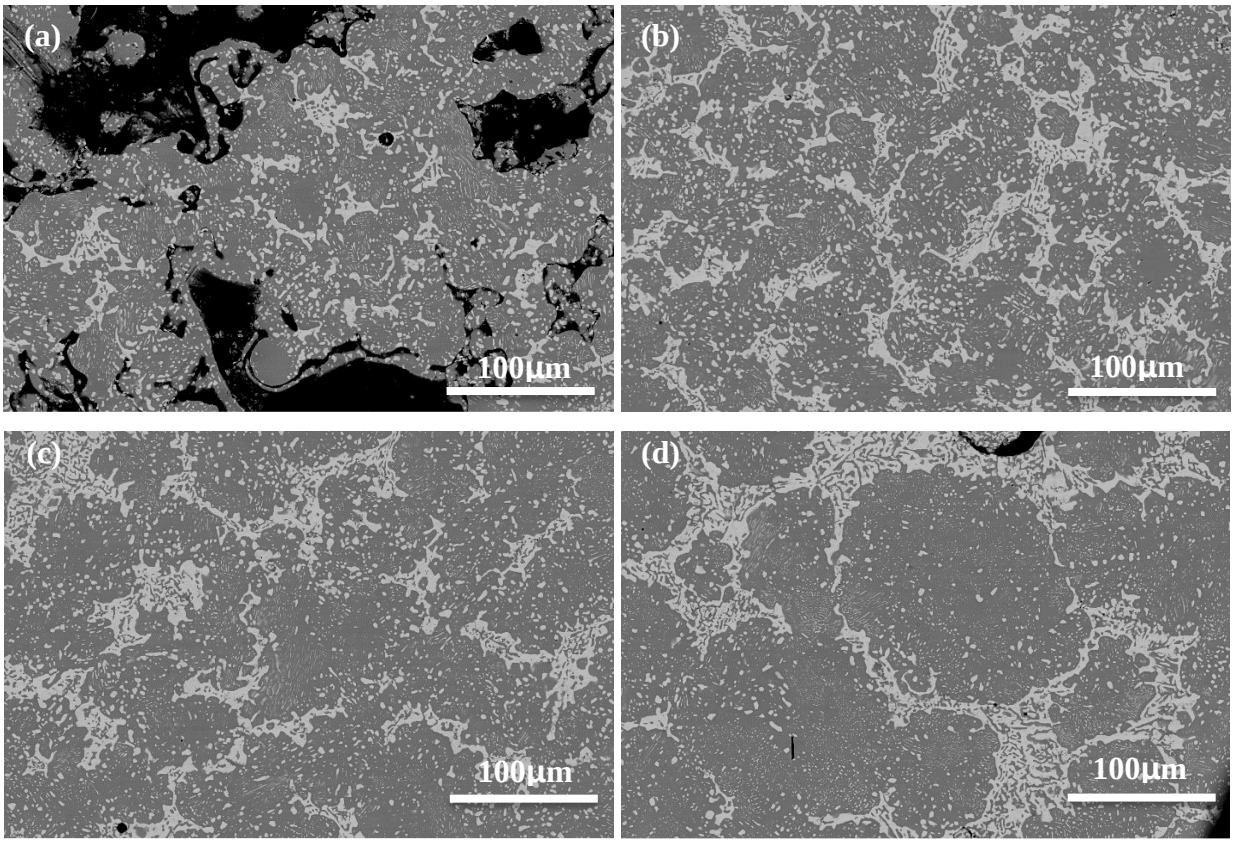

Figure 1.8. Microstructure of Sn-30 wt.% Bi samples annealed at 165°C for (a) 0 min; (b) 5 min; (c) 60 min; and (d) 240 min

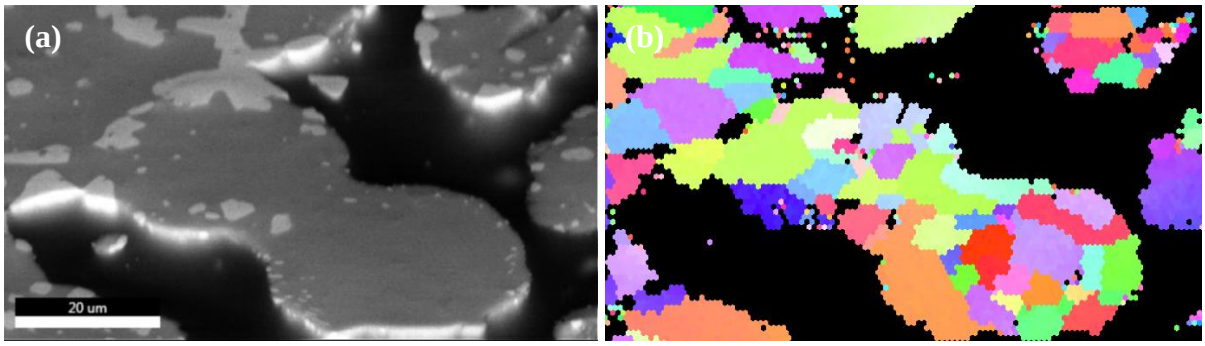

Figure 1.9. Microstructure and Sn orientation structures of Sn-30 wt.% Bi samples heated to 145°C with (a, b) air quench with no isothermal hold; and (c, d) cooled down with 10°C/min with no isothermal hold; and Sn-30 wt.% Bi samples heated to 165°C and then cooled down with 10°C/min with the isothermal hold time of (e, f) 0 min; (g, h) 5 min; (i, j) 60min; and (k, l) 240 min

Figure 1.9 continued

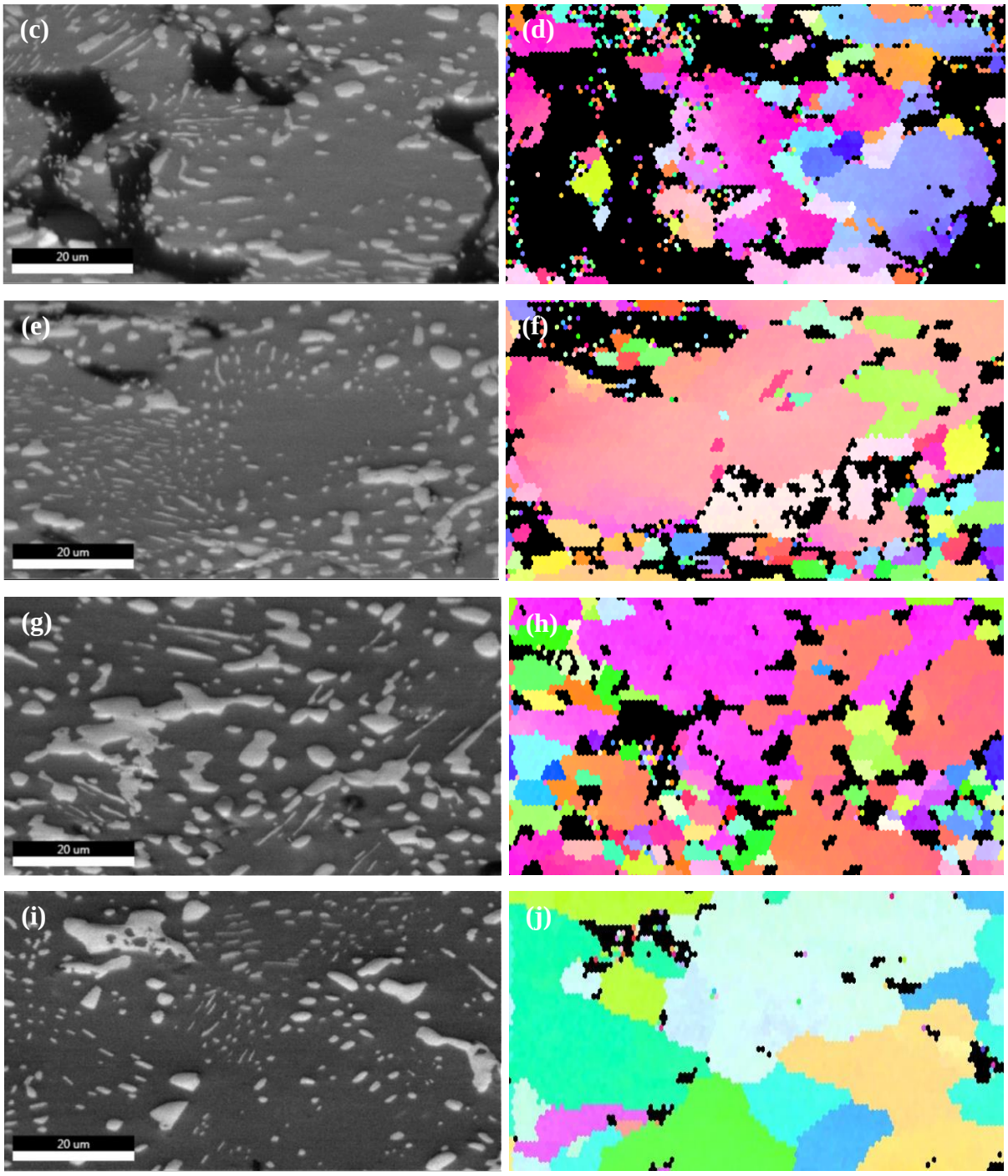

Figure 1.9 continued

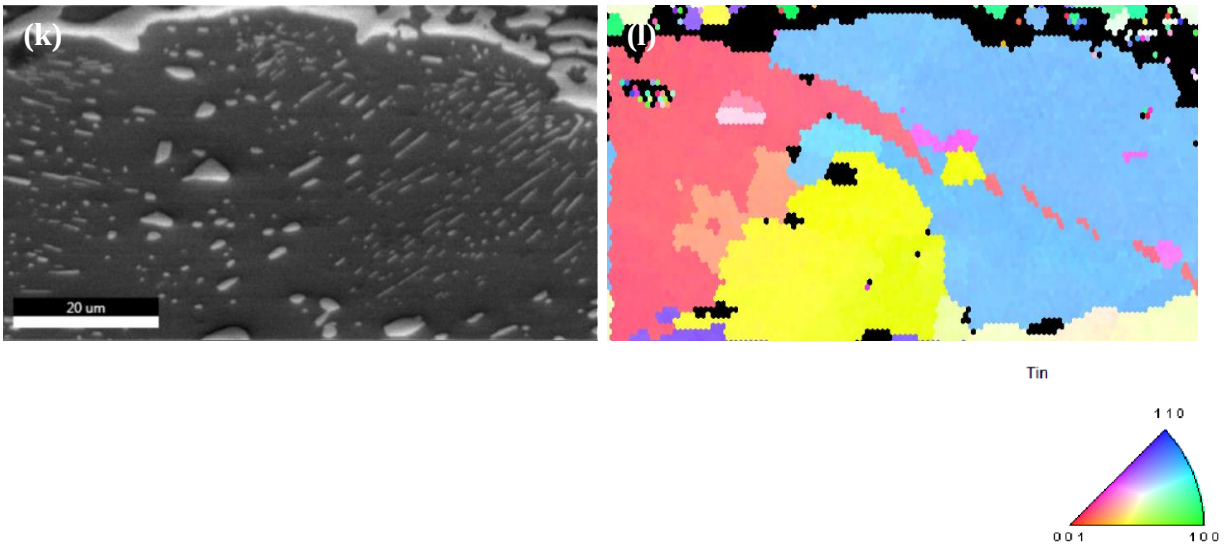

To determine Bi diffusion characteristics in Sn during annealing, EDS mapping was used in Sn-30 wt.% Bi samples. The mapping mainly focused on the (1) Bi composition inside Sn-Bi solid solution, where the needle-shaped, oriented fine Bi precipitates exist, and (2) Sn grain boundary regions, where the larger, spheroidal Bi precipitates reside. The analysis results are listed in Table 1.1 below. The actual results, however, do not agree with the predicted results from normal diffusion model at all. The Bi composition in Sn-Bi solid solution not only exceeded the solubility limit, but the Bi composition decreased during isothermal hold process, which is completely the opposite with the predicted results from normal diffusion model. Therefore, Bi does not follow the normal diffusion model, another diffusion model should be applied.

Table 1.1. EDS results of Bi composition in different areas of Sn-Bi solder system after annealing

Heating Profile	Overall Bi Composition	Wt.% Bi Inside Sn Grains	Wt.% Bi at Grain Boundaries	Remaining Liquid Vol.% During Cooling
At Equilibrium	30	15	15	48
145°C no isothermal hold	30	27	30	--
165°C no isothermal hold	31	25	31	14
165°C 5 min	30	23	28	16
165°C 60 min	31	20	25	22
165°C 240 min	29	19	22	26

1.4.3 Phase transformation during two-phase annealing

DSC traces of Sn-30Bi solder paste mixture samples are shown in Figure 1.10 below. The DSC traces revealed the phase transformation in different Sn-Bi systems. During heating, the DSC trace curved downwards due to the solution of Bi into Sn, and the evaporation of the flux in the system, which are endothermic. When the temperature reached the eutectic temperature of Sn-Bi system, a sharp eutectic melting peak, which corresponds with the melting of eutectic Sn-Bi solder paste could be observed. After the initial liquid phase formed, another wide endothermic bump could be seen on the DSC curve, which corresponds with the additional melting of Sn in the system. During cooling, Sn-Bi solid solution began to precipitate out from the liquid phase, which appeared on the DSC curve as wide exothermal bump at the beginning of the cooling process. during further cooling, since the overall composition of Bi comes across the invariant line on the phase diagram, when the temperature reached the eutectic temperature, a sharp eutectic solidification peak could be observed with an undercooling of about 10°C. The reason for the area of the peaks during heating and cooling do not add up to 0 is because during isothermal hold process, there are Bi diffusion as well as Sn solidification, as well as liquid forming, which all result in heat change in the system, which are all invisible on the heat flow – temperature diagrams, but could be observed as base line change on heat flow – time diagrams.

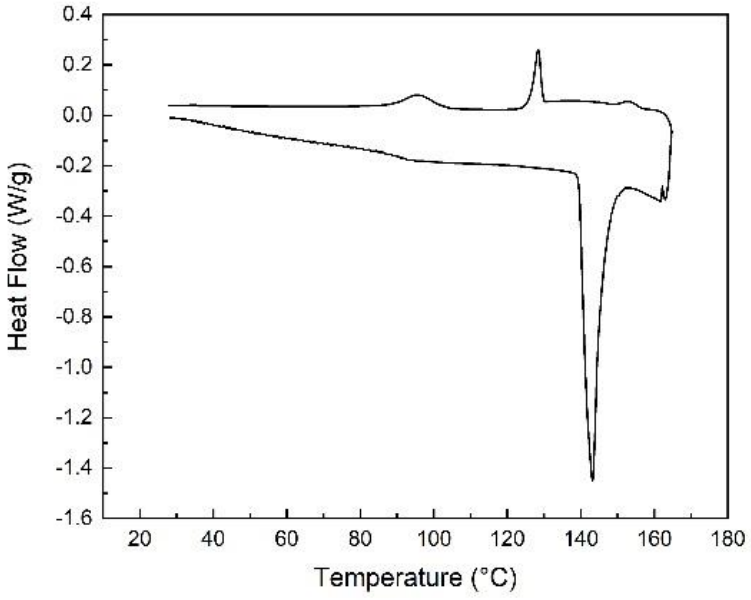

Figure 1.10. DSC traces of Sn-30 wt.% Bi Sn-Bi mixture held at 165°C for 5 minutes

In Sn-30%Bi mixtures, after the eutectic solidification, another exothermal peak was seen in all of these samples. The positions of the peaks dropped to a lower temperature when the isothermal hold temperature increased, and formed a nice linear relationship with the isothermal hold temperature, as shown in Figure 1.11(b) below. The reason for this low-temperature bump to appear is the precipitation of excess Bi in Sn-Bi solid solution during cooling, when the Bi composition of Sn-Bi solid solution reached the solvus line. According to the Sn-Bi phase diagram, at higher isothermal hold temperature, the Bi has a lower solubility in Sn. Therefore, during cooling, the sample held at a higher temperature will hit the solvus line later, which will cause the bump to shift towards a lower temperature, just as shown in Fig 1.11(a), another plot of low-temperature bump positions versus the corresponding solvus temperature at different isothermal hold temperatures is shown in Fig 1.11(c). The low-temperature peak positions also follows a nice linear relationship with the corresponding solvus temperature. Since the solvus line on Sn-Bi phase diagram is nearly linear on our testing range, the hypothesis of the microstructure change in this low-temperature peak is confirmed.

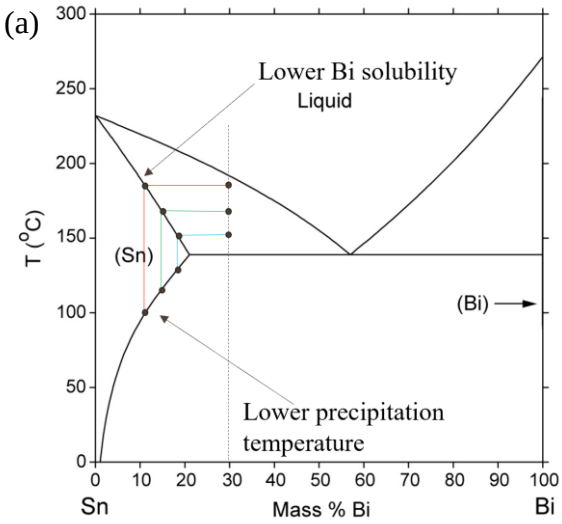

Figure 1.11. (a) Schematic illustration on Sn-Bi phase diagram showing higher isothermal hold temperature results in lower Bi solubility in Sn and lower precipitation temperature during cooling; (b) the linear relationship between Bi precipitation temperature and isothermal hold temperature; (c) the linear relationship between Bi precipitation temperature and corresponding solvus temperature

Figure 1.11 continued

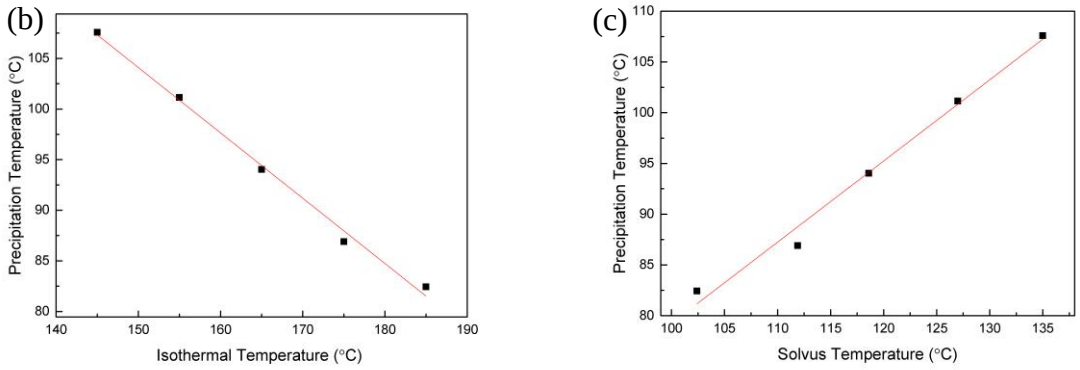

The remaining volume fraction of liquid inside the system after two-phase annealing could be quantitatively calculated by integrating the area under the eutectic solidification peak on the DSC curves. The remaining volume fraction of liquid in Sn-30 wt.% Bi samples after different annealing time could be seen in Figure 1.12 below. The DSC results revealed the increasing amount of liquid forming in the system during two-phase annealing, which is also completely the opposite from thermodynamic model predictions. Also, the volume fraction of liquid remaining in the system even after 4 hours of aging was still much lower than the equilibrium volume fraction of remaining liquid phase according to phase diagram (26vol% vs 48vol%).

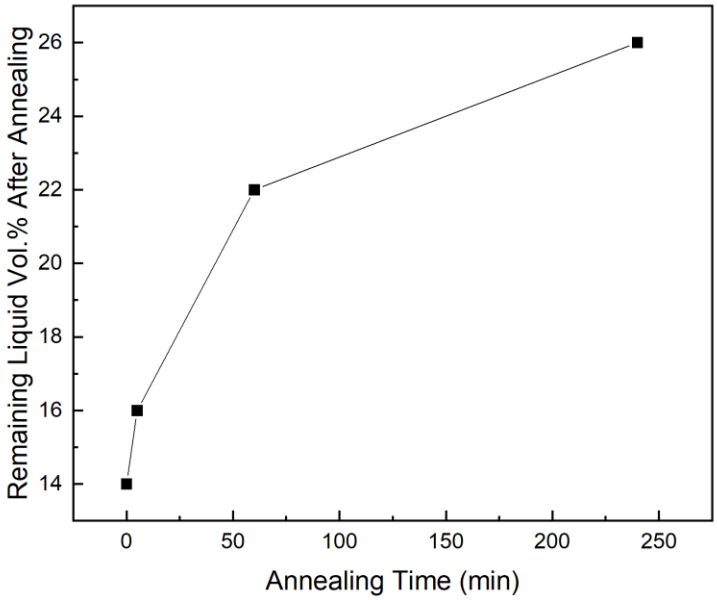

Figure 1.12. The remaining volume fraction of liquid in Sn-30 wt.% Bi samples after different annealing time at 165°C, showing increasing amount of liquid during annealing process

Therefore, according to thermal and metallographic analysis, the microstructure evolution in Sn-Bi binary system could not fit traditional thermodynamic and normal diffusion models. A new model for Bi diffusion and distribution in Sn must be constructed.

1.4.4 Bi segregation model establishment

Delhaise and Perovic have found the preliminary Bi diffusion characteristics in Sn during solid-state annealing [17]. Their results revealed that the diffusion of Bi in Sn is much faster than the self-diffusion of Sn, which means the diffusion of Sn in Bi is negligible compared with diffusion of Bi in Sn. The multi-grain structure in Sn could produce even faster grain boundary diffusion, and the grain boundary diffusion is the dominate diffusion mechanism in the overall diffusion process.

The observed results in Sn-30 wt.% Bi samples agreed with Delhaise and Perovic's conclusions. The microstructure and EDS showed dominantly high Bi diffusion rate in Sn during reaction process, and the Bi composition at Sn grain boundary regions is higher than the Bi composition inside the Sn grains. Therefore, a new Bi segregation model could be constructed based on the experimental observations. At the beginning of the annealing process, the average Sn grain size in the solid phase is small, as shown in Figure 1.9, which means a large amount of grain boundary areas inside Sn solid solution. Since Bi has a larger amount of segregation at Sn grain boundaries according to the observations in Table 1.1, the average composition of Bi in Sn solid solution will be higher, as shown as the red dot on the Sn-Bi phase diagram in Figure 1.13 below. With higher Bi composition in Sn solid solution and fixed liquidus composition, the amount of liquid in the two-phase system will be less than equilibrium amount according to lever rule, which corresponds with the lower-than-expected remaining liquid volume fraction at the beginning of the annealing process. As the annealing process goes on, Sn grain growth is seen in the system, shown in Figure 1.9, which results in less grain boundary area in Sn solid solution as well as less Bi segregation regions. Therefore, the average Bi composition inside Sn will slowly decrease as Sn grains grow, which shifts back towards the solidus composition at equilibrium. According to the lever rule, once the Bi composition in Sn moves back to solidus composition during further annealing, the amount of liquid increases in the system, which also corresponds with the DSC results.

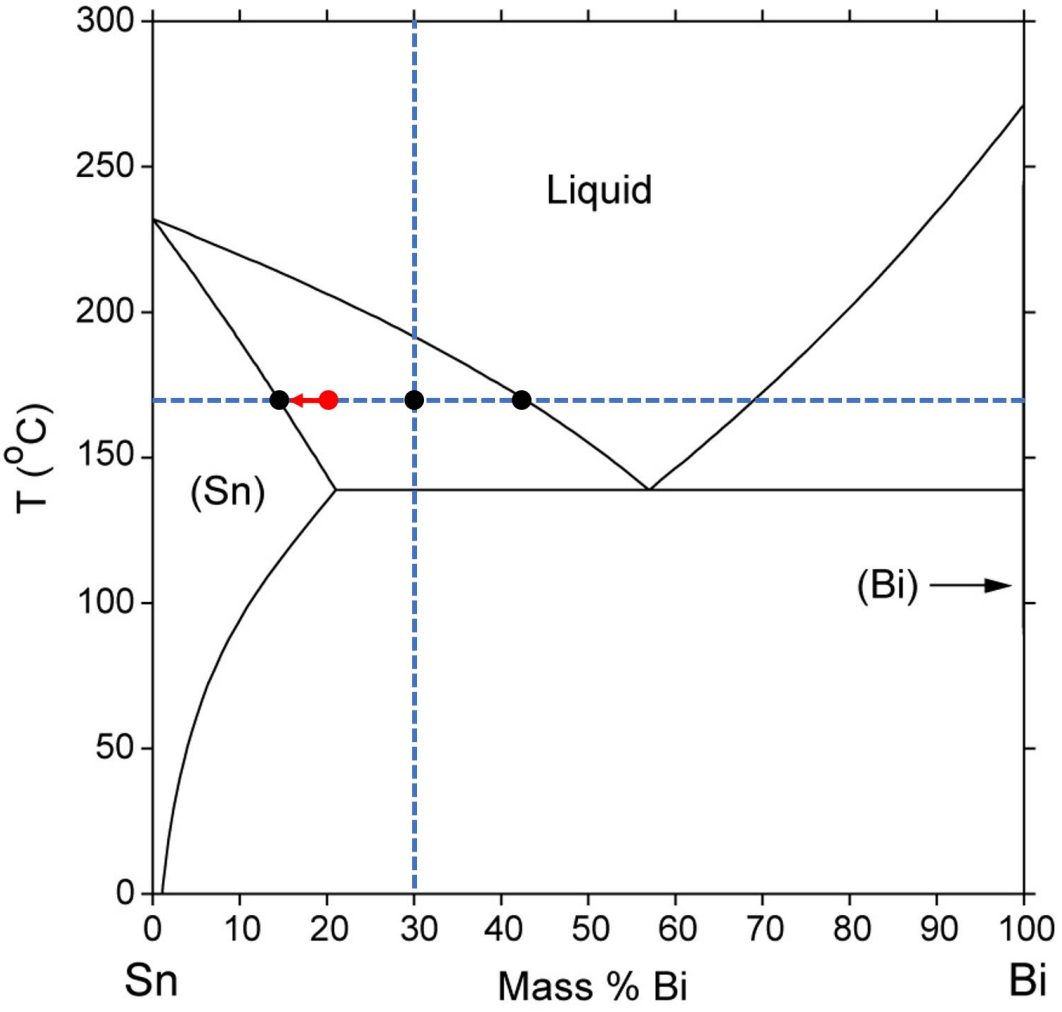

Figure 1.13. Bi composition change in Sn solid solution during annealing process due to Bi segregation at Sn grain boundaries

1.5 Conclusions

- During initial melting and annealing in Sn-Bi solder system, Bi diffuses into Sn at a very high rate through grain boundary diffusion.
- After annealing, three different Bi morphologies exist in the system: the lamellar Sn-Bi eutectic structure, non-eutectic, spheroidal bulk Bi precipitates which exist at grain boundary regions, and fine, oriented needle-shaped Bi precipitates residing inside Sn grains.
- During annealing process, Bi has a much higher solubility in Sn due to segregation at Sn grain boundaries, higher Bi composition in Sn results in less liquid amount according to lever rule

at the beginning of the annealing. With further annealing process, the decreasing grain boundary areas in the system caused the system slowly shift to equilibrium state, as a result, the Bi composition in Sn-Bi solid solution slowly drops and the volume fraction of liquid in the system increases till equilibrium.

1.6 Acknowledgment

The author wants to acknowledge Intel Cooperation for the grant on supporting this research.

1.7 References

[1] Bath, J., Garcia, R., Uchida, N., Takahashi, H., Clark, G., & Itoh, M. (2009). Investigation and development of tin-lead and lead-free solder pastes to reduce the head-in-pillow component soldering defect. SMTA International Proceedings 2009.

[2] Boettinger, W. J., Handwerker, C. A., Newbury, B., Pan, T. Y., & Nicholson, J. M. (2002). Mechanism of fillet lifting in Sn-Bi alloys. Journal of electronic materials, 31(5), 545-550.

[3] Henshall, Gregory, Jasbir Bath, and Carol A. Handwerker, eds. Lead-free solder process development. John Wiley & Sons, 2011.

[4] Hua, F., Mei, Z., & Glazer, J. (1998, May). Eutectic Sn-Bi as an alternative to Pb-free solders. In 1998 Proceedings. 48th Electronic Components and Technology Conference (Cat. No. 98CH36206) (pp. 277-283). IEEE.

[5] Ferrer, E., & Holder, H. (2003, March). 57Bi-42Sn-1Ag: A Lead Free, Low Temperature Solder for the Electronic Industry. In JEDEX Conference, San Jose, CA, March (pp. 22-25).

[6] Aspandiar, R., Byrd, K., Tang, K. K., Campbell, L., & Mokler, S. (2015, February). Investigation of low temperature solders to reduce reflow temperature, improve SMT yields and realize energy savings. In Proceedings of the 2015 APEX Conference.

[7] Chen, O. H., Byrd, K., Mokler, S., Tang, K. K., & Aspandiar, R. (2015, May). Comparison of the Mechanical Shock/Drop Reliability of Flip Chip BGA (FCBGA) Solder Joints Formed by Soldering with Low Temperature BiSn-Based Resin Reinforced Solder Pastes. In Proceedings of the International Conference on Soldering and Reliability.

[8] Chen, O. H., Molina, A., Aspandiar, R., Byrd, K., Mokler, S., & Tang, K. K. (2015, September). Mechanical shock and drop reliability evaluation of the BGA solder joint stack-ups formed by reflow soldering SAC solder balls BGAs with BiSnAg and resin reinforced BiSn-based solder pastes. In Proceedings of SMTA International (pp. 215-222).

[9] Mokler, S., Aspandiar, R., Byrd, K., Chen, O., Walwadkar, S., Tang, K. K., ... & Sane, S. (2016, September). The application of Bi-based solders for low temperature reflow to reduce cost while improving SMT yields in client computing systems. In Proceedings of SMTA International (pp. 318-326).

[10] Silva, B. L., Xavier, M. G., Garcia, A., & Spinelli, J. E. (2017). Cu and Ag additions affecting the solidification microstructure and tensile properties of Sn-Bi lead-free solder alloys. Materials Science and Engineering: A, 705, 325-334.

[11] Sahasrabudhe, S., Mokler, S., Renavikar, M., Sane, S., Byrd, K., Brigham, E., ... & Parupalli, S. (2018, May). Low Temperature Solder-A Breakthrough Technology for Surface Mounted Devices. In 2018 IEEE 68th Electronic Components and Technology Conference (ECTC) (pp. 1455-1464). IEEE.

[12] Lee, Byeong-Joo, Chang-Seok Oh, and Jae-Hyeok Shim. "Thermodynamic assessments of the Sn-In and Sn-Bi binary systems." Journal of electronic materials 25.6 (1996): 983-991.

[13] Kuntz, M. L., S. F. Corbin, and Y. Zhou. "Quantifying metallurgical interactions in solid/liquid diffusion couples using differential scanning calorimetry." Acta materialia 53.10 (2005): 3071-3082.

[14] Qiao, X., and S. F. Corbin. "Development of transient liquid phase sintered (TLPS) Sn–Bi solider pastes." Materials Science and Engineering: A 283.1-2 (2000): 38-45.

[15] Kuntz, M. L., Y. Zhou, and S. F. Corbin. "A study of transient liquid-phase bonding of Ag-Cu using differential scanning calorimetry." Metallurgical and Materials Transactions A 37.8 (2006): 2493.

[16] Corbin, S. F., and D. J. McIsaac. "Differential scanning calorimetry of the stages of transient liquid phase sintering." Materials Science and Engineering: A 346.1-2 (2003): 132-140.

[17] Reyburn, Beth, and Stephen Corbin. "Monitoring transient liquid phase sintering of Cu-Sn alloys by thermal analysis." International journal of powder metallurgy 36.5 (2000): 57-68.

[18] Whitney, M., and S. F. Corbin. "Lead contamination of a transient liquid-phase-processed Sn-Bi lead-free solder paste." Journal of electronic materials 35.2 (2006): 284-291.

[19] Yoon, Seung Wook, and Hyuck Mo Lee. "A thermodynamic study of phase equilibria in the Sn-Bi-Pb solder system." Calphad 22.2 (1998): 167-178.

[20] Delhaise, André M., and Doug D. Perovic. "Study of Solid-State Diffusion of Bi in Polycrystalline Sn Using Electron Probe Microanalysis." Journal of Electronic Materials 47.3 (2018): 2057-2065.

1.8 Appendix

Phase transformation during two-phase annealing

DSC traces of 10%, 20%, 30% and 40% Sn-Bi solder paste mixture samples are shown in Figure 1.14 below. The DSC traces revealed the phase transformation in different Sn-Bi systems. During heating, the DSC trace curved downwards due to the solution of Bi into Sn, and the evaporation of the flux in the system, which are endothermic. When the temperature reached the eutectic temperature of Sn-Bi system, a sharp eutectic melting peak, which corresponds with the melting of eutectic Sn-Bi solder paste could be observed. After the initial liquid phase formed, another wide endothermic bump could be seen on the DSC curve, which corresponds with the additional melting of Sn in the system. During cooling, Sn-Bi solid solution began to precipitate out from the liquid phase, which appeared on the DSC curve as wide exothermal bump at the beginning of the cooling process. For high-Bi content solder paste mixtures, since the overall composition of Bi comes across the invariant line on the phase diagram, when the temperature reached the eutectic temperature, a sharp eutectic solidification peak could be observed with an undercooling of about 10°C. After all the liquid in the system has totally solidified, no other signals could be detected by DSC.

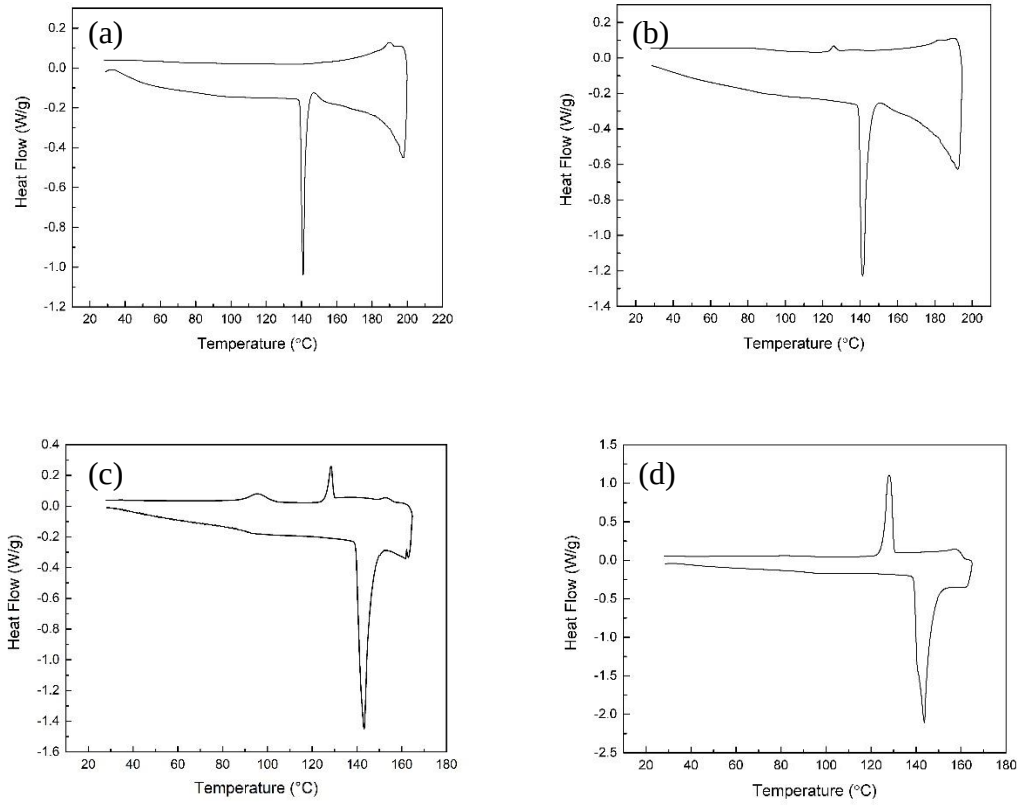

Figure 1.14. DSC traces of (a) Sn-10 wt.% Sn-Bi mixture; (b) Sn-20 wt.% Sn-Bi mixture; (c) Sn-30 wt.% Bi Sn-Bi mixture; and (d) Sn-40 wt.% Bi Sn-Bi mixture held at peak temperature for 5 minutes

2. INFLUENCE OF PAD SURFACE FINISH ON THE MICROSTRUCTURE EVOLUTION AND INTERMETALLIC COMPOUND GROWTH IN HOMOGENEOUS TIN-BISMUTH AND TIN-BISMUTH-SILVER SOLDER INTERCONNECTS

2.1 Abstract

Low reflow temperature solder interconnect technology based on Sn-Bi alloys is currently being considered as an alternative for Sn-Ag-Cu solder alloys to form solder interconnects at significantly lower melting temperatures than required for Sn-Ag-Cu alloys. Microstructural evolution after reflow and aging, especially of intermetallic compound (IMC) growth at solder/pad surface finish interfaces, is important to understanding fatigue life and crack paths in the solder joints. This study describes intermetallic growth in homogeneous solder joints of Sn-Bi eutectic alloy and Sn-Bi-Ag alloys formed with electroless nickel-immersion gold (ENIG) and Cu-organic surface protection (Cu-OSP) surface finishes. Experimental observations revealed that, during solid state annealing following reflow, the 50nm Au from the ENIG surface finish catalyzed rapid (Ni,Au)Sn4 intermetallic growth at the Ni-solder interface in both Sn-Bi and Sn-Bi-Ag homogeneous joints, which led to significant solder joint embrittlement during fatigue testing. Intermetallic growth of (Ni,Au)Sn4 was decreased by Ag alloying of eutectic Sn-Bi solder and was completely eliminated by changing the metallization from ENIG to Cu-OSP on the board side of the assembly. The reduction in (Ni,Au)Sn4 growth rate with Ag additions is attributed to changes in grain boundary wetting of the IMC by Bi with Ag alloying.

Keywords: Tin-bismuth solder, electroless nickel immersion gold, gold embrittlement, intermetallic growth

2.2 Introduction

Three-dimensional (3D) packaging technologies, specifically, large area Heterogeneously Integrated System-in Package (SIP) technologies, are critical for achieving modern high performance, high bandwidth systems [1]. As these SIPs grow in area, warpage of the substrates leading to either solder joint bridging (short circuit) or gaps (open circuit) becomes a significant reliability concern [2]. Since the extent of warpage is directly proportional to solder reflow temperature, there is a need to reduce the peak reflow temperature by using alternative “low

temperature" solder alloys. Tin-silver-copper (SAC) alloys, the industry standard, require peak reflow temperatures of approximately 240°C due to their high eutectic temperature (217°C). Such high reflow temperatures have been observed to cause serious warpage-induced defects, such as separation of SAC solder balls from SAC solder paste before melting (217°C) to form head-on-pillow (HoP) defects along the edges of the IC and bridging in the center [3,4]. A schematic illustration of chip warpage and some of the resulting defects are shown in Figure 2.1. In HoP, the connections between solder on the board side and the ball are weak, based only on Van der Waals forces. Therefore, when the component encounters large thermal or mechanical stresses during use, HoP defects can cause electrical failure in the component [5]. Solder joints in the center of the packaging may also form bridging defects, which could cause short circuit and component failure.

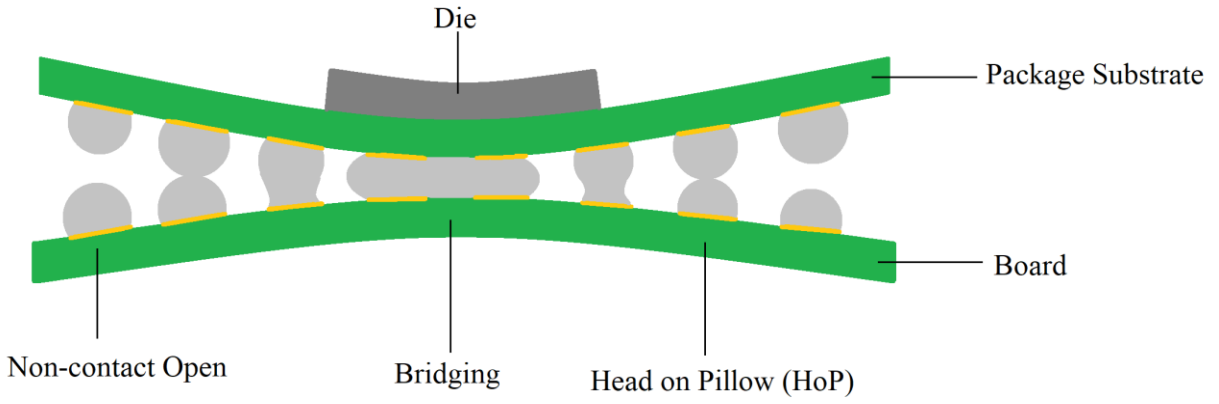

Figure 2.1. Schematic illustration of component warpage and different defects formed during reflow soldering

As a result, low temperature soldering (LTS) systems have been recommended as a solution to reduce heating-induced warpage [6-13]. Solders based on eutectic Sn-Bi alloys are popular candidates for low temperature soldering due to their low eutectic temperature [14], as well as low cost and toxicity. Two different use modes of the low-temperature Sn-Bi alloys are being considered: (1) Sn-Bi alloy solder paste used instead of Sn-Ag-Cu solder paste to assemble components with Sn-Ag-Cu solder balls to form "hybrid" joints after soldering, as shown in Figure 2.2 and (2) both the ball and the paste are Sn-Bi alloys to form homogeneous joints after reflow, as shown in Figure 2.3. For both use modes, assembly necessitates initial balling of the component, followed by melting of Sn-Bi alloy pastes to attach the component to the board. For the Sn-Bi eutectic alloy with a eutectic melting temperature of 139°C, a reflow temperature of approximately

160-190°C is required, lowering the peak reflow temperature by 50-80°C relative to the Sn-Ag-Cu alloy reflow.

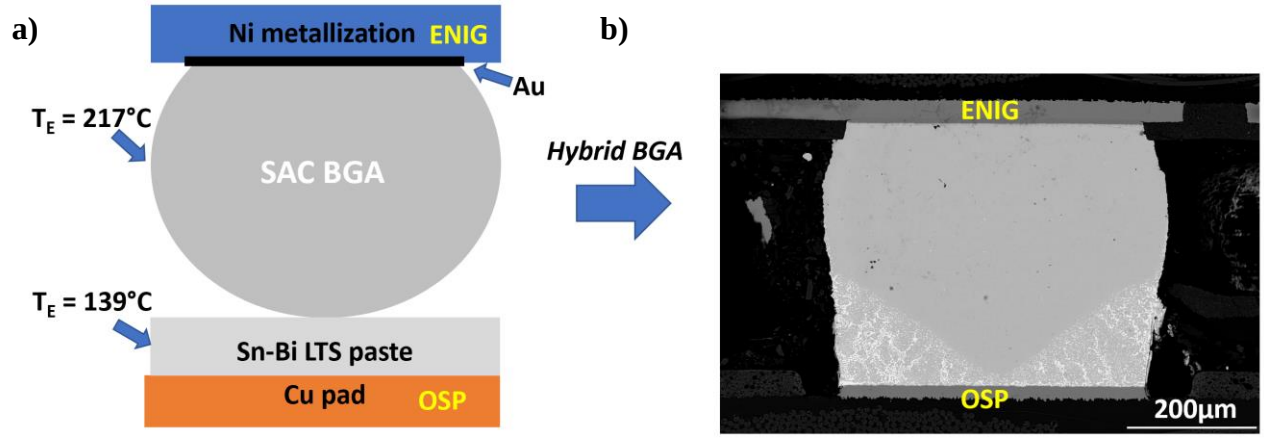

Figure 2.2. a) A schematic illustration of hybrid joints before reflow, where Sn-Bi LTS paste replaces Sn-Ag-Cu solder paste during surface mount procedure; b) typical microstructure of a Sn-Bi LTS-Sn-Ag-Cu hybrid joint after reflow showing the Bi diffusion region and the un-melted Sn-Ag-Cu solder ball region

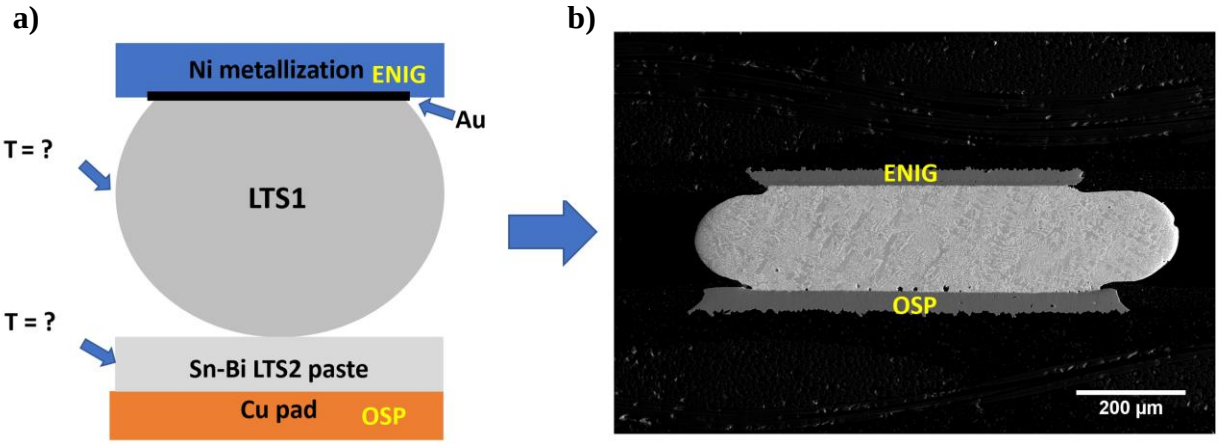

Figure 2.3. a) A schematic illustration of Sn-Bi homogeneous joints before reflow, where Sn-Bi LTS paste substitutes both Sn-Ag-Cu solder paste and Sn-Ag-Cu solder ball during surface mount procedure; b) microstructure of a Sn-57Bi-1Ag homogeneous joint after reflow

To understand the reliability of both hybrid as well as homogeneous low temperature solder joints, it is critical to examine the intermetallic compound stability and growth with different surface finishes because of the introduction of Bi into the system. Existing literature has studied

intermetallic compound growth with Sn-Bi alloys on different surface finishes, including Sn-Bi and Sn-Bi-Ag solders on Cu [15-19], ENIG [15,18,20-22], Ni [16,17,22-25], and ENEPIG [15,18,20,26] surfaces. Li et al. annealed Sn-Bi solders on Cu [27], Ni [28,29], and ENIG [28,29] at 240°C, 100°C above the Sn-Bi eutectic temperature. For Sn-Bi solders on Cu, intermetallic compounds Cu_6Sn_5 and Cu_3Sn formed at the solder-surface finish interface during 240°C annealing, with two different growth rates observed depending on the annealing time. This difference in growth rate reflects a change in mechanism of intermetallic growth [27]. For Sn-Bi solders on Ni substrates, Ni_3Sn_4 forms along the interface during annealing at 240°C [28,29], while Sn-Bi solders in contact with ENIG surface finish result in the formation of Ni_3Sn_4 and Ni_3P intermetallic compounds at the solder-surface finish interface during annealing at 240°C [28,29]. However, most of the previous research mainly focused on the intermetallic compound growth at either very high temperature (above the Sn-Bi eutectic temperature) or low application temperatures (room temperature, 85°C, 100°C). Few studies appear to have considered the influence of surface finish on the intermetallic compound growth in Sn-Bi solders under harsh, solid-state aging environments (homologous temperatures > 0.75), supported growth observations with thermodynamic simulations, measured the order of intermetallic growth with isothermal annealing, or measured the growth rate of intermetallic compound layer.

In terms of micro-alloying effects in Sn-Bi solders, previous research has studied the influence of alloying addition on solder microstructure and intermetallic compound growth. The addition of Ag into Sn-Bi solders produces Ag_3Sn intermetallic precipitates in the solder matrix, refines the microstructure, and slows down Cu_6Sn_5 growth at solder/Cu interfaces during aging [30-33]. Additions of Cu to Sn-Bi alloys results in the formation of Cu_6Sn_5 particles in the solder matrix and refines the microstructure [34]. Li et al. studied the effects of Al, Cr, Cu, Si, Zn, Ag, Au, Pt and Nb micro-alloying additions on intermetallic compound growth rates at solder/Cu interfaces [27].Their results revealed that additions Al, Cr, Cu, Si, Au, Pt and Nb have no effect on interfacial intermetallic growth, Ag additions slow down Cu_6Sn_5 layer growth during aging at 240°C, and Zn additions slow down intermetallic layer growth by forming the Cu_5Zn_8 phase rather than Cu_6Sn_5 and Cu_3Sn [27]. Research on alloying Sn-Bi solders with Sb [35], Ni [36,37], In [38,39], Co [40], and Zn [41,42] has also been reported for assembly with Cu surface finishes, including in a recent review by Wang et al. [43].

For homogeneous LTS joints, intermetallic compound growth on the component side (ENIG and ENEPEG) is also important for joint reliability. Li et al. studied intermetallic compound growth during high temperature annealing at 240°C for Sn-Bi alloys on Ni and ENIG surface finishes with Al, Cr, Si, Zn, Ag, Au, Ru, Ti, Pt, Nb, and Cu additions [28,29]. Among all the micro-alloying elements, only Cu is effective in slowing down intermetallic layer growth by forming $(Ni,Cu)_6Sn_5$ instead of Ni_3Sn_4 and Ni_3P phases during aging at 240°C [28,29]. However, this research only focused on intermetallic growth on ENIG at very high temperatures (above typical peak reflow temperatures); information about intermetallic compound growth at typical LTS reflow durations and temperatures (180°C) and during solid-state annealing (125°C) are largely missing, as is the resulting mechanical behavior of the solder joints.

To address the above identified gap in the literature, in this study, we characterize intermetallic compound growth in Sn-58Bi and Sn-57Bi-1Ag solder joints on Cu-OSP and ENIG surface finishes under typical LTS reflow durations and peak temperatures (180°C) as well as during solder state annealing at 125°C after reflow. We then relate the resulting microstructures to fatigue life through mechanical tests using a micro-scale precision mechanical tester. Starting from phase equilibrium calculations for Sn-Bi-Cu, Sn-Bi-Ag-Cu, Sn-Bi-Au-Ni, and Sn-Bi-Ag-Au-Ni, intermetallic formation in the bulk solder and at the solder-surface finish interfaces is examined; comparing microstructures and phases after reflow with those after high temperature, solid annealing (125°C). As a further step toward conditions in commercial practice, microstructure evolution and the intermetallic compound growth are characterized in ENIG/Sn-58Bi/Cu-OSP and ENIG-Sn-57Bi-1Ag- solder joints, similar to the materials sets in real joints, with Au-Ni under-bump metallizations on the component side and Cu-OSP on the board side.

2.3 Experimental

The test specimens consist of eight solder joints connecting two FR4 boards custom[1]. Figure 2.4 a) shows the configuration and dimensions of the test specimens. The FR4 substrates are single layer PCBs with mask-defined copper pads with ENIG or Cu-OSP surface finish. The. The solder joints were assembled by reflowing 500 μm diameter Sn-58Bi or Sn-57Bi-1Ag solder balls[2] . The samples were assembled using a tabletop reflow oven (DDM Novastar GF-12HC-HT 3-zone). For

[1] Bay Area Circuits, Fremont, CA 94538, USA.
[2] Scientific Alloys Corporation, Clifton, NJ 07011.

both alloys, a maximum temperature of 180°C was used with 90 seconds of time-above-liquidus (139°C). After reflow, the standoff height was measured on solder joint cross-sections using scanning electron microscopy (SEM, Quanta 650 FEG,) After assembly, the test specimens were stored at -10°C to slow any microstructural aging. To study the microstructure evolution during solid state annealing, the test specimens were annealed in air at 125°C for up to 250 h (Fisher Scientific 725F annealing furnace.) The microstructure evolution and fracture paths were determined from SEM images. The thicknesses of the intermetallic compound layers were measured using the average length of 20 line intercepts of individual intermetallic compound layers from multiple SEM images. The intermetallic phases were identified by the relative concentrations of Ni, Cu, Au, and Sn in the intermetallics by EDS. Solder joints were also analyzed by 3D x-ray microscopy (Zeiss Xradia 510 Versa) at a pixel edge length resolution of 2.51 microns and a field of view of 2.54 mm. The analysis for the different materials were performed at a voltage of 60, with an in-situ system temperature of ~28°C. Object Research Systems (ORS) Dragonfly Pro software is used to visualize and analyze the data.

Isothermal sections and solidification paths of Sn-Bi-Ni, Sn-Bi-Cu, Sn-Bi-Ag, and Sn-Ni-Au systems were calculated using the Thermo-Calc software (2020a version) with the TCSLD3 solder alloys database.

Displacement-controlled shear fatigue tests were performed on the test specimens until failure using a custom-built micro-precision mechanical tester, as shown as schematic illustration in Figure 2.4 b) (described in detail in reference [44]). The test specimen displacement for the tester is measured with a capacitance sensor (resolution 7nm) mounted near the test specimen. The capacitance sensor displacement measurement is used for closed-loop control of the tester to ensure that the desired displacement and displacement rate is imposed on the test specimen. This feature is critical for solder alloy characterization due to most alloys' viscoplastic behavior at room temperature, i.e., the stress response of solder alloys depend on the applied strain rate. Shear fatigue tests were performed at 30°C. The displacement profile consists of a 0.20 µm/s ramp up (7.7×10^{-4} s^{-1} strain rate) to 39 µm (15% strain) followed by a 200 seconds dwell, a 0.20 µm/s ramp down (7.7×10^{-4} s^{-1} strain rate) to 0 µm (0% strain), and another 200 s dwell. The displacement profile, though applied isothermally, is inspired by the on/off cycle experienced in electronic assemblies. The displacement profile is repeated until the test specimen has failed or after the test has run for 24 h. The first ramp up is identical to a monotonic test at 7.7×10^{-4} s^{-1}. The equivalent stress, σ,

and equivalent strain, ε, for the test specimens are estimated using established isotropic behavioral assumption as is common in mechanical characterization (see for instance [45]):

$$\sigma=(\sqrt{3}\ F)/A$$

$$\varepsilon=\delta/(\sqrt{3}\ h)$$

where F is the measured shear load, A is the total pad area, δ is the shear displacement, and h is the standoff height.

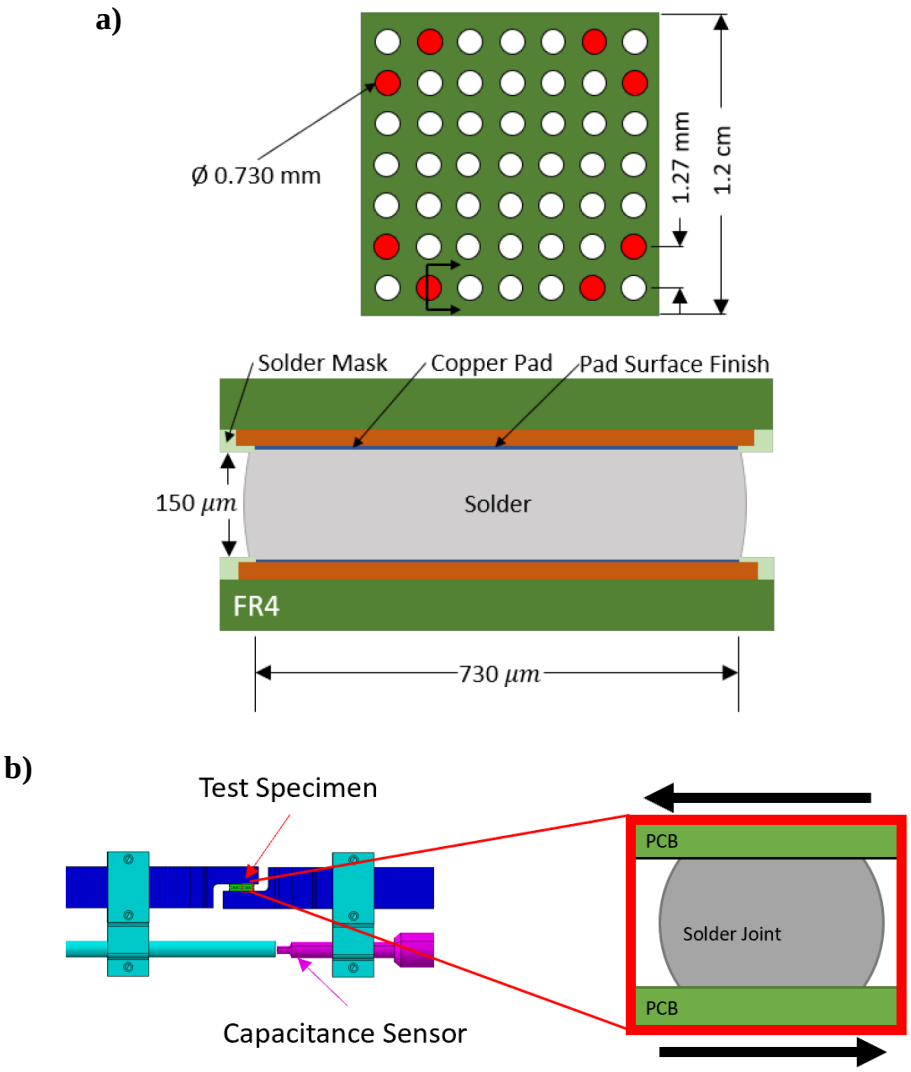

Figure 2.4. Schematic illustration of a) Sn-58Bi and Sn-57Bi-1Ag solder test specimens with 730 μm diameter pads arranged in a 7 x 7, 1.27 mm pitch grid. The eight red circles indicate the locations of the solder joints in the top view of the printed circuit board (top). Schematic cross section of an assembled single solder joint (bottom); and b) schematic illustration of the mechanical tester for shear testing

2.4 Results and Discussion

2.4.1 Thermodynamic Calculations of Intermetallic Compound Growth during Reflow/Solidification and Solid-state Annealing

Phase equilibrium calculations give insight into the expected phases within the bulk solder and at the solder-surface finish interfaces during reflow (melting at 180˚C and solidification to room temperature) and subsequent annealing at 125˚C. In the following analysis, isothermal sections are calculated and single point ThermoCalc calculations are performed using the bulk solder compositions to identify the phases formed during melting and after solidification. Phase formation at the interfaces is characterized by starting with the bulk compositions and identifying what additional phases and their compositions are expected when the solders come in contact with ENIG and Cu-OSP and dissolve Au+Ni and Cu, respectively. The solder joints form from solders of the initial alloy compositions (Sn-58Bi eutectic or Sn-57Bi-1Ag) in contact with ENIG (50nm Au/4um Ni, thick Cu) or Cu (Cu-OSP) so there are different conditions in the bulk solder and at the solder-surface finish interfaces that can be examined using the assumptions of local equilibrium. (Ternary isothermal sections are provided in the Supplementary Materials for reference.)

Sn-58Bi and Sn-57Bi-1Ag on Cu-OSP

Reflow of Sn-58Bi in contact with Cu-OSP at 180˚C leads to the formation of liquid solder with Cu dissolved into the liquid up to a 0.03wt% maximum solubility of Cu. For Sn-57Bi-1Ag, the solubility limit of Ag in the liquid solder at 180˚C is estimated to be 0.8wt% Ag, leaving 0.2wt%Ag as undissolved Ag3Sn, present as 0.4 at% Ag_3Sn (0.3wt%, 0.3vol%) in the liquid solder. The phase at the liquid solder/Cu interface is expected to be Cu_6Sn_5, with Cu_3Sn forming between Cu_6Sn_5 and Cu. During solidification, (Sn), (Bi), and Cu_6Sn_5 are expected to form in Sn-58Bi on Cu-OSP; for Sn-57Bi-1Ag, the phases are (Sn), (Bi), Cu_6Sn_5, and Ag_3Sn, with the fraction of Ag_3Sn increasing on solidification. With annealing at 125˚C, there are no additional phases found.

Sn-58Bi and Sn-57Bi-1Ag on ENIG

During reflow of Sn-58Bi and Sn-57Bi-1Ag on ENIG at 180˚C, Au and Ni from the ENIG surface finish dissolve into the liquid solder. With the measured 50nm Au thicknesses from two ENIG surface finished pads and the solder volumes in this study, the liquid solder contains 0.14wt%

of Au. The solubility limit of Ni in Sn-58Bi eutectic and Sn-57Bi-1Ag is estimated to be < 0.01wt% Ni. At the interface between the liquid solders of both compositions and the electroless Ni(P) layer, Ni_3Sn_4 is expected to form with a Ni_3P layer forming between Ni_3Sn_4 and the electroless Ni(P) layer due to the low solubility of P in Ni_3Sn_4. During solidification of Sn-58Bi eutectic on ENIG, (Sn), (Bi), and $(Ni,Au)Sn_4$ form in the bulk solder, with the Ni in solution in $(Ni,Au)Sn_4$ leading to a Ni:Au ratio (mole basis) of 1:4. For solidification of Sn-57Bi-1Ag on ENIG, (Sn), (Bi), $(Ni,Au)Sn_4$, and Ag_3Sn are expected in the bulk, with Ag_3Sn at 2at% (1.4wt%, 0.8vol%) in the bulk solder. For annealing at 125 ˚C, the expected phases in the bulk at equilibrium are (Sn), (Bi), $(Ni,Au)Sn_4$ for Sn-58Bi and (Sn), (Bi), Ag_3Sn, and $(Ni,Au)Sn_4$ for Sn-57Bi-1Ag. For the reaction at the interface between the bulk solder and Ni_3Sn_4, it is expected that $(Ni,Au)Sn_4$ in the bulk dissolves and precipitates at the interface where additional Ni is provided by diffusion from Ni_3Sn_4. It is expected that $(Ni,Au)Sn_4$ will continue to grow at the interface until it reaches the maximum Ni:Au ratio of approximately 2:3. For the solder joints used here and a Au concentration in the solder of 0.14wt%, the maximum thickness of $(Ni,Au)Sn_4$ at the interface with Ni(P) would be 0.58μm.

Sn-58Bi and Sn-57Bi-1Ag on ENIG (one side) and Cu-OSP (other side)

In typical ball-grid array assemblies, a Ni-based surface finish is typically used on the component side, while Cu-OSP is used on the board side. There are two possible scenarios depending on the order of soldering. If the ENIG board is soldered first, Ni_3Sn_4 is expected to form at the solder/Ni interface and the 50nm Au layer dissolves into the liquid and precipitates as $AuSn_4$ in the bulk during solidification. For the second reflow to attach the Cu-OSP board, Cu is expected to dissolve into the solder with a maximum solubility of 0.03wt%Cu, $(Cu,Au)_6Sn_5$ is expected to form at the solder/Cu interface, and $(Cu,Ni,Au)_6Sn_5$ may form on the pre-existing Ni_3Sn_4 layer on the ENIG side. If the Cu-OSP board is soldered first, Cu_6Sn_5 is expected to form at the solder/Cu interface; with second reflow to attach the ENIG board, $(Cu,Ni)_6Sn_5$ is expected to form with a thinner layer of Ni_3Sn_4 adjacent to the Ni(P) than in the first scenario.

2.4.2 Microstructure Evolution Experiments

Sn-58Bi and Sn-57Bi-1Ag on Cu-OSP

The phases observed on Cu-OSP are those predicted by ThermoCalc in agreement with previous studies [13-17, 25]. Typical microstructures of Sn-58Bi solder on Cu-OSP surface finish after reflow and after solid-state and solid annealing at 125˚C are shown in Figure 2.5. After reflow, the solder showed good wetting with the Cu-OSP metallization, and a facetted polycrystalline layer of Cu_6Sn_5 at the Sn-58Bi/Cu interface. As noted above, thermodynamic calculations estimated that Cu dissolution into the liquid was possible up to a maximum solubility of 0.03wt% Cu, however no Cu_6Sn_5 was observed in the bulk after solidification. During solid-state annealing, Cu_6Sn_5 layer growth along the solder/Cu-OSP interface and fast Bi coarsening within the eutectic were observed in the joints. Similar Cu_6Sn_5 interface morphologies were seen in Cu-OSP/Sn-57Bi-1Ag/Cu-OSP joints (Figure 2.5), however with a finer microstructure than Cu-OSP/Sn-58Bi/Cu-OSP joints. During solid-state annealing, both the Cu_6Sn_5 growth rate and the Bi coarsening rate during solid-state annealing process were slower with the Sn-57Bi-1Ag alloy than eutectic Sn-58Bi, as shown in Figure 2.6.

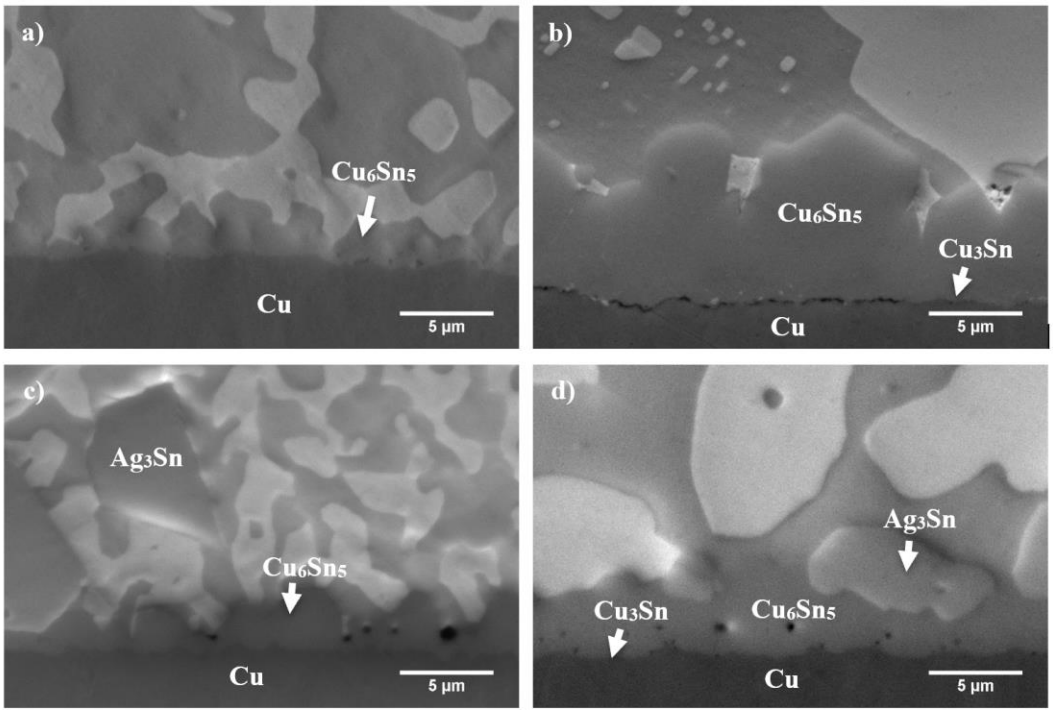

Figure 2.5. Microstructures of Sn-58Bi/Cu interface of Cu-OSP/Sn-58Bi/Cu-OSP a) after reflow and b) after 250 h of solid-state annealing at 125˚C. and Sn-57Bi-1Ag/Cu interface of Cu-OSP/Sn-57Bi-1Ag/Cu-OSP c) after reflow and d) after 250 h of solid-state annealing at 125˚C

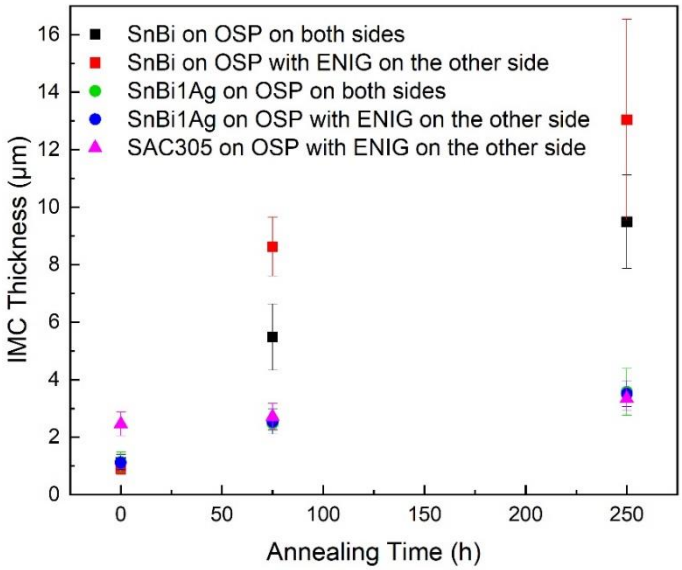

Figure 2.6. Intermetallic compound layer thickness as a function of annealing time at 125°C for Sn-58Bi and Sn-57Bi-1Ag solders on boards with Cu-OSP- Cu-OSP and Cu-OSP-ENIG surface finishes

Sn-58Bi and Sn-57Bi-1Ag on ENIG

The microstructures of the Sn-58Bi homogeneous joints on ENIG surface finish are shown in Figure 2.7. After reflow, the Sn-58Bi homogeneous joints showed good wetting on ENIG surface finishes with a thin layer of Ni_3Sn_4 at the solder-ENIG interface, significantly thinner than the Cu_6Sn_5 formed with Cu-OSP. With Au from ENIG surface finish, $AuSn_4$ particles were also observed in the bulk solder after reflow. However, after 75 h and 250 h of solid-state annealing at 125˚C of ENIG/Sn-58Bi/ENIG solder interconnects, significant $(Ni,Au)Sn_4$ intermetallic growth occurred at the interface between the solder and Ni_3Sn_4. Coarsening of the eutectic within the bulk solder was also observed. An approximately 40µm thick layer of $(Ni,Au)Sn_4$ formed after 75 h of annealing at 125˚C, with the thickness increasing to approximately 50µm after 250 h of annealing, shown in Figure 2.8. The $(Ni,Au)Sn_4$ microstructures are largely columnar, with Bi appearing to wet the grain boundaries of the columnar grains shown in Figure 2.8e) and Figure 2.8f). The intermetallic layers in aged ENIG-Sn-58Bi-ENIG is highly porous, as seen in Figure 2.8. Imaging by 3D x-ray microscopy without cross-sectioning confirmed the formation of voids in the joint as seen in Figure 2.9. As seen in Figure 2.8e) and 2.8f), there is a multi-phase, three-layer structure

after annealing: a thick layer of (Ni,Au)Sn_4, a thin layer of Ni_3Sn_4 and a Ni_2P layer in contact with the Ni(P) surface finish. The P-rich layer forms due to Ni consumption by intermetallic formation and no detectable solubility of P in Ni_3Sn_4. The bright vertical regions in the Ni-P layer are possibly $Ni_{10}P_3Sn_5$, a ternary intermetallic compound reported by Schmetterer et al. [46]

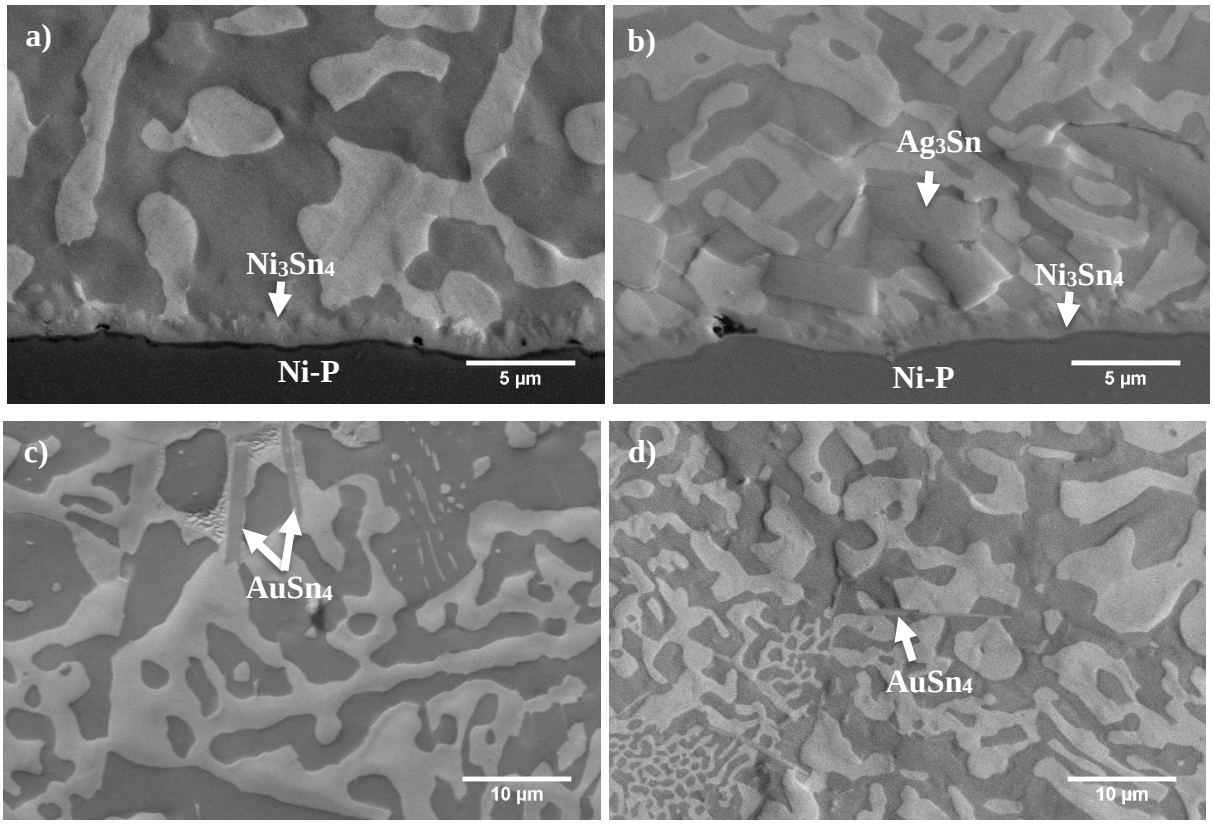

Figure 2.7. Microstructure after reflow of interfacial intermetallic layers for a) ENIG/Sn-58Bi/ENIG; b) ENIG/Sn-57Bi-1Ag/ENIG; and microstructure in the bulk solder showing AuSn4 for c) ENIG/Sn-58Bi/ENIG; and d) ENIG/Sn-57Bi-1Ag/ENIG

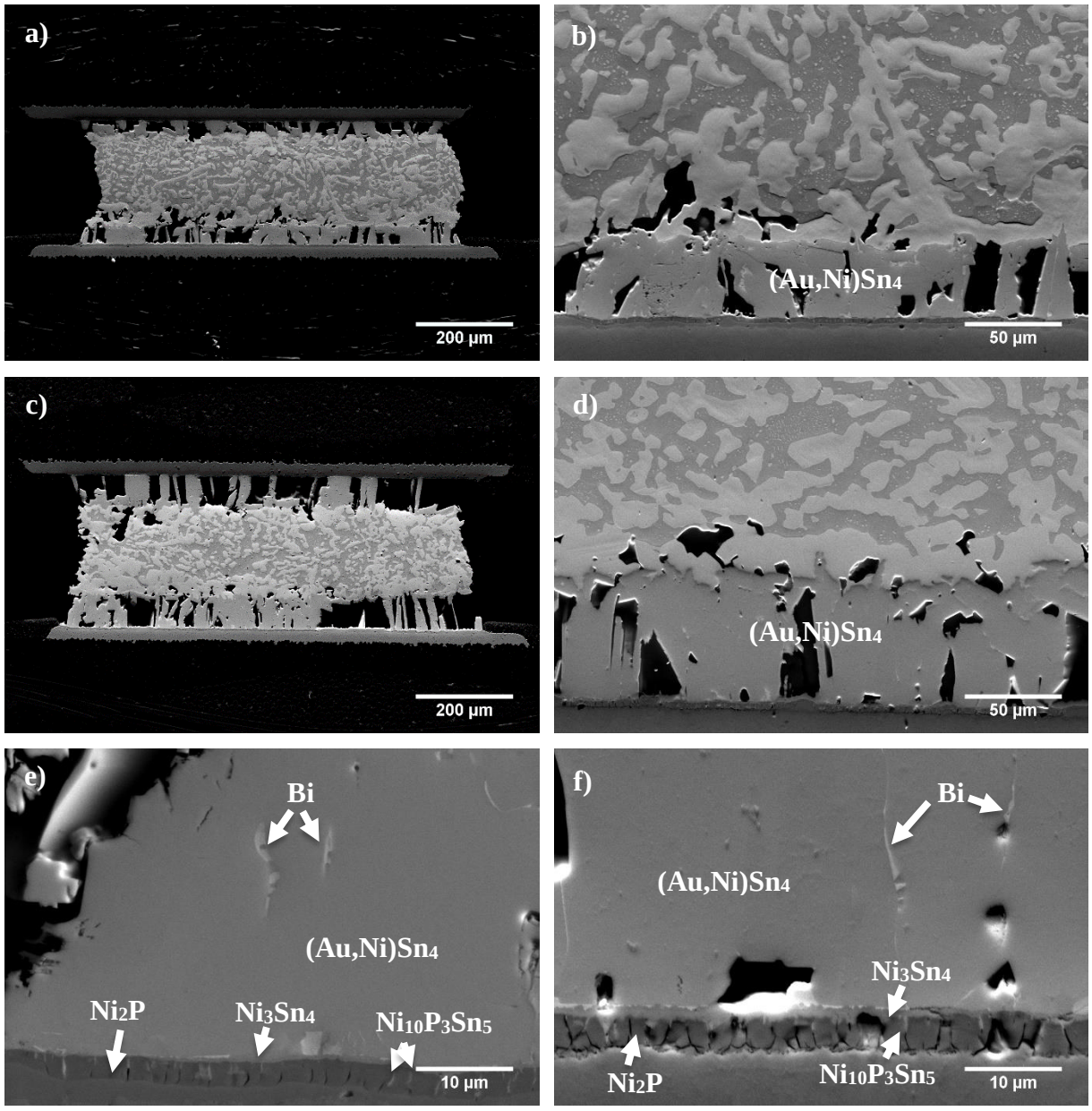

Figure 2.8. Microstructures after solid state annealing at 125˚C: a) ENIG/Sn-58Bi/ENIG after 75 h annealing; b) higher magnification image of a); c) ENIG/Sn-58Bi/ENIG after 250 h annealing; d) higher magnification image of c). Higher magnification images of interfacial layer structures of ENIG/Sn-58Bi/ENIG solder interconnects showing Bi wetting along (Ni,Au)Sn_4 grain boundaries after e) 75 h annealing and f) 250 h annealing

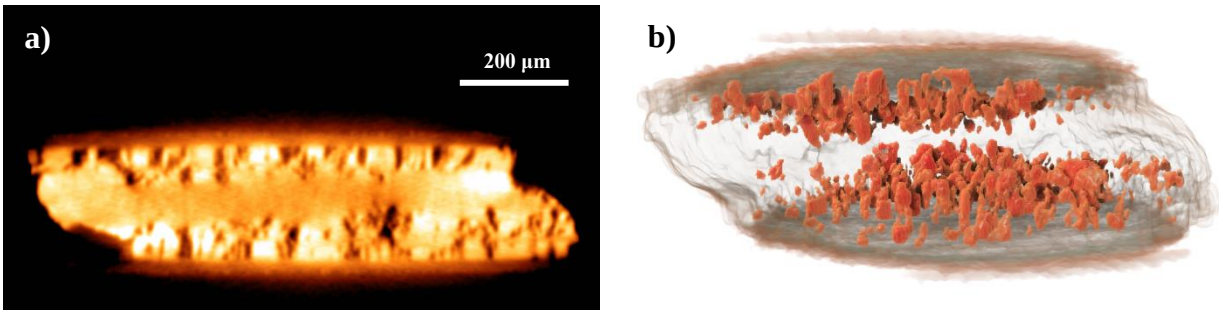

Figure 2.9. 3D x-ray microscope images of ENIG/Sn-58Bi/ENIG solder joint after annealing at 125°C, a) a cross-section of the solder interconnect showing large voids (black regions) formed inside the $(Ni,Au)Sn_4$ during annealing; b) 3-D reconstruction of the solder joint, with the large voids formed inside the $(Ni,Au)Sn_4$ shown in orange.

For Sn-57Bi-1Ag homogeneous joints on ENIG surface finish, Ni_3Sn_4 is the only interfacial IMC phase found at the solder/Ni interface after reflow. As shown in Figure 2.10, after 75 h of aging at 125˚C, a discontinuous $(Ni,Au)Sn_4$ layer has formed on the Ni_3Sn_4 layer. After 250 h of aging, continuous layers of $(Ni,Au)Sn_4$ and Ni_3Sn_4 were observed but $(Ni,Au)Sn_4$ grows significantly more slowly than with Sn-58Bi and with less porosity than Sn-58Bi as seen in Figure 2.10 and in 3D x-ray microscope images.

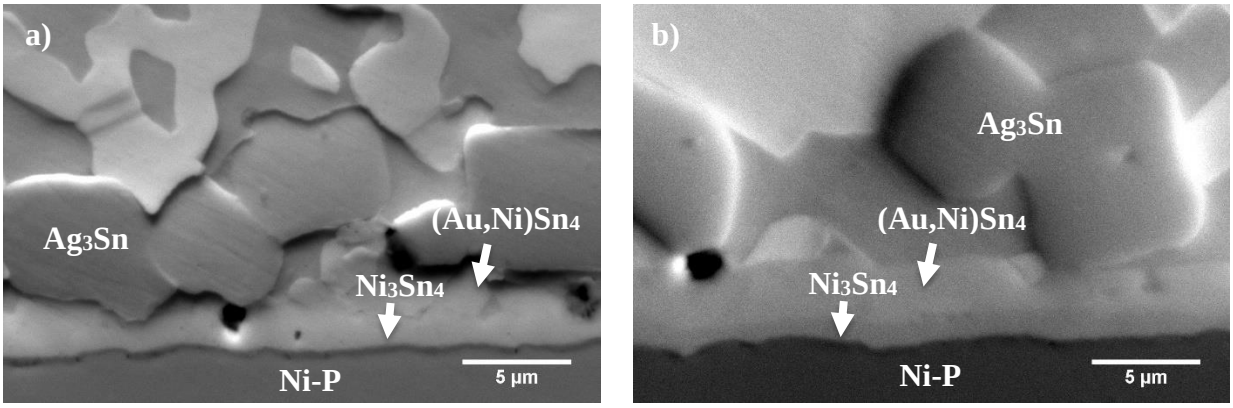

Figure 2.10. Microstructure of Sn-57Bi-1Ag-Ni interface of ENIG-Sn-57Bi-1Ag-ENIG after annealing at 125˚C for a) 75 h and b) 250 h

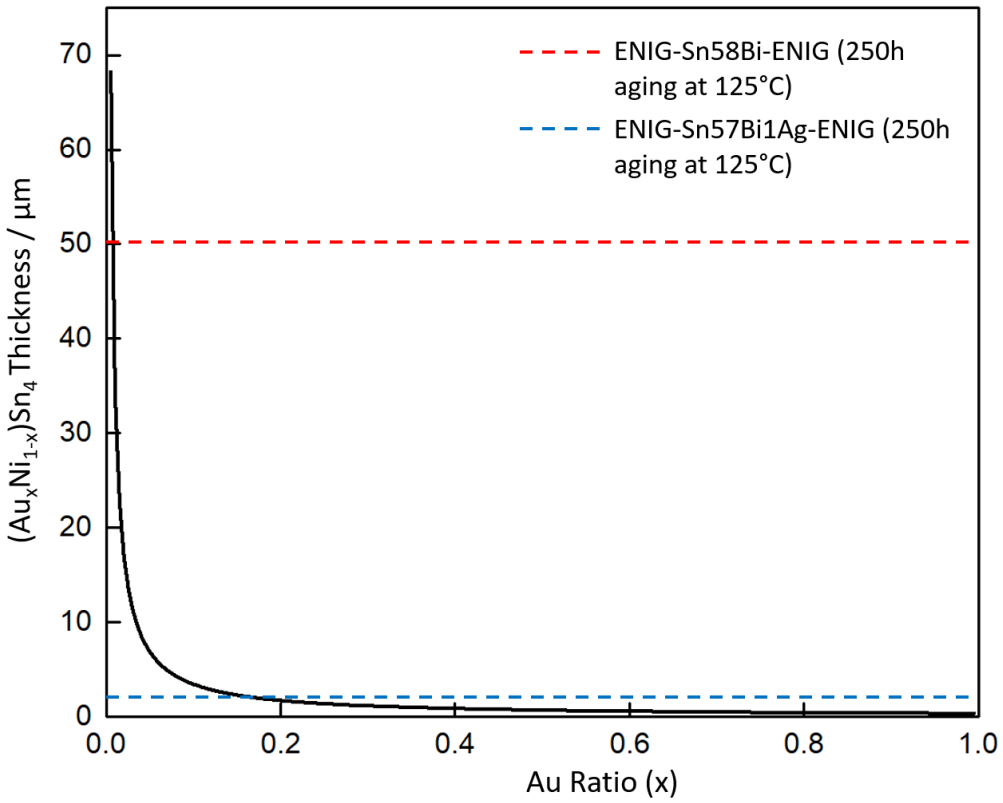

Figure 2.11. Theoretical $(Ni_{1-x}Au_x)Sn_4$ layer thickness as a function of x, the Au fraction, The top dotted line is the observed thickness after 250h aging of Sn-58Bi on ENIG at 125˚C; the bottom dotted line is for Sn-57Bi-1Ag on ENIG for the same conditions

To understand the role of the 50nm Au layer in $(Ni,Au)Sn_4$ growth on ENIG, the Au concentrations expected in the IMC layer as a function of layer thickness were calculated as shown in Fig 11, assuming that all Au from the surface finish is contained in the $(Au_xNi_{1-x})Sn_4$ IMC layer. The thicknesses of ENIG/Sn-58Bi/ENIG and ENIG/Sn-57Bi-1Ag/ENIG joints after 250 h of aging at 125°C are 50µm and 4µm, respectively, are indicated by the dotted lines on Figure 2.11. For the ENIG/Sn-58Bi/ENIG joint, a 50µm IMC layer thickness corresponds to a Au fraction of 0.006, which translates to 0.12% Au, far below the EDS detection limit. For the ENIG-Sn-57Bi-1Ag-ENIG joint, the thickness of the $(Ni_{1-x}Au_x)Sn_4$ layer was 2µm. As shown in Fig 11, a thickness of 2µm corresponds to an Au fraction of 0.17, which translates to 3.4at% Au. According to EDS, the Au concentration in $(Ni_{1-x}Au_x)Sn_4$ in the ENIG/Sn-57Bi-1Ag/ENIG joint after 250h was 2.6 at% Au, in reasonable agreement with the calculation.

The microstructure of ENIG/Sn-58Bi/ENIG and ENIG-Sn-57Bi-1Ag-ENIG joints and calculated Au concentrations in the $(Au_xNi_{1-x})Sn_4$ indicate that (Au, Ni)Sn_4 that formed in the bulk solder after reflow diffuses to the solder/Ni interface during aging at 125˚C to form (Ni,Au)Sn_4. The intermetallic phase $NiSn_4$ is not a stable phase in the binary Ni-Sn phase diagram. It is stable in the Au-Bi-Ni-Sn and the Au-Ni-Sn systems in the range of Ni:Au ratios in (Ni,Au) Sn_4 at 125˚C from 0:1 to 2:3 (Au fractions from 100% to 60%.) If the (Ni,Au)Sn_4 had stopped growing when the Ni:Au ratio reached the maximum predicted solubility, the maximum thickness observed would have been 0.58μm, far from 50 μm and 1000:7 ratio observed here for ENIG/Sn-58Bi/ENIG. That Au from the ENIG surface finish catalyzed the reaction is indicated from complementary experiments performed without the 50nm Au in which no (Ni,Au)Sn_4 formed during annealing. From the literature, it appears that $NiSn_4$ is a marginally unstable phase, which has been observed after in other solder systems with and without Au. [47]

2.4.3 Ag_3Sn Effect on Interfacial Intermetallic Growth Rate and Bi Coarsening for Sn-Bi Solders

According to the results from the previous section, Ag addition into Sn-Bi solder was observed to significantly suppress the interfacial IMC growth on both ENIG and Cu-OSP surface finishes. Previous studies [31] suggested that with Ag addition, Ag_3Sn serves as diffusion barrier between Sn and surface metallization, thereby slowing down the intermetallic compound layer growth during aging. However, according to the microstructures shown in Figure 2.10 of the previous section, Ag_3Sn forms as large isolated particles that are in a line parallel to the solder-intermetallic interface. Furthermore, Ag_3Sn particles were frequently observed only on one side of the sandwich structures, as shown in Figure 2.12. If Ag_3Sn served as diffusion barrier between Sn and surface metallization, the intermetallic growth rate should be faster on the Ag_3Sn-segregated side of the joint. In addition, it is expected that interfacial IMC on the interface that had been subjected to two reflows would be thicker than after a single reflow. Finally, it is expected that there would be a gravity effect. To separate these effects, the presence of Ag_3Sn particles at the interfaces and IMC interfacial growth were measured at both interfaces after reflow and aging, keeping track of the number of reflows and controlling the orientation of the structures during reflow, as summarized in Table 2.1. The results showed that there is negligible difference between the intermetallic compound layer during aging on two sides of the joints. The intermetallic compound layer

thickness is even smaller on the Ag_3Sn-depleted side than Ag_3Sn-segregated side of the joint. Therefore, Ag_3Sn particles do not have the effect on inhibiting the diffusion between Sn and the surface finish. Ag effects on intermetallic compound layer growth should be further studied.

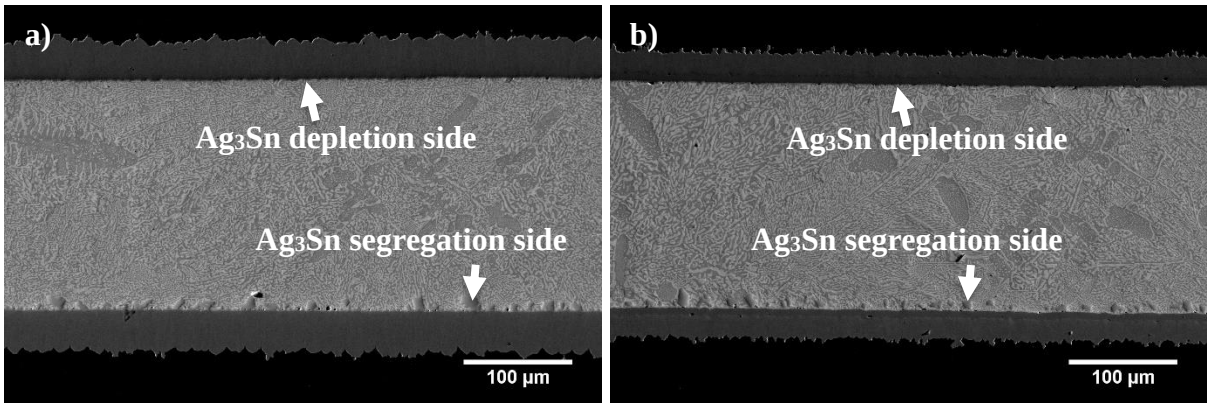

Figure 2.12. Microstructure of a) Cu- OSP-Sn-57Bi-1Ag- Cu-OSP solder joint after reflow showing Ag_3Sn segregation on one side of the joint; and b) ENIG-Sn-57Bi-1Ag-ENIG solder joint after reflow showing Ag_3Sn segregation on one side of the joint

Table 2.1. Intermetallic compound layer thickness in Sn-57Bi-1Ag joints during aging on different sides

Intermetallic compound layer thickness (µm)	As-reflowed	125°C 75 hours	125°C 250 hours
Cu-OSP Ag_3Sn segregation side (Cu_6Sn_5 growth)	1.1	2.5	3.6
Cu-OSP Ag_3Sn depletion side (Cu_6Sn_5 growth)	1.0	2.4	3.5
ENIG Ag_3Sn segregation side (Ni_3Sn_4 growth)	0.9	2.0	3.3
ENIG Ag_3Sn depletion side (Ni_3Sn_4 growth)	0.7	1.7	2.5

According to the microstructure of aged Sn-58Bi and Sn-57Bi-1Ag solder joints, Ag addition also significantly slows down Bi coarsening inside solder during aging, as shown in Figure 2.13 below. Small Ag_3Sn particles were observed in aged Sn-57Bi-1Ag solder matrix, which are much smaller than the size of Ag_3Sn particle near intermetallic compound layer. These finer Ag_3Sn

particles may serve as refining agent in the solder, which might be the reason of the slower coarsening rate of eutectic Bi inside the solder joints.

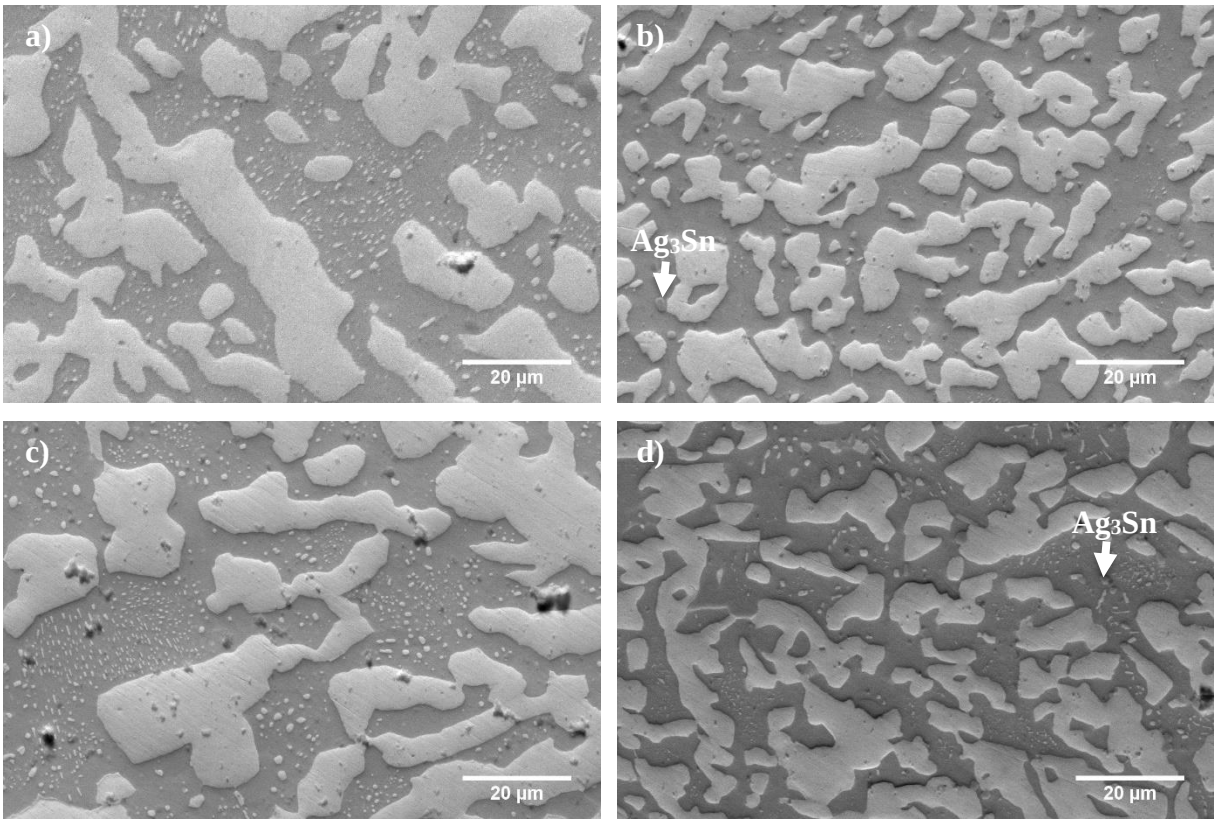

Figure 2.13. Microstructure of coarsened eutectic Bi inside a) Cu-OSP-Sn-58Bi- Cu-OSP; b) Cu-OSP-Sn-58Bi- Cu-OSP; c) ENIG-Sn-57Bi-1Ag-ENIG; and d) ENIG-Sn-57Bi-1Ag-ENIG solder interconnects after 250 hours of aging at 125°C

2.4.4 Mechanical Characterization and Gold Embrittlement Effect in Sn-58Bi and Sn-57Bi-1Ag Solder Interconnects on ENIG

The formation of $(Ni,Au)Sn_4$ significantly embrittles both Sn-58Bi and Sn-57Bi-1Ag solder joints, causing brittle failures inside $(Ni,Au)Sn_4$ layer during fatigue loading, as shown in Figure 2.14. The N_{50} life (numbers of cycles needed for the saturation stress to drop 50% from that of the first cycle) for both alloys on ENIG surface finish after reflow and after 250 h annealing are shown in Figure 2.17. After aging, both ENIG-Sn-58Bi-ENIG and ENIG-Sn-57Bi-1Ag-ENIG solder interconnects failed even before the first fatigue cycle was complete, shown in the stress-strain curve of first fatigue cycle loading of the aged joints in Figure 2.15. Therefore, Au in ENIG surface finish not only catalyzed the formation of $(Ni,Au)Sn_4$ during annealing ,but also embrittled the Sn-

58Bi and Sn-57Bi-1Ag solder joints. A spalling phenomenon was also observed for Sn-58Bi and Sn-57Bi-1Ag on ENIG after solid-state annealing at 125˚C for 250 h in which the Ni(P) surface finish was breached at several points and formed $(Cu,Ni)_6Sn_5$ in a pattern characteristic of similar Ni(P) layer failures with Sn-Ag-Cu alloys.

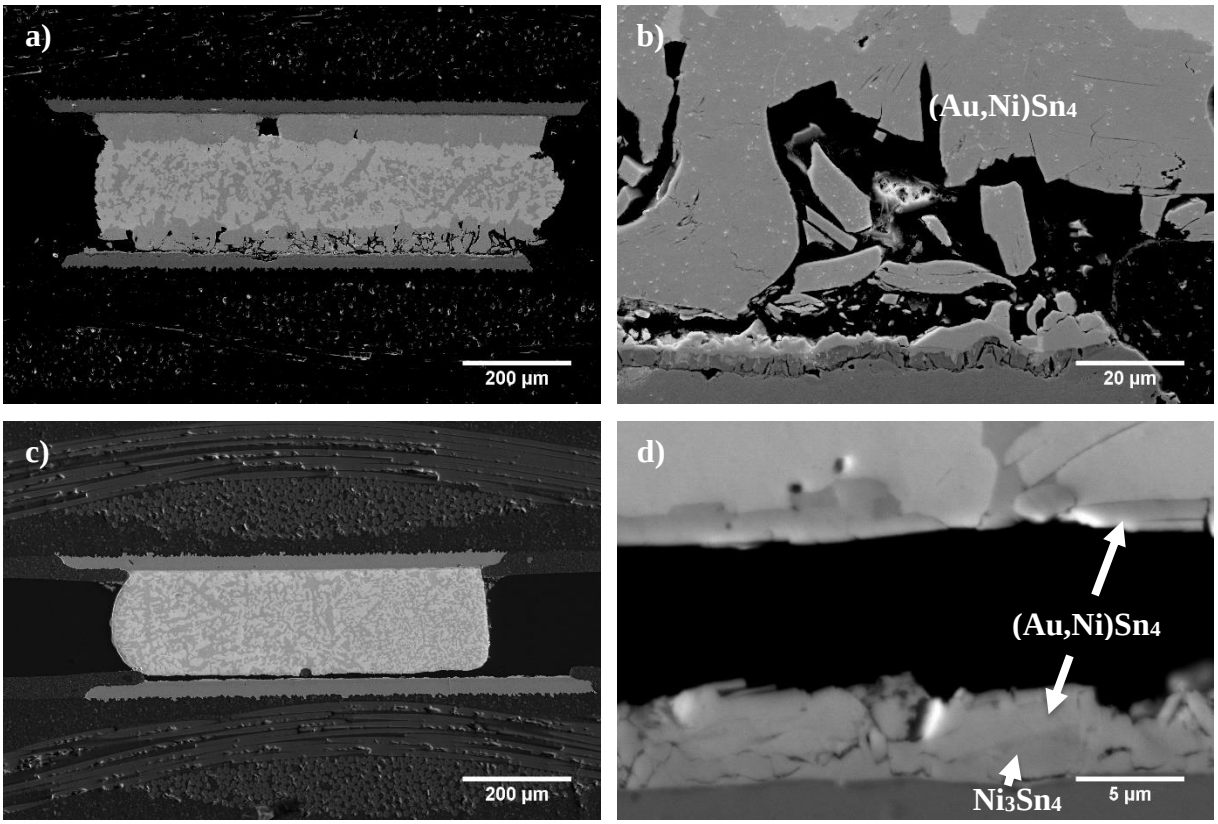

Figure 2.14. Microstructure of a) fatigue-loaded ENIG/Sn-58Bi/ENIG solder interconnects after 250h of solid-state annealing; b) higher magnification image at Sn-58Bi/Ni interface of a) showing the details of the fracture path; c) fatigue-tested ENIG/Sn-57Bi-1Ag/ENIG solder interconnects after 250h of solid-state annealing; and d) higher magnification image at Sn-57Bi-1Ag/Ni interface of c) showing the details of the fracture surface

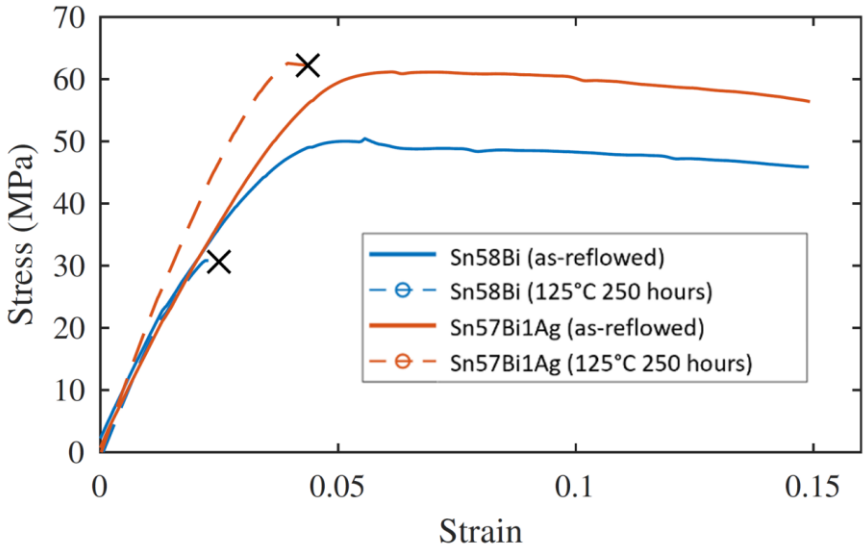

Figure 2.15. Stress-strain curves of first fatigue loading cycle of ENIG/Sn-58Bi/ENIG and ENIG/Sn-57Bi-1Ag/ENIG solder joints after both reflow and 250 h of aging at 125°C

The microstructures of fractured Sn-58Bi and Sn-57Bi-1Ag joints on Cu-OSP surface finish are shown in Figure 2.16. After reflow, ductile fatigue failures were observed in both Sn-58Bi and Sn-57Bi-1Ag, with the cracks in both alloys propagating inside the bulk solder. After annealing at 125˚C, both solder joints still experience ductile fatigue failure, the fracture propagates inside the $(Ni,Au)Sn_4$ layer for aged Sn-58Bi joints, and inside the bulk solder but very close to $(Ni,Au)Sn_4$ in Sn-57Bi-1Ag joints. The fatigue reliability of aged solder joints on Cu-OSP finish is much better than the corresponding ones on ENIG finish. This is attributed to lack of Au embrittlement in joints with Cu-OSP surface finish, as shown in Figure 2.17. Still, the fatigue life of Sn-Bi solder joints on Cu-OSP pad finish is significantly lower than for Sn-3.0Ag-0.5Cu solder joints.

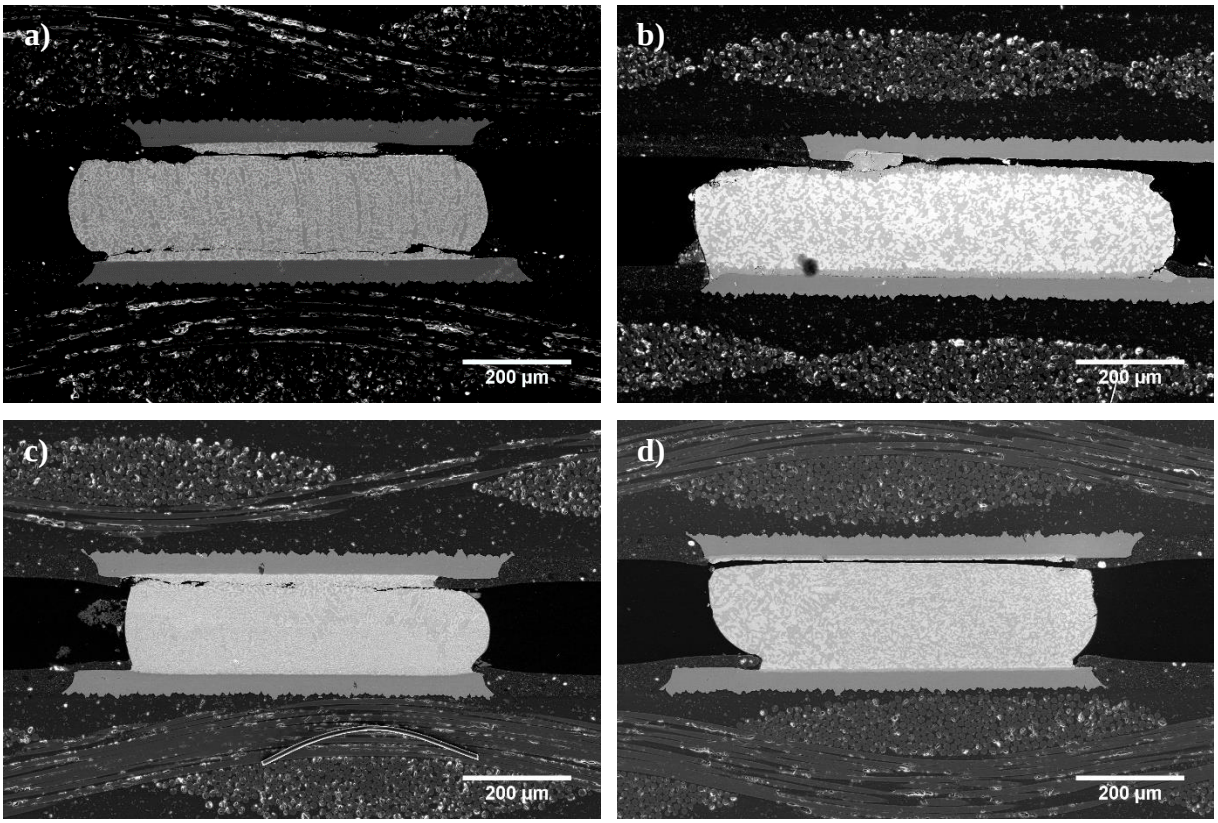

Figure 2.16. Microstructure of fractured solder interconnects after fatigue testing: a) Cu-OSP/Sn-58Bi/Cu-OSP after reflow; b) Cu-OSP/Sn-58Bi/Cu-OSP after 250 h aging at 125°C; c) Cu-OSP/Sn-57Bi-1Ag/Cu-OSP after reflow; and d) Cu-OSP/Sn-57Bi-1Ag/Cu-OSP after 250 h aging at 125°C

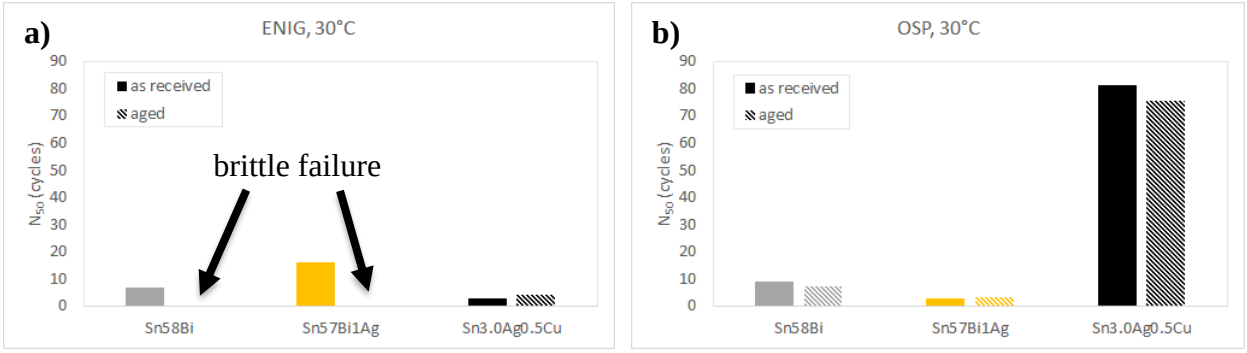

Figure 2.17. Fatigue reliability and N_{50} cycles for Sn-58Bi, Sn-57Bi-1Ag and Sn3.0Ag0.5Cu after reflow and 250 h of aging at 125˚C on a) ENIG and b) Cu-OSP surface finishes

2.4.5 Elimination of (Ni,Au)Sn_4 Formation in Sn-58Bi and Sn-57Bi-1Ag Solder Interconnects

To improve the reliability of the Sn-Bi low temperature solders on ENIG surface finish, (Ni,Au)Sn_4 formation during annealing must be suppressed. From Belyakov and Gourlay's work on Sn-Ag on ENIG, it is well known that microalloying of Cu into Sn-Ag solder causes $(Cu,Ni)_6Sn_5$ to form on ENIG during annealing [48]. To extend this concept to Sn-Bi alloys, Cu was introduced in the joints by dissolution from Cu-OSP using ENIG/Sn-58Bi/Cu-OSP and ENIG/Sn-57Bi-1Ag/Cu-OSP samples. With the low Cu solubility in Sn-58Bi at 180˚C and the short reflow times, it was not certain it would be enough. The microstructures of ENIG/Sn-58Bi/Cu-OSP and ENIG/Sn-57Bi-1Ag/Cu-OSP solder joints after reflow and annealing process are shown in Figure 2.18. Compositional analysis by EDS at Sn-58Bi/Ni and Sn-57Bi-1Ag-Ni interfaces revealed that $(Cu,Ni)_6Sn_5$ formed instead of (Ni,Au)Sn_4 and Ni_3Sn_4 in ENIG/Sn-58Bi/ENIG and ENIG/Sn-57Bi-1Ag/ENIG interconnects after annealing.

2.4.6 Intermetallic Compound Growth Rate Calculation for Sn-58Bi and Sn-57Bi-1Ag Solder Interconnects

Interfacial intermetallic growth as a function of annealing times at 125°C is shown in Figure 2.19 for Sn-58Bi and Sn-57Bi-1Ag with ENIG surface finishes. When one of the substrate finish was changed from ENIG to Cu-OSP, Cu in the pad dissolves into Sn-58Bi and Sn-58Bi1Ag solders during reflow process, eliminating the formation of Ni_3Sn_4 and (Ni,Au)Sn_4 layers, and instead forming $(Cu,Ni)_6Sn_5$. The growth rate of $(Cu,Ni)_6Sn_5$ is also significantly slower. Compared with the IMC growth rate in Sn3.0Ag0.5Cu solder on ENIG metallization, only ENIG-Sn-58Bi-ENIG joints exhibited much faster growth rate, all the other three configurations (ENIG-Sn-58Bi- Cu-OSP, ENIG-Sn-57Bi-1Ag-ENIG and ENIG-Sn-57Bi-1Ag- Cu-OSP) exhibit comparable intermetallic compound growth rate as the Sn3.0Ag0.5Cu solder joints.

The average growth rate constant *k* for Sn-58Bi and Sn-57Bi-1Ag on different surface finishes during aging at 125°C could be calculated using the equation $k = l^2/t$, where *k* is the intermetallic compound growth rate constant, l is increased intermetallic compound layer thickness after annealing, and *t* is the annealing time at 125°C. The estimated growth rate constants for Sn-58Bi and Sn-57Bi-1Ag interconnects are summarized in Tables 2.2 and 2.3. The calculated growth rate constants also correspond with microstructure evolution. For Cu-OSP surface finish, Sn-58Bi has

one order of magnitude higher intermetallic compound growth rate than Sn-57Bi-1Ag. For ENIG surface finish, the growth rate constant of ENIG-Sn-58Bi-ENIG joints is significantly higher than any other configuration.

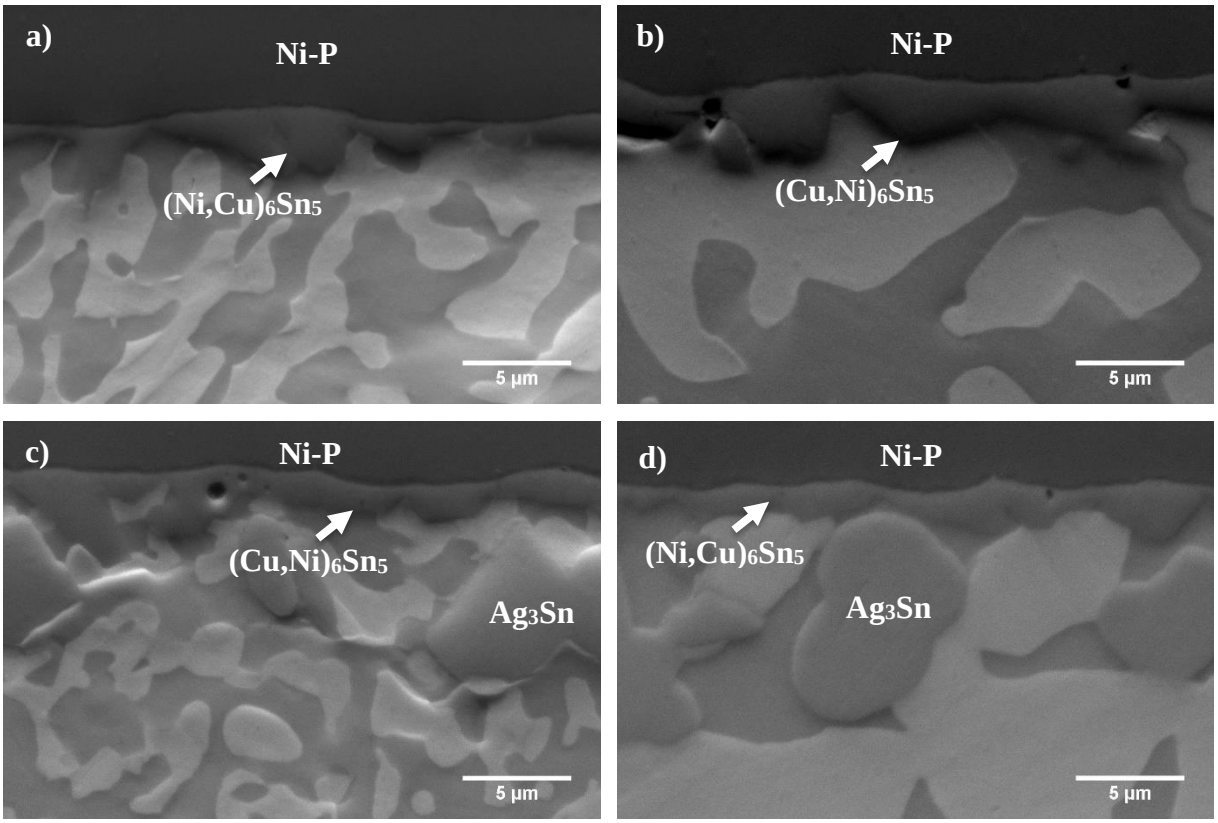

Figure 2.18. Microstructures at a) Sn-58Bi/Ni interface of ENIG/Sn-58Bi/Cu/OSP solder joints after reflow; b) Sn-58Bi/Ni interface of ENIG/Sn-58Bi/Cu-OSP solder interconnects after 250 h of annealing at 125˚C; c) Sn-57Bi-1Ag-Ni interface of ENIG/Sn-57Bi-1Ag/Cu-OSP solder interconnects after reflow; and d) Sn-57Bi-1Ag-Ni interface of ENIG/Sn-57Bi-1Ag/Cu-OSP solder interconnects after 250 h of at 125˚C

a)

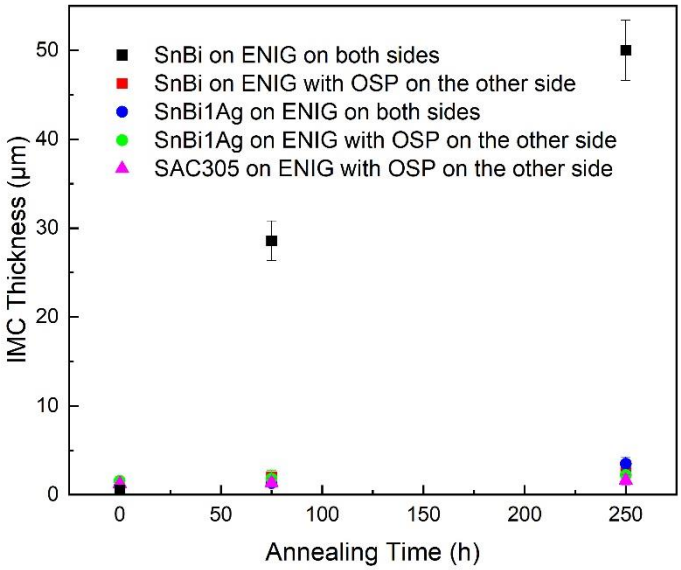

b)

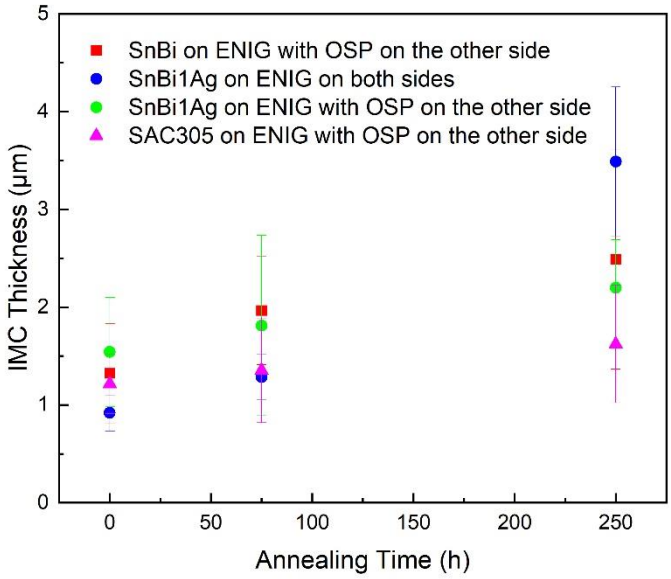

Figure 2.19. Intermetallic compound layer thickness change during solid-state annealing (125°C) for a) Sn-58Bi and Sn-57Bi-1Ag solders on ENIG surface finishes under different configurations, and b) enlarged lower part of Figure 2.19a)

Table 2.2. Summary of intermetallic growth rate constants for Sn-58Bi and Sn-57Bi-1Ag solders on Cu-OSP surface finish with different configurations at 125°C

k ($\mu m^2 \cdot h^{-1}$)	Cu-OSP on both sides	Cu-OSP on one side and ENIG on the other side
Sn-58Bi on OSP	2.67×10^{-1}	6.92×10^{-1}
Sn-57Bi-1Ag on OSP	2.39×10^{-2}	2.51×10^{-2}

Table 2.3. Summary of intermetallic growth rate constants for Sn-58Bi and Sn-57Bi-1Ag solders on ENIG surface finish with different configurations at 125°C

k ($\mu m^2 \cdot h^{-1}$)	ENIG on both sides	ENIG on one side and Cu-OSP on the other side
Sn-58Bi on ENIG	10.3	5.47×10^{-3}
Sn-57Bi-1Ag on ENIG	1.41×10^{-2}	1.36×10^{-3}

2.5 Conclusions

To reduce substrate and component warpage by lowering the reflow temperature, Sn-Bi low temperature solders are promising candidates to replace traditional Sn-Ag-Cu solder joints entirely to form homogeneous joints or to replace Sn-Ag-Cu solder paste to form hybrid joints. In this study the microstructural evolution of Sn-58Bi and Sn-57Bi-1Ag homogeneous joints with ENIG and OSP surface finishes was characterized after reflow and then after annealing at 125˚C, and the effects of interfacial intermetallic formation on mechanical fatigue were characterized. Important results from this study are:

- For Sn-58Bi and Sn-57Bi-1Ag homogeneous joints with Cu-OSP surface finishes, Cu_6Sn_5 and Cu_3Sn form at solder/Cu interfaces during reflow and annealing, with 1wt%Ag in Sn-Bi solders decreasing Cu_6Sn_5 growth during annealing.
- For Sn-58Bi and Sn-57Bi-1Ag homogeneous joints on ENIG surface finishes, Ni_3Sn_4 forms during reflow. However, during solid-state annealing, 50nm Au from the ENIG surface finish catalyzes formation and growth of highly porous $(Ni,Au)Sn_4$ at the Ni_3Sn_4/Ni(P) interface in both Sn-58Bi and Sn-57Bi-1Ag homogeneous joints. Growth of $(Ni,Au)Sn_4$ is significantly faster with Sn-58Bi than with Sn-57Bi-1Ag.
- The $(Ni,Au)Sn_4$ embrittles both Sn-58Bi and Sn-57Bi-1Ag solder joints, causing brittle fracture during the first load cyclic in mechanical fatigue testing, even though the (Ni,Au)Sn4 layer for Sn-57Bi-1Ag was significantly thinner than for Sn-58Bi on ENIG.

- Introducing Cu into Sn-58Bi and Sn-57Bi-1Ag joints even by switching one of the ENIG surface finishes to Cu-OSP stabilizes $(Cu,Ni)_6Sn_5$ formation at the remaining solder/ENIG interface, and reduces this Au-embrittlement effect.
- These results suggest that ENIG surface finishes should be avoided unless the low temperature solder contains sufficient Cu to suppress $(Ni,Au)Sn_4$ formation.

2.6 Acknowledgment

The authors gratefully acknowledge Intel Corporation for supporting this research. The authors acknowledge Chven Mitchell who acquired X-ray microscope images for this paper on a Zeiss Xradia 510 Versa 3D X-ray Microscope purchased through the EVPRP Major Multi-User Equipment Program 2017 at Purdue University.

2.7 References

[1] Li, Y., & Goyal, D. (Eds.). (2017). 3D microelectronic packaging: from fundamentals to applications (Vol. 57). Springer.

[2] Vianco, P., & Neilsen, M. (2021). Processing and Reliability of Solder Interconnections in Stacked Packaging. In 3D Microelectronic Packaging (pp. 471-526). Springer, Singapore.

[3] Bath, J., Garcia, R., Uchida, N., Takahashi, H., Clark, G., & Itoh, M. (2009). Investigation and development of tin-lead and lead-free solder pastes to reduce the head-in-pillow component soldering defect. SMTA International Proceedings 2009.

[4] Boettinger, W. J., Handwerker, C. A., Newbury, B., Pan, T. Y., & Nicholson, J. M. (2002). Mechanism of fillet lifting in Sn-Bi alloys. Journal of electronic materials, 31(5), 545-550.

[5] Henshall, Gregory, Jasbir Bath, and Carol A. Handwerker, eds. Lead-free solder process development. John Wiley & Sons, 2011.

[6] Hua, F., Mei, Z., & Glazer, J. (1998, May). Eutectic Sn-Bi as an alternative to Pb-free solders. In 1998 Proceedings. 48th Electronic Components and Technology Conference (Cat. No. 98CH36206) (pp. 277-283). IEEE.

[7] Ferrer, E., & Holder, H. (2003, March). 57Bi-42Sn-1Ag: A Lead Free, Low Temperature Solder for the Electronic Industry. In JEDEX Conference, San Jose, CA, March (pp. 22-25).

[8] Aspandiar, R., Byrd, K., Tang, K. K., Campbell, L., & Mokler, S. (2015, February). Investigation of low temperature solders to reduce reflow temperature, improve SMT yields and realize energy savings. In Proceedings of the 2015 APEX Conference.

[9] Chen, O. H., Byrd, K., Mokler, S., Tang, K. K., & Aspandiar, R. (2015, May). Comparison of the Mechanical Shock/Drop Reliability of Flip Chip BGA (FCBGA) Solder Joints Formed by Soldering with Low Temperature BiSn-Based Resin Reinforced Solder Pastes. In Proceedings of the International Conference on Soldering and Reliability.

[10] Chen, O. H., Molina, A., Aspandiar, R., Byrd, K., Mokler, S., & Tang, K. K. (2015, September). Mechanical shock and drop reliability evaluation of the BGA solder joint stack-ups formed by reflow soldering SAC solder balls BGAs with BiSnAg and resin reinforced BiSn-based solder pastes. In Proceedings of SMTA International (pp. 215-222).

[11] Mokler, S., Aspandiar, R., Byrd, K., Chen, O., Walwadkar, S., Tang, K. K., ... & Sane, S. (2016, September). The application of Bi-based solders for low temperature reflow to reduce cost while improving SMT yields in client computing systems. In Proceedings of SMTA International (pp. 318-326).

[12] Silva, B. L., Xavier, M. G., Garcia, A., & Spinelli, J. E. (2017). Cu and Ag additions affecting the solidification microstructure and tensile properties of Sn-Bi lead-free solder alloys. Materials Science and Engineering: A, 705, 325-334.

[13] Sahasrabudhe, S., Mokler, S., Renavikar, M., Sane, S., Byrd, K., Brigham, E., ... & Parupalli, S. (2018, May). Low Temperature Solder-A Breakthrough Technology for Surface Mounted Devices. In 2018 IEEE 68th Electronic Components and Technology Conference (ECTC) (pp. 1455-1464). IEEE.

[14] Lee, Byeong-Joo, Chang-Seok Oh, and Jae-Hyeok Shim. "Thermodynamic assessments of the Sn-In and Sn-Bi binary systems." Journal of electronic materials 25.6 (1996): 983-991.

[15] Kim, J. H., Lee, Y. C., Lee, S. M., & Jung, S. B. (2014). Effect of surface finishes on electromigration reliability in eutectic Sn–58Bi solder joints. Microelectronic engineering, 120, 77-84.

[16] Liu, P. L., & Shang, J. K. (2005). Fracture of Sn-Bi/Ni (P) interfaces. Journal of materials research, 20(4), 818-826.

[17] Yoon, J. W., Lee, C. B., & Jung, S. B. (2002). Interfacial reactions between Sn-58 mass% Bi eutectic solder and (Cu, electroless Ni-P/Cu) substrate. Materials transactions, 43(8), 1821-1826.

[18] Lee, S. M., Yoon, J. W., & Jung, S. B. (2015). Interfacial reaction and mechanical properties between low melting temperature Sn–58Bi solder and various surface finishes during reflow reactions. Journal of Materials Science: Materials in Electronics, 26(3), 1649-1660.

[19] Zou, H. F., Zhang, Q. K., & Zhang, Z. F. (2012). Interfacial microstructure and mechanical properties of Sn-Bi/Cu joints by alloying Cu substrate. Materials Science and Engineering: A, 532, 167-177.

[20] Myung, W. R., Kim, Y., Kim, K. Y., & Jung, S. B. (2016). Drop reliability of epoxy-contained Sn-58 wt.% Bi solder joint with ENIG and ENEPIG surface finish under temperature and humidity test. Journal of Electronic Materials, 45(7), 3651-3658.

[21] Chen, L. T., & Chen, C. M. (2006). Electromigration study in the eutectic Sn-Bi solder joint on the Ni/Au metallization. Journal of materials research, 21(4), 962-969.

[22] Young, B. L., Duh, J. G., & Jang, G. Y. (2003). Compound formation for electroplated Ni and electroless Ni in the under-bump metallurgy with Sn-58Bi solder during aging. Journal of electronic materials, 32(12), 1463-1473.

[23] Tao, W. H., Chen, C., Ho, C. E., Chen, W. T., & Kao, C. R. (2001). Selective interfacial reaction between Ni and eutectic BiSn lead-free solder. Chemistry of materials, 13(3), 1051-1056.

[24] Wang, J., Liu, H. S., Liu, L. B., & Jin, Z. P. (2006). Interfacial reaction between Sn-Bi alloy and Ni substrate. Journal of electronic materials, 35(10), 1842-1847.

[25] Chiu, M. Y., Chang, S. Y., Tseng, Y. H., Chan, Y. C., & Chuang, T. H. (2002). Characterization of intermetallic compounds formed during the interfacial reactions of liquid Sn and Sn-58Bi solders with Ni substrates. ZeitschriftfürMetallkunde, 93(3), 248-252.140: SnAgCu, ENIG, IMC

[26] Pun, K. P., Islam, M. N., Rotanson, J., Cheung, C. W., & Chan, A. H. (2018). Enhancement of Sn-Bi-Ag Solder Joints with ENEPIG Surface Finish for Low-Temperature Interconnection. Journal of Electronic Materials, 47(9), 5191-5202.

[27] Li, J. F., Mannan, S. H., Clode, M. P., Whalley, D. C., & Hutt, D. A. (2006). Interfacial reactions between molten Sn–Bi–X solders and Cu substrates for liquid solder interconnects. Acta Materialia, 54(11), 2907-2922.

[28] Li, J., Mannan, S. H., Clode, M. P., Liu, C., Chen, K., Whalley, D. C., ... & Conway, P. P. (2008). Interfacial reaction between molten Sn-Bi based solders and electroless Ni-P coatings for liquid solder interconnects. IEEE Transactions on Components and Packaging Technologies, 31(3), 574-585.

[29] Li, J. F., Mannan, S. H., Clode, M. P., Chen, K., Whalley, D. C., Liu, C., & Hutt, D. A. (2007). Comparison of interfacial reactions of Ni and Ni–P in extended contact with liquid Sn–Bi-based solders. Actamaterialia, 55(2), 737-752.

[30] Dong, W., Shi, Y., Xia, Z., Lei, Y., & Guo, F. (2008). Effects of trace amounts of rare earth additions on microstructure and properties of Sn-Bi-based solder alloy. Journal of Electronic Materials, 37(7), 982-991.

[31] Myung, W. R., Ko, M. K., Kim, Y., & Jung, S. B. (2015). Effects of Ag content on the reliability of LED package component with Sn–Bi–Ag solder. Journal of Materials Science: Materials in Electronics, 26(11), 8707-8713.

[32] Guan, Z. M., Liu, G. X., & Liu, T. (2000). Kinetics of interface reaction in 40Sn-Bi/Cu and 40Sn-Bi-2Ag/Cu systems during aging in solid state. IEEE transactions on advanced packaging, 23(4), 737-742.

[33] Suganuma, K., Sakai, T., Kim, K. S., Takagi, Y., Sugimoto, J., &Ueshima, M. (2002). Thermal and mechanical stability of soldering QFP with Sn-Bi-Ag lead-free alloy. IEEE Transactions on electronics packaging manufacturing, 25(4), 257-261.

[34] Lai, Z., & Ye, D. (2016). Microstructure and Properties of Sn-10Bi-xCu Solder Alloy/Joint. Journal of Electronic Materials, 45(7), 3702-3711.

[35] Zhang, C., Liu, S. D., Qian, G. T., Jian, Z. H. O. U., & Feng, X. U. E. (2014). Effect of Sb content on properties of Sn—Bi solders. Transactions of Nonferrous Metals Society of China, 24(1), 184-191.

[36] Mokhtari, O., & Nishikawa, H. (2016). Correlation between microstructure and mechanical properties of Sn–Bi–X solders. Materials Science and Engineering: A, 651, 831-839.

[37] Mokhtari, O., & Nishikawa, H. (2014). Effects of In and Ni addition on microstructure of Sn-58Bi solder joint. Journal of electronic materials, 43(11), 4158-4170.

[38] Chen, X., Xue, F., Zhou, J., & Yao, Y. (2015). Effect of In on microstructure, thermodynamic characteristic and mechanical properties of Sn–Bi based lead-free solder. Journal of Alloys and Compounds, 633, 377-383.

[39] Li, Q., Ma, N., Lei, Y., Lin, J., Fu, H., & Gu, J. (2016). Characterization of low-melting-point Sn-Bi-In lead-free solders. Journal of Electronic Materials, 45(11), 5800-5810.

[40] Huang, Y. C., & Chen, S. W. (2011). Effects of Co alloying and size on solidification and interfacial reactions in Sn-57 wt.% Bi-(Co)/Cu couples. Journal of electronic materials, 40(1), 62-70.

[41] Zhou, S., Mokhtari, O., Rafique, M. G., Shunmugasamy, V. C., Mansoor, B., & Nishikawa, H. (2018). Improvement in the mechanical properties of eutectic Sn-58Bi alloy by 0.5 and 1 wt% Zn addition before and after thermal aging. Journal of Alloys and Compounds, 765, 1243-1252.

[42] Mokhtari, O., Zhou, S., YC, C., & Nishikawa, H. (2016). Effect of Zn addition on interfacial reactions between Sn-Bi solder and Cu substrate. Materials Transactions, 57(8), 1272-1276.

[43] Wang, F., Chen, H., Huang, Y., Liu, L., & Zhang, Z. (2019). Recent progress on the development of Sn–Bi based low-temperature Pb-free solders. Journal of Materials Science: Materials in Electronics, 30(4), 3222-3243.

[44] Dale, T., Singh, Y., Bernander, I., Subbarayan, G., Handwerker, C., Su, P., & Glasauer, B. (2020). Fatigue Life of Sn3. 0Ag0. 5Cu Solder Alloy Under Combined Cyclic Shear and Constant Tensile/Compressive Loads. Journal of Electronic Packaging, 142(4).

[45] Bhate, D., Chan, D., Subbarayan, G., Chiu, T. C., Gupta, V., & Edwards, D. R. (2008). Constitutive behavior of Sn3. 8Ag0. 7Cu and Sn1. 0Ag0. 5Cu alloys at creep and low strain rate regimes. IEEE Transactions on Components and Packaging Technologies, 31(3), 622-633.

[46] Schmetterer, C., Vizdal, J., Kroupa, A., Kodentsov, A., & Ipser, H. (2009). The ni-rich part of the ni-P-Sn system: Isothermal sections. Journal of electronic materials, 38(11), 2275-2300.

[47] Boettinger, W. J., Vaudin, M. D., Williams, M. E., Bendersky, L. A., & Wagner, W. R. (2003). Electron backscattered diffraction and energy dispersive X-ray spectroscopy study of the phase NiSn 4. Journal of electronic materials, 32(6), 511-515.

[48] Belyakov, S. A., & Gourlay, C. M. (2016). The Influence of Cu on Metastable NiSn 4 in Sn-3.5 Ag-xCu/ENIG Joints. Journal of Electronic Materials, 45(1), 12-20.

2.8 Appendix

Thermodynamic Calculation of Stable Phases in Sn-Bi Solder Joint Systems

A series of isothermal sections were generated for different ternaries within the Au-Bi-Cu-Ni-Sn using Thermo-Calc with the TCSLD3 solder database and are included here for reference. For Sn-58Bi on OSP-Cu surface finishes, intermetallic compound growth in Sn-Bi homogeneous joints uses Sn-Bi-Cu isothermal sections for reactions during reflow and isothermal annealing (Figure 2.20).

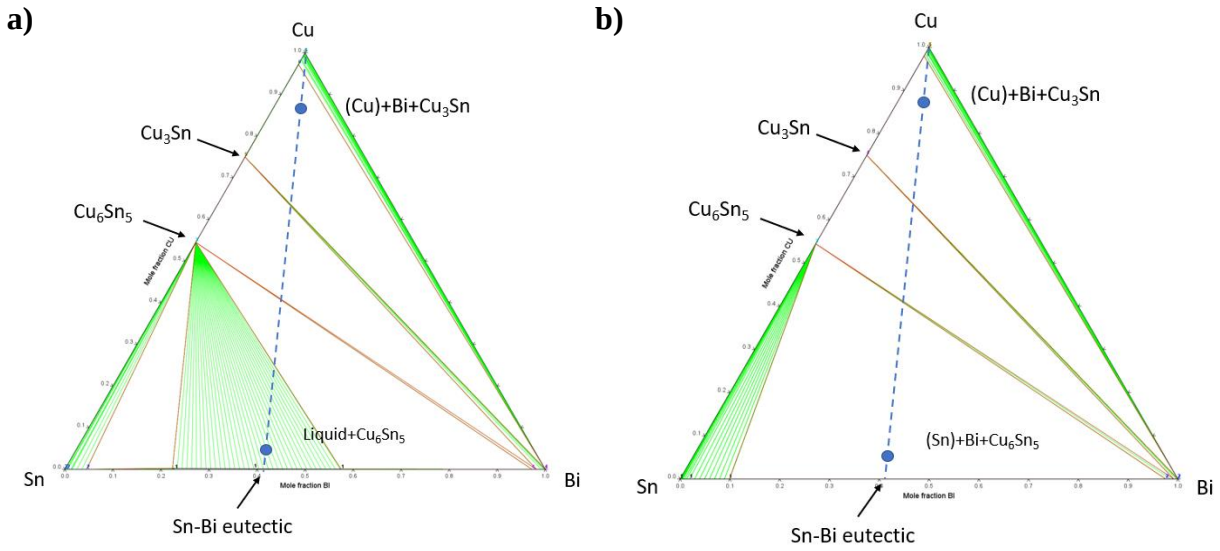

Figure 2.20. Isothermal sections of Sn-Bi-Cu ternary system during a) reflow (180°C), and b) solid-state annealing (125°C) showing possible intermetallic phases formation during either process

For Sn-Bi-based low temperature solders with ENIG metallization, the influence of Ni and Au on ENIG should be taken into further consideration. First, the isothermal sections of Sn-Bi-Ni ternary system were generated, as shown in Figure 2.21.

Since ENIG metallization also contains a small amount of Au, the influence of Au on intermetallic compound formation must also be taken into account. The isothermal sections of Sn-Ni-Au ternary systems during reflow and solid-state annealing are shown in Figure 2.22.

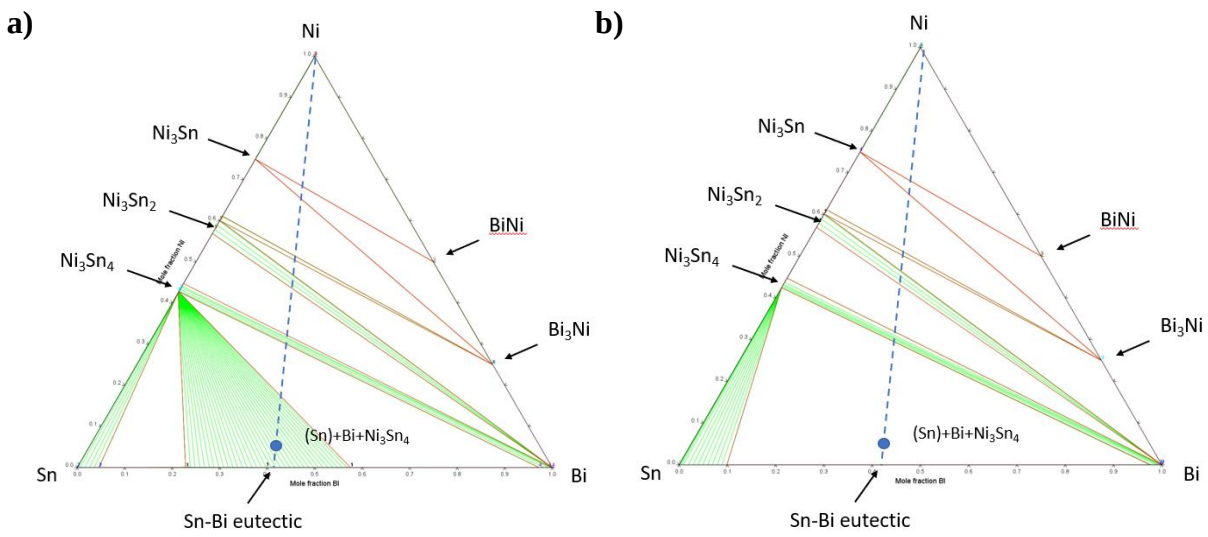

Figure 2.21. Isothermal sections of Sn-Bi-Ni ternary system during a) reflow (180°C), and b) solid-state annealing (125°C) showing possible intermetallic phases formation during either process

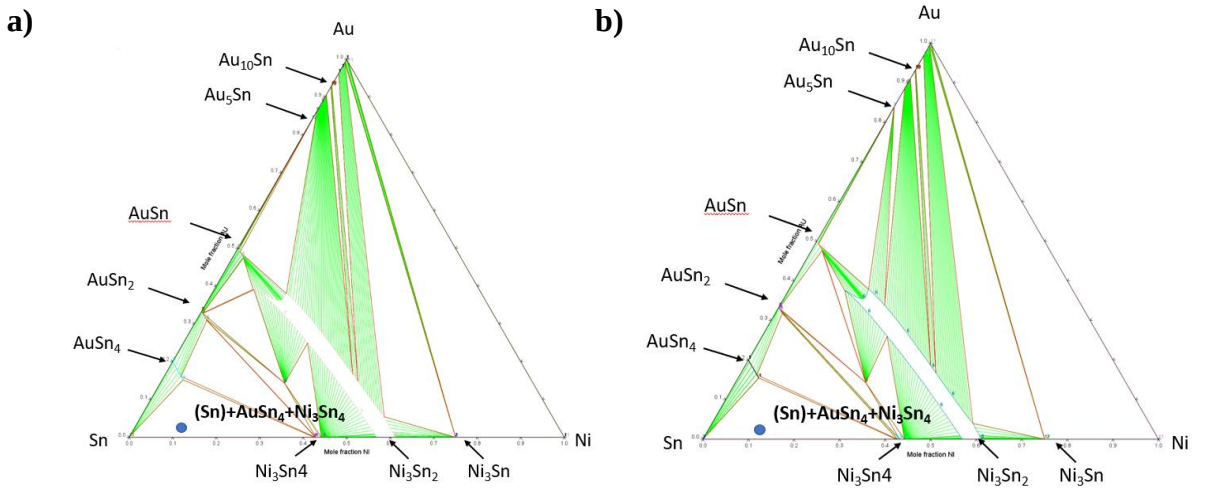

Figure 2.22. Isothermal sections of Sn-Ni-Au ternary system during a) reflow (180°C), and b) solid-state annealing (125°C) showing possible intermetallic phases formation during either process

In SnBi-based solders on OSP-Cu finish, Cu_6Sn_5 and Cu_3Sn are expected to form and grow during reflow and solid-state annealing process; Ni_3Sn_4 and $AuSn_4$ formation and growth are expected during reflow and solid-state annealing in SnBi-based solders on ENIG metallization, however, the phase diagrams do not show the large Ni:Au ratios observed in experiments.

3. MICROALLOYING EFFECTS ON INTERMETALLIC COMPOUND GROWTH AND MECHANICAL RELIABILITY OF TIN-BISMUTH SOLDER JOINTS

3.1 Abstract

A new low temperature interconnect technology based on Sn-Bi alloys is being considered as a substitute for Sn-Ag-Cu (SAC) solder BGAs to form joints with significantly lower melting temperatures than homogeneous SAC joints. Microstructure development studies of reflow and aging, especially intermetallic growth, are important in understanding mechanical reliability and failure paths in the resulting homogeneous joints. This study focused on intermetallic growth between several SnBi eutectic and off-eutectic alloys with different microalloying elements (Sb, Cu, In) soldered on electroless nickel immersion gold (ENIG) metallization and organic surface protection (OSP) surface finishes. Experimental results revealed that, during solid state annealing following reflow, the (50nm) Au from the ENIG finish catalyzed rapid $(Au,Ni)Sn_4$ intermetallic growth at the Ni-solder interface in both Sn-Bi and Sn-Bi-Ag homogeneous joints, which led to significant solder joint embrittlement during creep and fatigue loading. Further study found that the growth rate of $(Au,Ni)Sn_4$ intermetallic could be reduced by In and Sb alloying of SnBi solders and is totally eliminated with Cu addition. Fatigue testing revealed Au embrittlement is always present in solder joints without Cu, even with In and Sb additions due to $(Au,Ni)Sn_4$ formation. The fatigue reliability of Cu-containing alloys is better on ENIG due to the formation of $(Ni, Cu, Au)_6Sn_5$ at the solder-surface finish interface instead of $(Au,Ni)Sn_4$.

Keywords: Tin-bismuth solder, electroless nickel immersion gold, gold embrittlement, intermetallic growth

3.2 Introduction

As integrated circuits have become larger and thinner, chip warpage during reflow has become an increasing issue, with warpage increasing with increasing reflow temperature. Tin-silver-copper (SAC) alloys, the industry standard, require peak reflow temperatures of approximately 240°C due to their high eutectic temperature (217°C). Such high reflow temperatures have been observed to cause serious warpage-induced defects, such as separation of SAC solder balls from SAC solder

paste before melting (217°C) to form head-on-pillow (HoP) defects along the edges of the IC and bridging in the center [1, 2]. A schematic illustration of chip warpage and resulting defects is shown in Figure 3.1. In HoP, the connections between solder on the board side and the ball are weak, based on Van der Waals forces. Therefore, when the component encounters large thermal or mechanical stresses during use, HoP defects can cause electrical failure in the component [3]. Solder joints in the center of the packaging may also form bridging defects, which could cause short circuit and component failure.

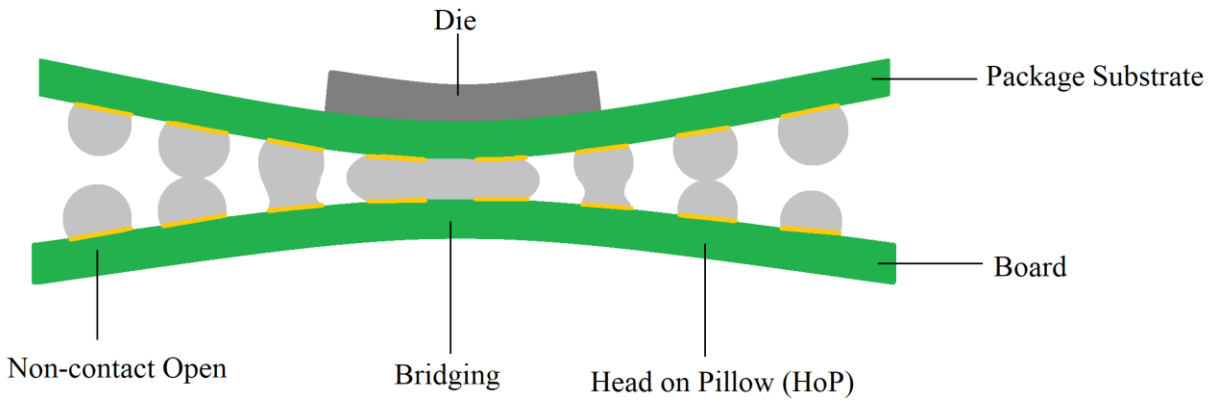

Figure 3.1. Schematic illustration of component warpage and different defects formed during reflow soldering

As a result, low temperature soldering (LTS) systems have been recommended as a solution to reduce heating-induced warpage [4-11]. Solders based on eutectic Sn-Bi solders have been used widely in low temperature soldering due to their low eutectic temperature [12], as well as low cost and toxicity. To lower the reflow temperature with the assistance of Sn-Bi-based alloys, two different kinds of geometries have been proposed. Solders based on Sn-Bi eutectic could be used instead of SAC solder paste to assemble components with SAC solder balls to form "hybrid" joints after soldering, as shown in Figure 3.2 below. Another way of achieving low temperature soldering is to replace both the ball and the paste with Sn-Bi-based alloys to form homogeneous joints after reflow, as shown in Figure 3.3. For both geometries, only melting of Sn-Bi-based alloys with their lower liquidus temperatures is required. For the Sn-Bi eutectic temperature of 139°C, a reflow temperature of approximately 160-190°C is required, lowering the peak reflow temperature by 50-80°C.

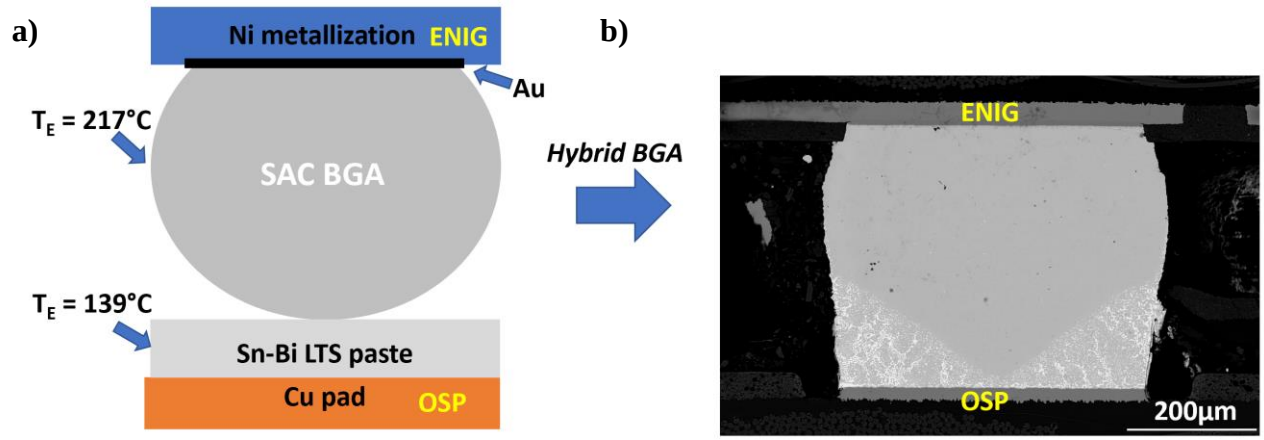

Figure 3.2. a) A schematic illustration of hybrid joints before reflow, when Sn-Bi LTS pastes substitutes SAC solder paste during surface mount procedure; b) typical microstructure of a LTS-SAC hybrid joint after reflow showing the Bi diffusion region and the un-melted SAC region

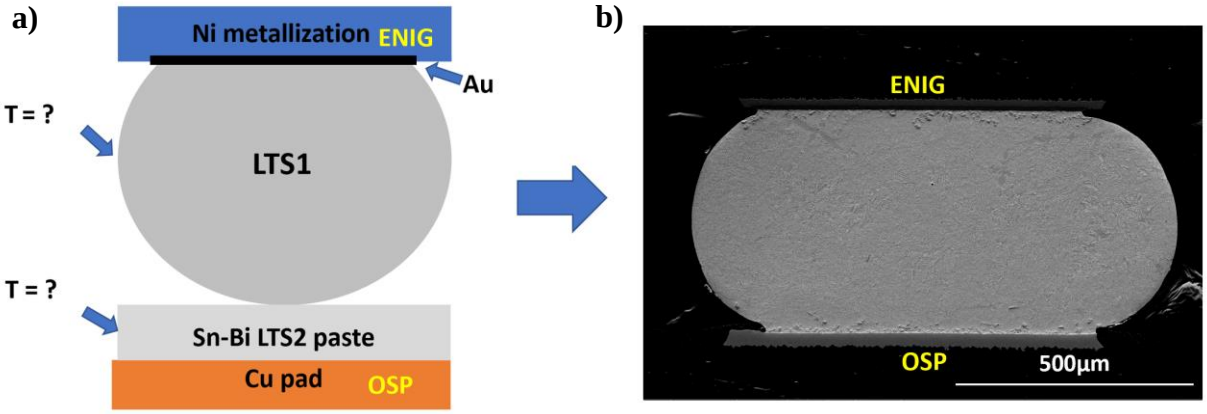

Figure 3.3. a) A schematic illustration of Sn-Bi homogeneous joints before reflow, when Sn-Bi LTS pastes substitutes both SAC solder paste and SAC BGA during surface mount procedure; b) microstructure of a Sn57Bi1Ag homogeneous joint after reflow

To understand the reliability of low temperature soldering systems, both hybrid and homogeneous, one of the most important areas to be examined is intermetallic compound stability and growth with different surface finishes because of the introduction of Bi into the system. There has been previous research on intermetallic compound growth with Sn-Bi alloys on different surface finishes, such as Sn-Bi and Sn-Bi-Ag solders on Cu [13-17], ENIG [13,16,18-20], Ni substrates [14,15,20-23], and ENEPIG [13,16,18,24]. Li et al. annealed Sn-Bi solders on Cu [25], Ni [26,27], and ENIG [26,27] at 240°C, 100°C above the Sn-Bi eutectic temperature. For Sn-Bi

solders on Cu, intermetallic compounds Cu_6Sn_5 and Cu_3Sn formed at the solder-surface finish interface during 240°C annealing with two different growth rates observed depending on annealing time reflecting a change in mechanism of intermetallic growth [25]. For Sn-Bi solders on Ni substrates, Ni_3Sn_4 forms along the interface during annealing at 240°C [26,27], while Sn-Bi solders in contact with ENIG surface finish result in the formation of Ni_3Sn_4 and Ni_3P intermetallic compounds at the solder-surface finish interface during annealing at 240°C [26,27]. However, most of the previous research mainly focused on the intermetallic compound growth at either very high temperature (above the Sn-Bi eutectic temperature) or low application temperatures (room temperature, 85°C, 100°C). There has been little research focused on intermetallic compound growth under harsh, solid-state aging environments (homologous temperatures > 0.75), or supported by thermodynamic simulation, measurements of the order of intermetallic growth with isothermal annealing, or growth rate of intermetallic compound layer in Sn-Bi solders on different surface finishes.

For micro-alloying effects in Sn-Bi solders, previous research has studied the influence on solder microstructure and intermetallic compound growth for different elemental additions into Sn-Bi solders. The addition of Ag into Sn-Bi solders produces Ag_3Sn intermetallic precipitates in the solder matrix, refines the microstructure, and slows down Cu_6Sn_5 growth at the solder-Cu interface during aging [28-31]. Additions of Cu to Sn-Bi alloys results in the formation of Cu_6Sn_5 particles in the solder matrix and also refines the microstructure [32]. Zhang et al. [33] and Sukuyama et al. [42] found Sb addition into SnBi solder produced SnSb intermediate phases, which serves as a refining agent. Chen et al. [36] and Li et al.[37] reported that with In addition into Sn–Bi solder, In alloying produces Bi–In IMCs in the solder matrix as a refining agent, The addition of 0.5 wt% In could also suppress the IMC growth on Cu during thermal aging. Li et al. studied the effects of Al, Cr, Cu, Si, Zn, Ag, Au, Pt and Nb micro-alloying additions on intermetallic compound growth rates at the solder-Cu interface[25].Their results revealed that additions Al, Cr, Cu, Si, Au, Pt and Nb have no effect on intermetallic layer growth, Ag additions slow down Cu_6Sn_5 layer growth during aging at 240°C, and Zn additions slow down intermetallic layer growth by forming Cu_5Zn_8 phase rather than Cu_6Sn_5 and Cu_3Sn [25]. Research on alloying Sn-Bi solders with Sb [33,42], Ni [34,35], In [36,37], Co [38], and Zn [39,40], has also been reported for assembly with Cu surface finishes. Wang et al. [41] published a review of the literature in 2019 which provides some details of earlier work.

For homogeneous LTS joints, intermetallic compound growth on the component side (ENIG and ENIPEG) is also important for joint reliability. Li et al. studied intermetallic compound growth during high temperature annealing at 240°C for Sn-Bi alloys on Ni and ENIG surface finishes with Al, Cr, Si, Zn, Ag, Au, Ru, Ti, Pt, Nb, and Cu additions [26,27]. Among all the micro-alloying elements, only Cu is effective on slowing down intermetallic layer growth by forming $(Ni,Cu)_6Sn_5$ rather than Ni_3Sn_4 and Ni_3P phases during aging at 240°C [26,27]. However, this research only focused on intermetallic growth on ENIG at very high temperatures (above reflow peak temperature), information about intermetallic compound growth at typical LTS reflow durations and temperatures (180°C) and during solid-state annealing (125°C) were missing, as were the resulting mechanical properties of the solder joints.

For the mechanical properties of the SnBi alloys with elemental additions, Zhang et al. [33] found with Sb additions, the shear strength of solder interconnect decreases during ball shear testing. Shen et al. [43] found out that the tensile strength and elongation of the solder increased due to Cu additions. Cu additions also increase the creep resistance [44] and shear strength [45] of the solder joints. Chen et al.'s [36] work revealed that with In additions, the tensile strength of SnBi solder decreased slightly, but there is a significant increase in the elongation of the solder. Shalaby et al. [46] found In additions also increase the creep resistance, and Mokhtari et al. [47] discovered the increase in shear strength in In-added solder joints. For all the previous study, they focused on mainly the characterization of tensile properties of the alloy itself instead of solder interconnects. For all the mechanical testing on solder interconnects, mainly creep and ball shear testing were conducted, which lacks systematic study on the reliability of the joints, such as monotonic and fatigue loading tests.

To fill this gap, the main focus for the research reported here is to characterize intermetallic compound growth under these conditions for Sn-Bi solders with Sb, Cu and In additions on Cu-OSP and ENIG surface finishes and relate the resulting microstructures to mechanical behavior and reliability. Starting from phase equilibrium calculations for Sn-Bi-Cu, Sn-Bi-Sb, and Sn-Bi-In ternary systems, intermetallic formation in the bulk solder and at the solder-surface finish interfaces is examined, comparing microstructures and phases after reflow with those after high temperature, solid annealing (85°C and 125°C). Mechanical reliability characterization of these joints after reflow and aging were followed to study the influence of different microalloying elements on the intermetallic compound growth as well as the failure modes in the solder joints.

3.3 Experimental

The test specimens consist of eight solder joints connecting two FR4 boards from Bay Area Circuits. Figure 3.4 a) shows the configuration and dimensions of the test specimens. The FR4 substrates are single layer PCBs with mask-defined copper pads and electroless nickel-immersion gold surface finish (ENIG) or Cu coated with an organic surface preservative (OSP) surface finish. The 730 μm diameter pads are arranged in a 7 x 7, 1:27mm pitch grid. The solder joints were assembled by reflowing 500 μm diameter Sn58BiSbNi (L29) or Sn40BiCuNi (L27) (Senju Metal Industry Co., Ltd.) or Sn56.5Bi0.5In solder balls (Scientific Alloys). The samples were assembled by DDM Novastar GF-12HC-HT 3-zone reflow oven. For both alloys, a maximum temperature of 180°C was used with 90 seconds of time above liquidus (139°C). After reflow, the standoff height was measured after cross-section under Quanta 650 FEG SEM for each sample prior to testing. The measured standoff heights ranged between 145 and 165μm. After assembly, the test specimens were stored at -10°C to slow any microstructural aging. To study the microstructure evolution during solid state annealing, the test specimens were annealed at 125°C for up to 250 hours in Fisher Scientific 725F annealing furnace. After solid state annealing and mechanical reliability tests, metallographic cross-sections were prepared using standard techniques, i. e. mounting in epoxy and polishing using a progression of diamond suspensions on porous polyurethane polishing pads (Allied High Tech). Quanta 650 FEG SEM was used to observe the microstructure evolution and fracture path propagation in all the samples. Measurements of the thickness of intermetallic compound (IMC) layers were performed using ImageJ. Thickness was measured by doing length-average (t=A/l) of IMC layers on multiple SEM images due to the nonuniformity of IMC layers. EDS was utilized to identify different intermetallic compound species as well as elemental segregations in the solder interconnects.

As a starting point in estimating the possible intermetallic compounds and their compositions forming in solder joints during reflow and solid-state annealing, Thermo-Calc 2020a software was utilized to calculate the isothermal sections and solidification paths of Sn-Bi-Cu, Sn-Bi-Sb, and Sn-Bi-In ternary systems using TCSLD3 solder alloys database.

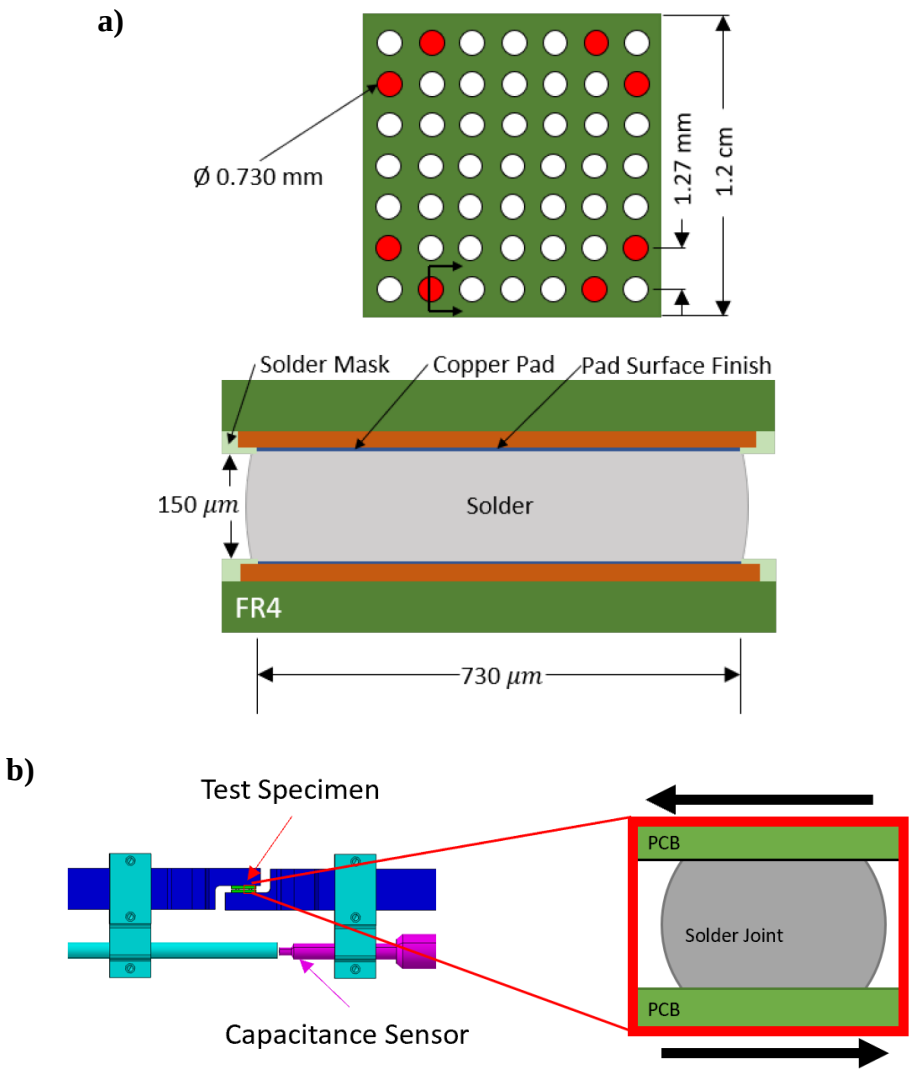

Figure 3.4. Schematic illustration of SnBi low temperature solder test specimens. The eight red circles indicate the locations of the solder joints in the top view of the printed circuit board (top). The cross section of an assembled single solder joint (bottom)

Displacement-controlled shear fatigue tests were performed on the test specimens until failure using a custom-built micro-precision mechanical tester, as shown as the schematic illustration in Figure 3.4 b). The test specimen displacement for the tester is measured with a capacitance sensor mounted near the test specimen. The capacitance sensor has a resolution of 7 nm. The capacitance sensor displacement measurement is used for closed-loop control of the tester to ensure that the desired displacement and displacement rate is imposed on the test specimen. This feature is critical

for solder characterization due to most solder alloys' viscoplastic behavior at room temperature, i.e., the stress response of solder alloys depend on the applied strain rate. Shear fatigue tests were performed at 30°C. The displacement profile consists of a 0.20 μm/s ramp up (7.7×10^{-4} s^{-1} strain rate) to 39 μm (15% strain) followed by a 200 s dwell, a 0.20 μm/s ramp down (7.7×10^{-4} s^{-1} strain rate) to 0 μm (0% strain), and another 200 s dwell. The displacement profile is inspired by the on/off cycle experienced by some electronics. The displacement profile is repeated until the test specimen has failed or after the test has run for 24 hours. The first ramp up is identical to a monotonic test at $7.7 \times 10\text{-}^{4}$ s^{-1}. The equivalent stress, σ, and equivalent strain, ε, for the test specimens are estimated with:

$$\sigma=(\sqrt{3}\ F)/A$$

$$\varepsilon=\delta/(\sqrt{3}\ h)$$

where F is the measured shear load, A is the total pad area, δ is the shear displacement, and h is the standoff height.

3.4 Results and Discussion

3.4.1 Thermodynamic Calculations of Intermetallic Compound Growth during Reflow/Solidification and Solid-state Annealing

Phase equilibrium calculations give insights into the expected phases within the bulk solder and at the solder-surface finish interfaces during reflow (melting at 180˚C and solidification to room temperature) and subsequent annealing at 125˚C. In the following analysis, isothermal sections are calculated and single point ThermoCalc calculations are performed using the bulk solder compositions to identify the phases formed during melting and after solidification. Phase formation at the interfaces is characterized by starting with the bulk compositions and identifying what additional phases and their compositions are expected when the solders come in contact with ENIG and OSP and dissolve Au+Ni and Cu, respectively. The solder joints form from solders of the initial alloy compositions (Sn58BiSbNi (L29), Sn40BiCuNi (L27) and Sn56.5Bi0.5In) in contact with ENIG (50nm Au/4um Ni, thick Cu) or Cu (OSP) so there are different conditions in the bulk solder and at the solder-surface finish interfaces that can be examined using the assumptions of local equilibrium.

Intermetallic Compounds in SnBiSb, SnBiCu and SnBiIn

With different microalloying elements into SnBi solders, different intermetallic compounds are expected to form during either reflow or solidification process. After inputting the compositions of Sn58BiSbNi (L29), Sn40BiCuNi (L27) and Sn56.5Bi0.5In alloys into ThermoCalc at different temperatures, SnBi with Sb additions introduces SnSb intermetallic compounds during cooling process after reflow, but no SnSb is formed during reflow, where Sb is distributed in the liquid phase. In solid phase, Sb either distributes in Sn solid solution, or forms SnSb with Sn. Cu additions into SnBi solders generates Cu_6Sn_5 particles during reflow and solidification process. 0.5wt% of In addition into SnBi solders on the other hand, does not generate any In-based intermetallic compounds in the solder during reflow or cooling process, and In distributes in Sn at solid state.

SnBiSb, SnBiCu and SnBiIn on Cu-OSP

Reflow of all the three SnBi solders in contact with OSP Cu at 180˚C leads to the formation of liquid solder with Cu dissolved into the liquid up to a 0.03 wt.% maximum solubility of Cu. The phase at the liquid solder-Cu interface is expected to be Cu_6Sn_5, with Cu_3Sn forming between Cu_6Sn_5 and Cu. During solidification, (Sn), (Bi), and Cu_6Sn_5 are expected to form in Sn40BiCuNi and Sn56.5BiIn on OSP; for Sn58BiSbNi, the phases are (Sn), (Bi), Cu_6Sn_5, and SnSb, with SnSb nucleation and formation on solidification. With annealing at 85°C and 125 ˚C, there are no additional phases found.

SnBiSb, SnBiCu and SnBiIn on ENIG

During reflow of Sn58BiSbNi, Sn40BiCuNi and Sn56.5Bi0.5In on ENIG at 180˚C, Au and Ni from the ENIG surface finish dissolve into the liquid solder. With the measured 50nm Au thicknesses from two ENIG surface finished pads and the solder volumes in this study, the liquid solder contains 0.14wt% of Au. The solubility limit of Ni in Sn58BiSbNi, Sn40BiCuNi and Sn56.5Bi0.5In is estimated to be 0.01wt% Ni. At the interface between liquid Sn58BiSbNi, Sn56.5Bi0.5In solders and the electroless Ni(P) layer, Ni_3Sn_4 is expected to form at the interface with liquid solder and a Ni_3P layer forming between Ni_3Sn_4 and the electroless Ni(P) layer due to the low solubility of P in Ni_3Sn_4. For liquid Sn40BiCuNi solder, with Cu additions, $(Cu,Ni)_6Sn_5$ is expected to form at the interface with liquid solder. During solidification of Sn56.5Bi0.5In on

ENIG, (Sn), (Bi), and $(Au,Ni)Sn_4$ form in the bulk solder, with the Ni in solution in $(Au,Ni)Sn_4$ leading to a Ni:Au ratio (mole basis) of 1:4. For solidification of Sn58BiSbNi on ENIG, (Sn), (Bi), $(Au,Ni)Sn_4$, SnSb and NiSb are expected in the bulk. For solidification of Sn40BiCuNi on ENIG, (Sn), (Bi), $(Au,Ni)Sn_4$, and $(Cu,Ni)_6Sn_5$ are expected in the bulk. For annealing at 85°C and 125 ˚C, the expected phases in the bulk at equilibrium are (Sn), (Bi), $(Au,Ni)Sn_4$ for Sn56.5Bi0.5In; (Sn), (Bi), SnSb, NiSb, and $(Au,Ni)Sn_4$ for Sn58BiSbNi and (Sn), (Bi), $(Au,Ni)Sn_4$, and $(Cu,Ni)_6Sn_5$ for Sn40BiCuNi. For the reaction at the interface between the bulk solder and Ni_3Sn_4, it is expected that $(Au,Ni)Sn_4$ in the bulk dissolves and reprecipitates at the interface where additional Ni is provided by diffusion from Ni_3Sn_4. It is expected that $(Au,Ni)Sn_4$ will continue to grow at the interface until it reaches the maximum Ni:Au ratio of approximately 0.6:1. For the solder joints used here and a Au concentration in the solder of 0.14wt%, the maximum thickness of $(Au,Ni)Sn_4$ at the interfaces with Ni(P) would be 1μm.

3.4.2 Microstructure Coarsening of SnBiSb, SnBiCu and SnBiIn during Aging

The microstructures of Sn58Bi, Sn58BiSbSn, Sn40BiCuNi and Sn56.5Bi0.5In after reflow and solid-state annealing process are shown in Figure 3.5. Coarsening of SnBi eutectic structures were observed in all of the alloys after aging. Comparing the aged microstructure, Sb additions and Cu additions showed a clear refinement of SnBi eutectic structure during aging process. This refinement effect might be caused by the intermetallic compounds inside bulk solder. Fine Cu_6Sn_5 particles were observed in bulk Sn40BiCuNi solder due to Cu additions, although no SnSb particles were observed in Sn58BiSbNi, Sakuyama et al. [42] utilized EPMA to confirm the existence of SnSb particles in SnBi alloys with Sb additions, which also refines the microstructure. For Sn56.5BiIn alloys, no intermetallic compounds were found in bulk solder under SEM, and Chen et al. [36] proved that In-based intermetallic compounds will be present only with In additions over 3wt%. Therefore, with no intermetallic compounds in Sn56.5Bi0.5In alloys, no significant refinement of SnBi eutectic structure was observed. EDS analysis revealed with Sb and In additions, Sb and In distributes in Sn instead of Bi, as shown in Figure 3.6 below.

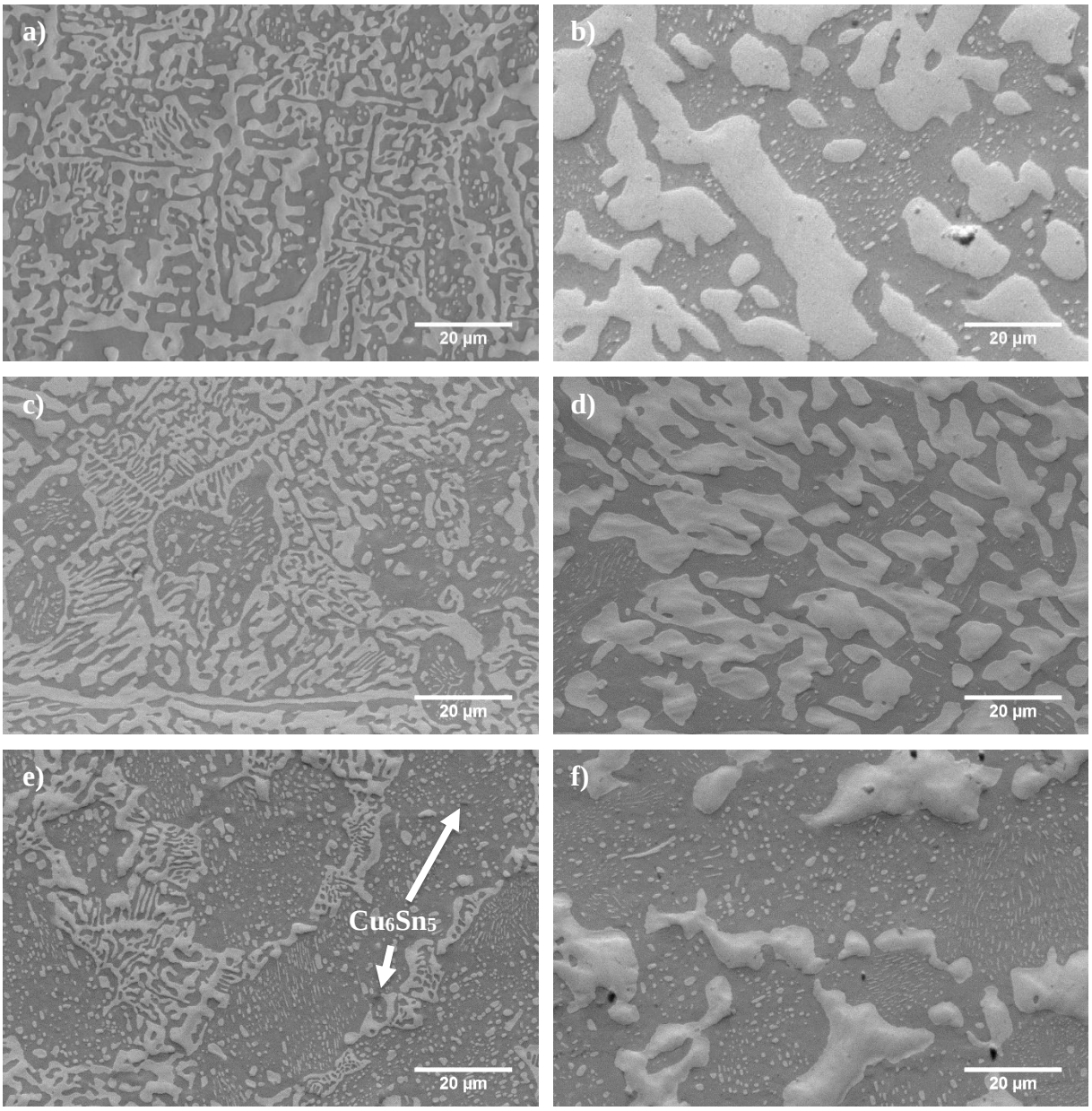

Figure 3.5. Microstructure of a) Sn58Bi after reflow; b) Sn58Bi after 250 hours of aging at 125°C; c) Sn58BiSbNi after reflow; d) Sn58BiSbNi after 250 hours of aging at 125°C; e) Sn40BiCuNi after reflow; f) Sn40BiCuNi after 250 hours of aging at 125°C; g) Sn56.5Bi0.5In after reflow; and h) Sn56.5Bi0.5In after 250 hours of aging at 125°C

Figure 3.5 continued

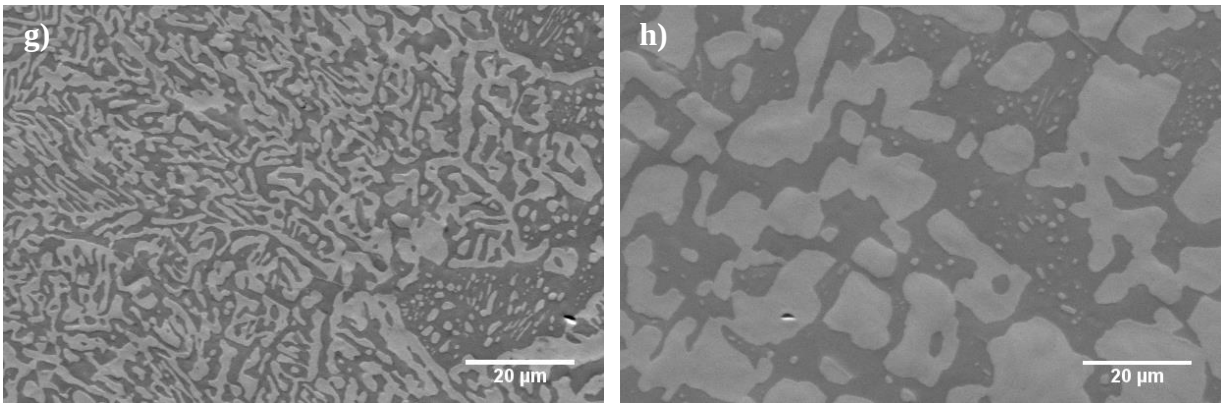

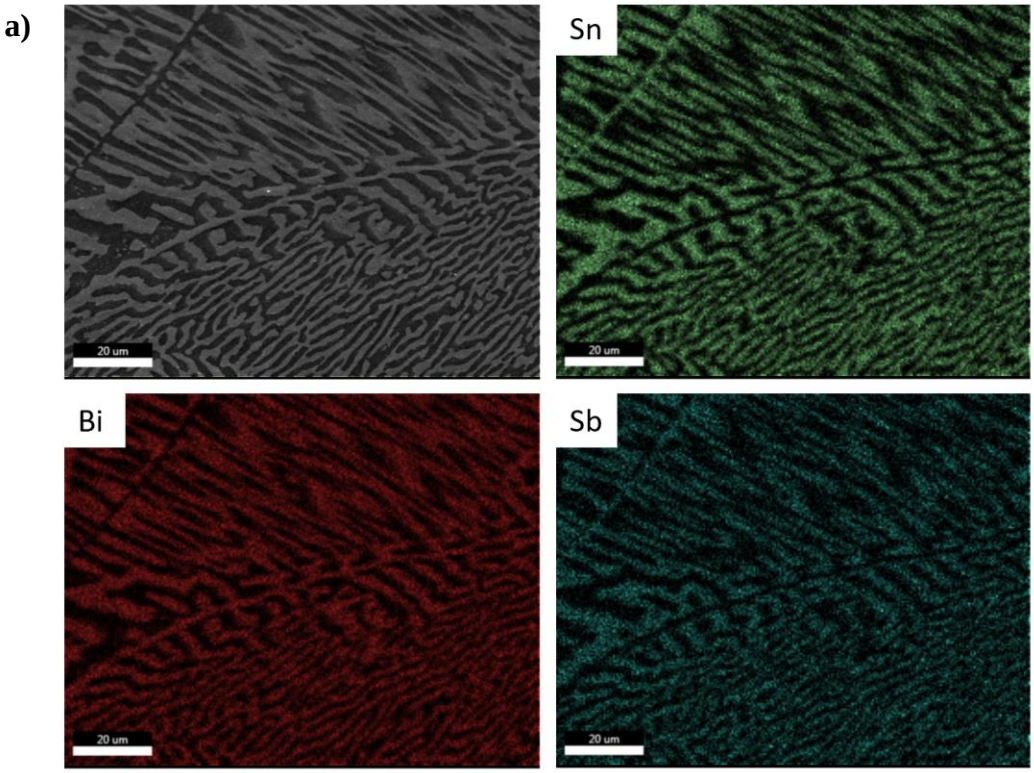

Figure 3.6. EDS mapping of a) Sn58BiSbNi after reflow and b) Sn56.5Bi0.5In after reflow showing Sb and In distribution in Sn

Figure 3.6 continued

b)

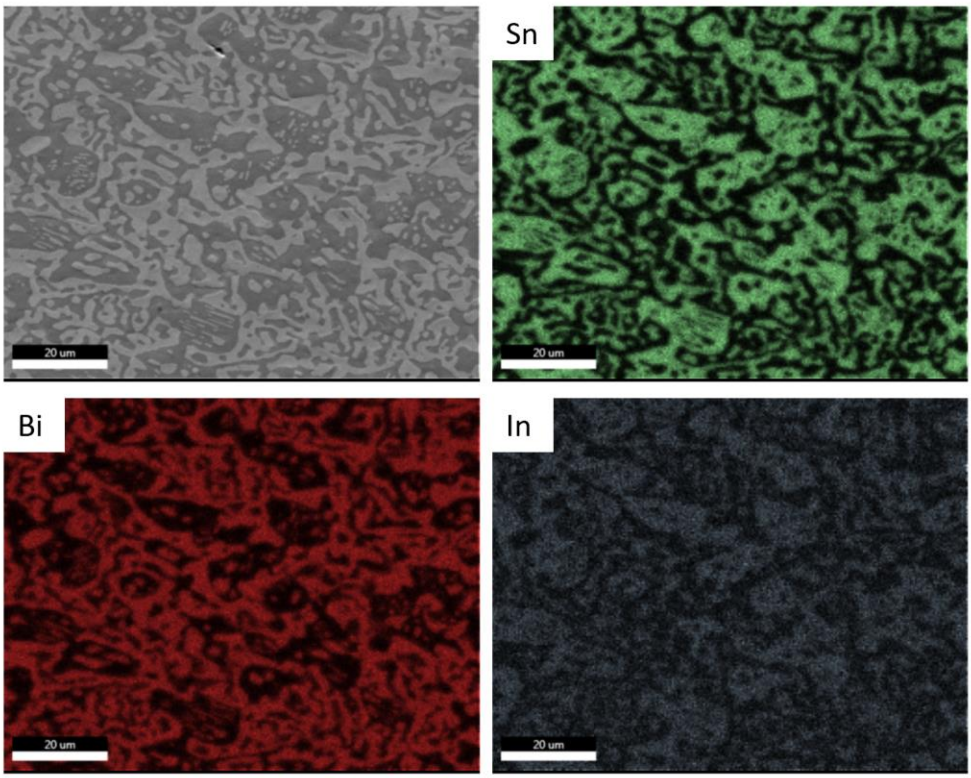

3.4.3 Intermetallic Compound Growth of SnBiSb, SnBiCu and SnBiIn on Cu-OSP

The phases observed on OSP are those predicted by ThermoCalc. Typical microstructures of Sn58BiSbNi and Sn56.5Bi0.5In solders on OSP surface finish after reflow/solid-state and solid annealing at 125˚C are shown in Figure 3.7. After reflow, the solder showed good wetting with the OSP metallization, and a facetted polycrystalline layer of Cu_6Sn_5 formed at the solder-Cu interface. Thermodynamic calculations estimated that Cu dissolution into the liquid was possible up to a 0.03 wt.% maximum solubility of Cu, however no Cu_6Sn_5 was observed in the bulk after solidification. For Sn40BiCuNi, similar morphology of Cu_6Sn_5 was found at solder-Cu interface, with smaller Cu_6Sn_5 particles inside bulk solder due to Cu additions. During solid-state annealing, Cu_3Sn and Cu_6Sn_5 layer growth along the interface and Bi coarsening within the eutectic were observed in the joints. Similar Cu_6Sn_5 morphologies were seen in OSP-Sn40BiCuNi-OSP and OSP-Sn56.50.5In-OSP joints (Figure 3.7). However, ThermoCalc predicted the existence of SnSb intermetallic compound in Sn58BiSbNi, no SnSb is found in cross-section. The intermetallic growth rates are shown in Figure 3.8. Sn58Bi showed higher intermetallic compound growth rate

than the other three solders on OSP at 125°C. The intermetallic growth rates at 85°C, however, do not have an obvious difference between the four alloys. Since no intermetallic compounds were found in Sn58BiSbNi and Sn56.5BiIn alloys, intermetallic compounds may not be the reason for intermetallic growth suppression during annealing, the reason for Sb and In additions on slowing down Cu_6Sn_5 layer on OSP surface finish at 125°C should be further studied.

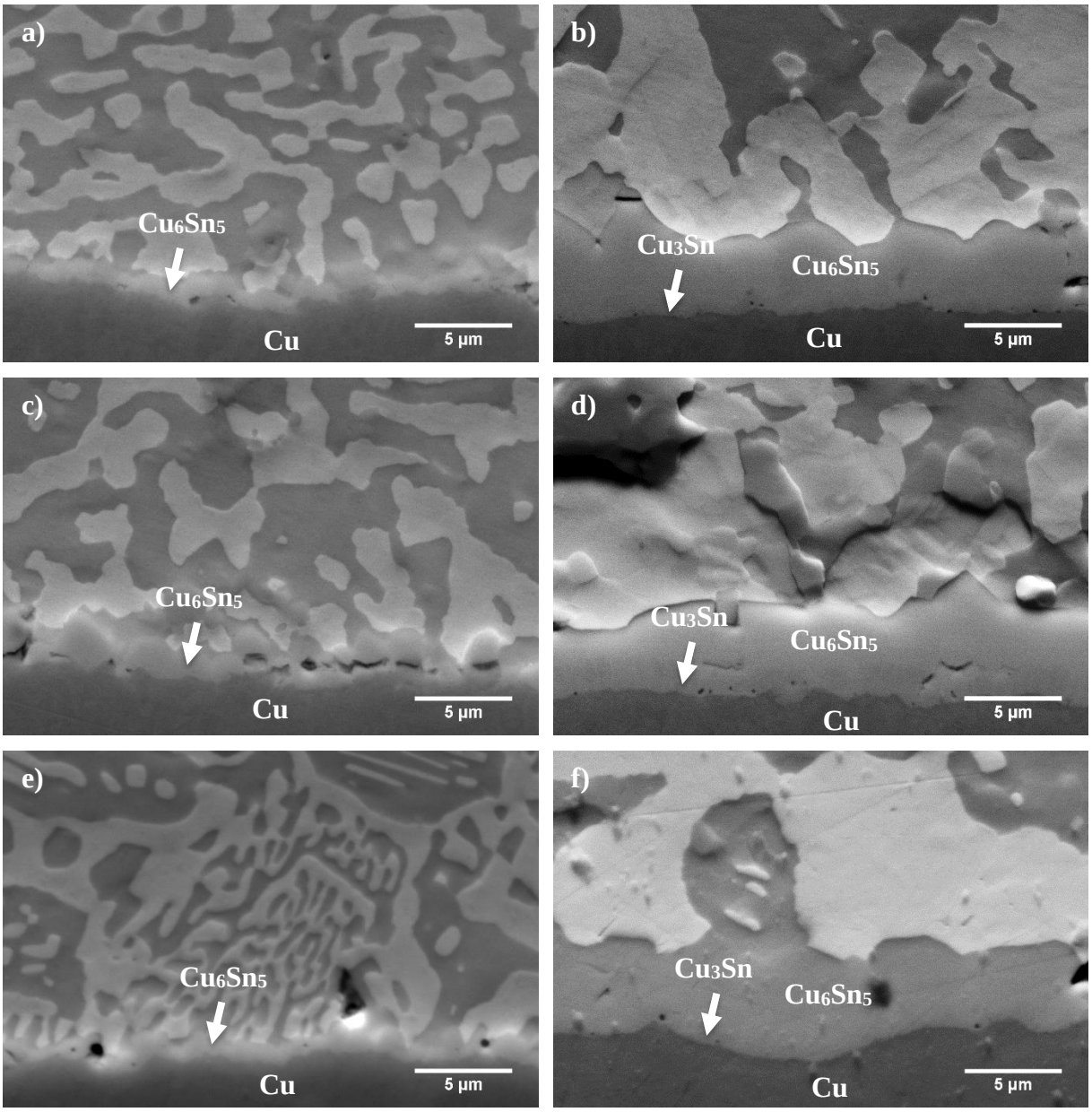

Figure 3.7. Microstructure of solder-Cu interface of intermetallic layers of OSP-Sn58BiSbNi-OSP solder interconnects a) after reflow and b) after 250 hours of solid-state annealing at 125°C. OSP-Sn40BiCuNi-OSP solder interconnects c) after reflow and d) after 250 hours of solid-state annealing at 125°C. OSP-Sn56.5Bi0.5In-OSP solder interconnects e) after reflow and f) after 250 hours of solid-state annealing at 125°C

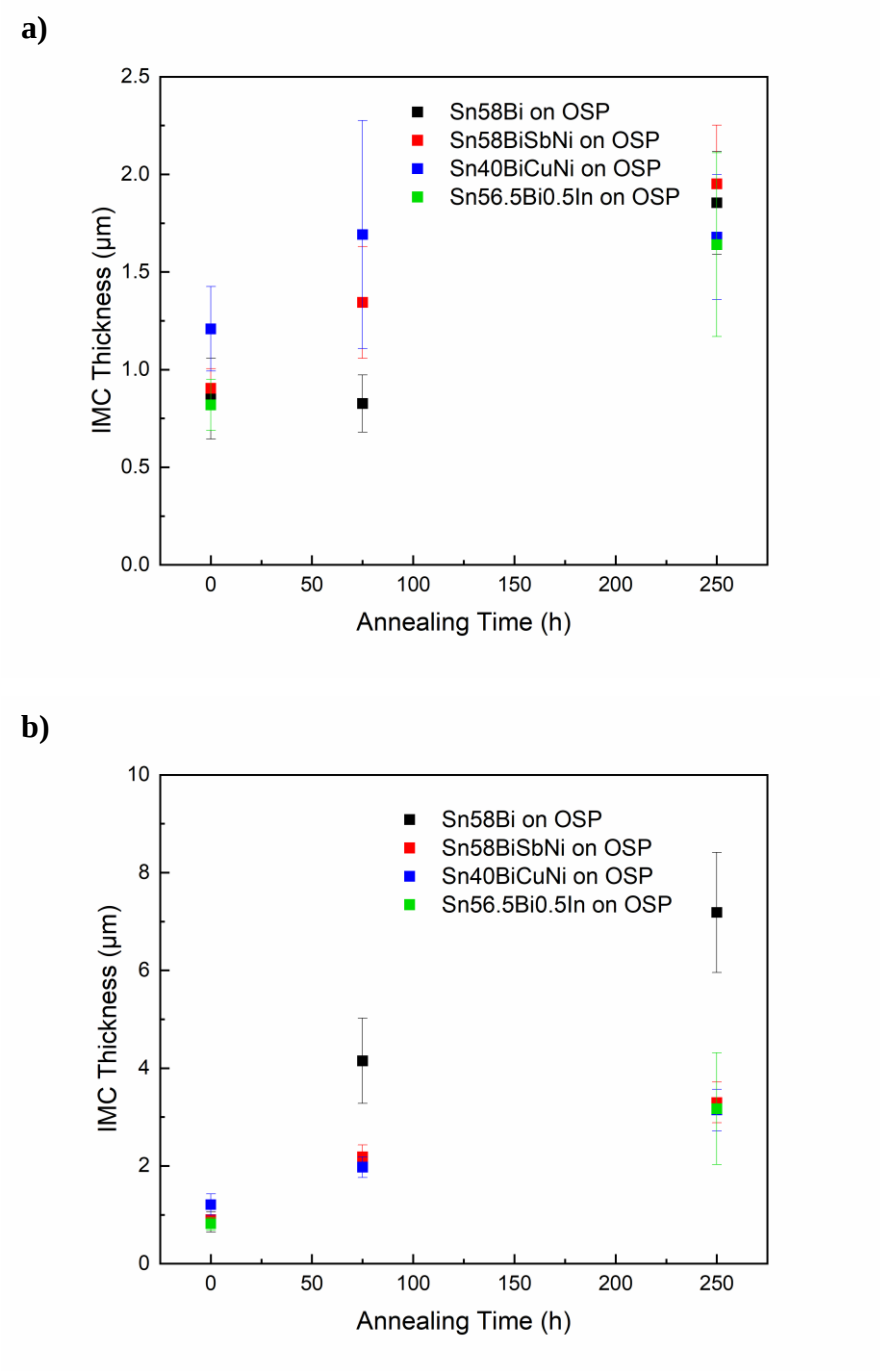

Figure 3.8. Intermetallic compound layer thickness change for Sn58Bi, Sn58BiSbNi, Sn40BiCuNi and Sn56.5Bi0.5In solders on OSP surface finish during solid state annealing at a) 85°C and b) 125°C

3.4.4 Intermetallic Compound Growth of SnBiSb, SnBiCu and SnBiIn on ENIG

The microstructure of Sn58BiSbNi, Sn40BiCuNi and Sn56.5Bi0.5In solder joints on ENIG surface finish after reflow and solid-state annealing are shown in Figure 3.9 below. After reflow, Ni_3Sn_4 was observed at solder-Ni interface in Sn58BiSbNi and Sn56.5Bi0.5In joints. in Sn40BiCuNi solder joints, with Cu additions, $(Cu,Ni)_6Sn_5$ instead of Ni_3Sn_4 forms at solder-Ni interface, which corresponds with ThermoCalc calculation. During aging, different solders showed different intermetallic compound growth rates. For Sn40BiCuNi joints, growth of $(Cu,Ni)_6Sn_5$ layer was observed during aging. In Sn56.5Bi0.5In joints, same as thermodynamic predictions, $(Au,Ni)Sn_4$ forms above the original Ni_3Sn_4 layer after aging. For Sn58BiSbNi interconnects, no $(Au,Ni)Sn_4$ layer was observed at solder-Ni interface after 250 hours of aging, but $(Au,Ni)Sn_4$ particles could be seen in the bulk. After aging, the solder joints were stored inside the freezer at -10°C. after two months of storage, a layer of $(Au,Ni)Sn_4$ was observed at the intermetallic compound layer, as shown in Figure 3.10. Therefore, with Sb additions, $(Au,Ni)Sn_4$ forms later at solder-Ni interface than Ag and In additions, but since $(Au,Ni)Sn_4$ already forms inside the bulk solder, it will eventually form the $(Au,Ni)Sn_4$ layer even at low aging temperature. The intermetallic compound growth rate for different alloys at 85°C and 125°C are summarized in Figure 3.11 below. According to previous research, SnBi eutectic experienced dramatic $(Au,Ni)Sn_4$ layer formation on ENIG at 125°C, a 50μm layer of $(Au,Ni)Sn_4$ was observed at SnBi-Ni interface with only 50nm of Au on ENIG surface finish. From the summarized intermetallic layer thickness, all Sb, Cu and In additions could significantly slow down $(Au,Ni)Sn_4$ layer growth on ENIG at 125°C. Although Sb and In additions could not eliminate $(Au,Ni)Sn_4$ layer formation, both Sb and In additions significantly slow down $(Au,Ni)Sn_4$ growth rate. Since no Sb-based or In-based intermetallic compounds were found inside bulk solder, the reason for $(Au,Ni)Sn_4$ growth rate slow down needs further study. At 85°C, all the alloys including Sn58Bi shows no big difference in intermetallic compound growth rate. Therefore, the catalyzation of $(Au,Ni)Sn_4$ layer is triggered by high aging temperature.

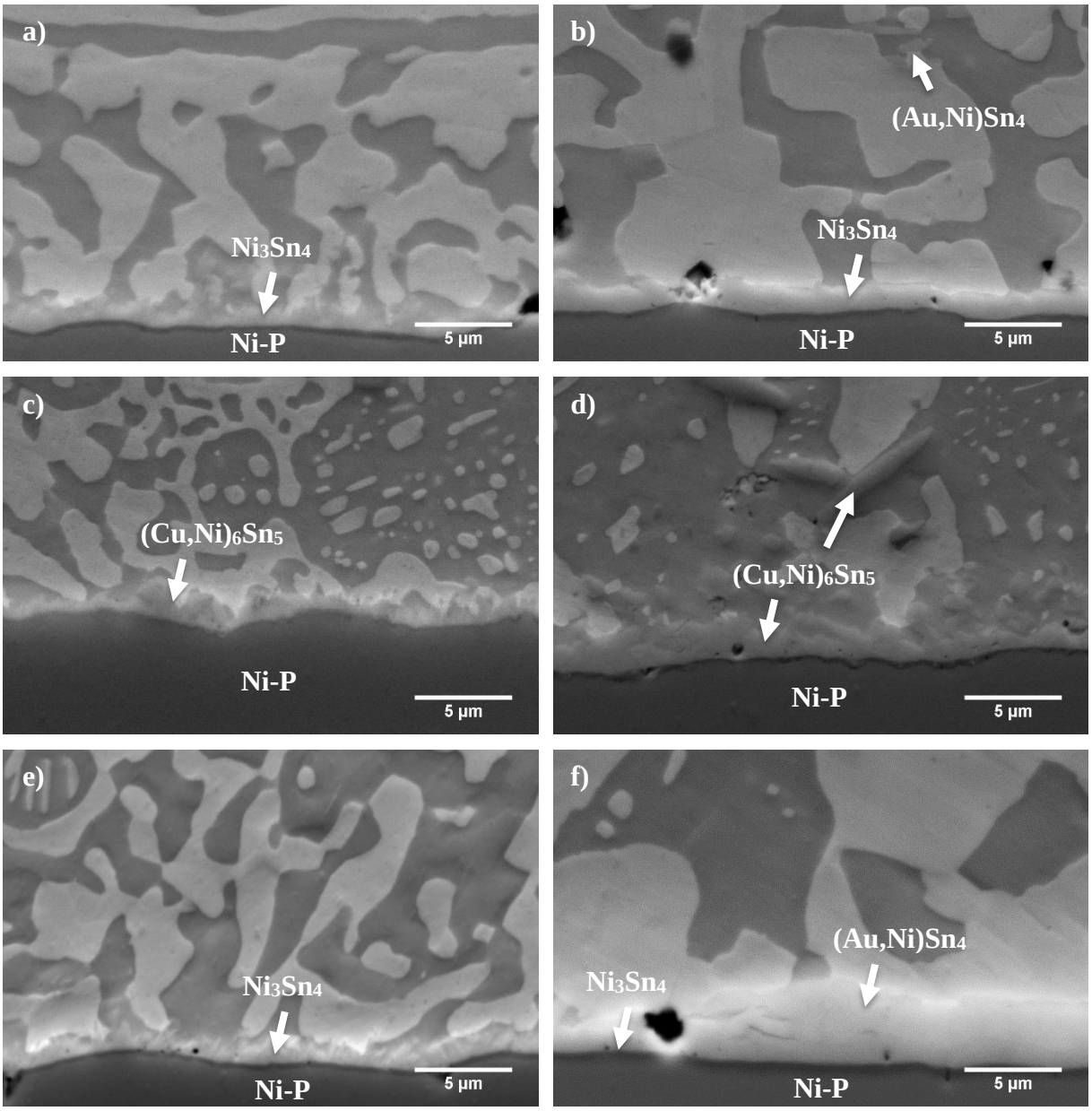

Figure 3.9. Microstructure of a) solder-Ni interface of intermetallic layers of ENIG-Sn58BiSbNi-ENIG solder interconnects after reflow; b) solder-Ni interface of intermetallic layers of ENIG-Sn58BiSbNi-ENIG solder interconnects after 250 hours of solid-state annealing at 125°C; c) solder-Ni interface of ENIG-Sn40BiCuNi-ENIG solder interconnects after reflow; d) solder-Ni interface of ENIG-Sn40BiCuNi-ENIG solder interconnects after 250 hours of solid-state annealing at 125°C; e) solder-Ni interface of intermetallic layers of ENIG-Sn56.5Bi0.5In-ENIG solder interconnects after reflow; and f) solder-Ni interface of intermetallic layers of ENIG-Sn56.5Bi0.5In-ENIG solder interconnects after 250 hours of solid-state annealing at 125°C

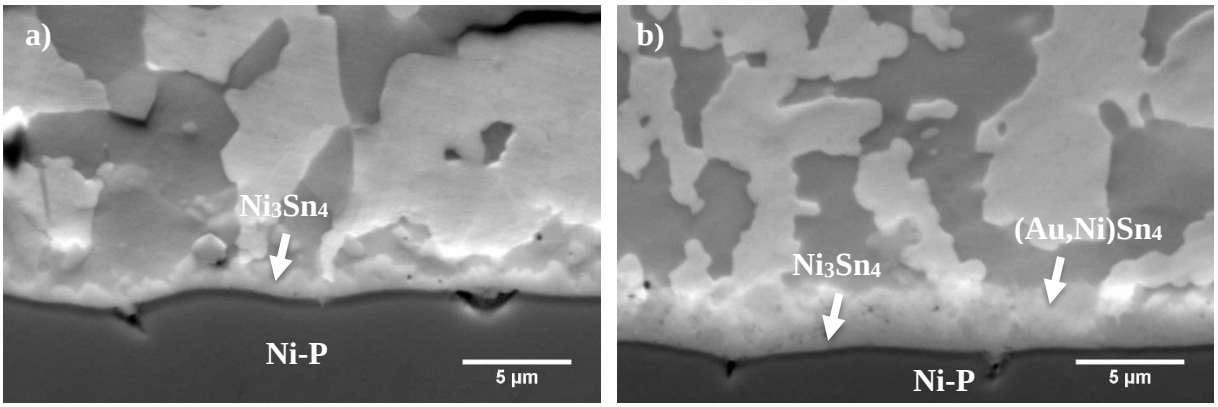

Figure 3.10. Microstructure of a) solder-Ni interface of intermetallic layers of ENIG-Sn58BiSbNi-ENIG solder interconnects after 250 hours of solid-state annealing at 85°C and b) solder-Ni interface of intermetallic layers of ENIG-Sn58BiSbNi-ENIG solder interconnects after 250 hours of solid-state annealing at 85°C followed by 2 months of storage at -10°C, which caused the formation of the $(Au,Ni)Sn_4$ layer

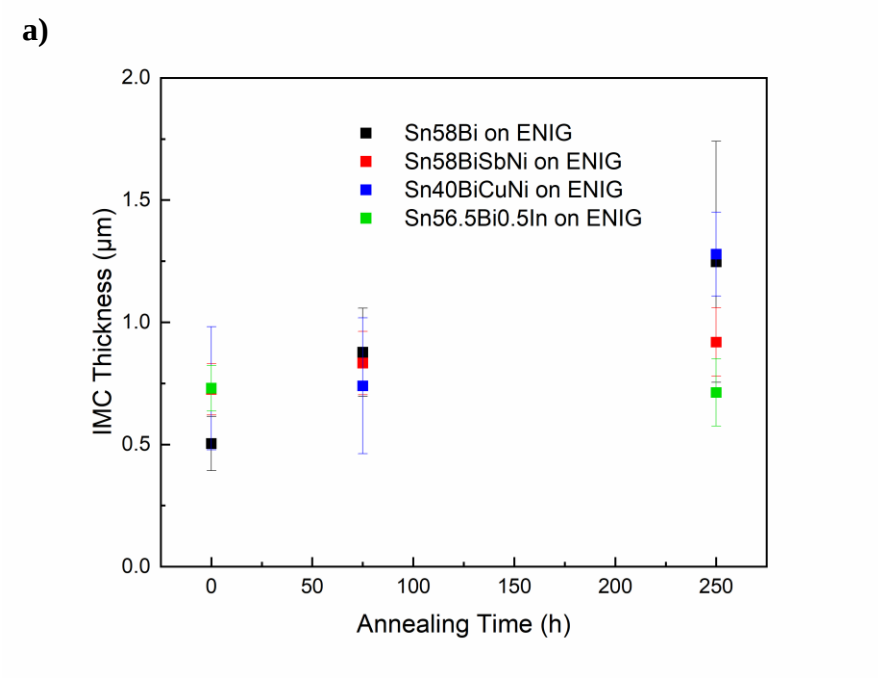

Figure 3.11. Intermetallic compound layer thickness change for Sn58Bi, Sn58BiSbNi, Sn40BiCuNi and Sn56.5Bi0.5In solders on ENIG surface finish during solid state annealing at a) 85°C and b) 125°C

Figure 3.11 continued

b)

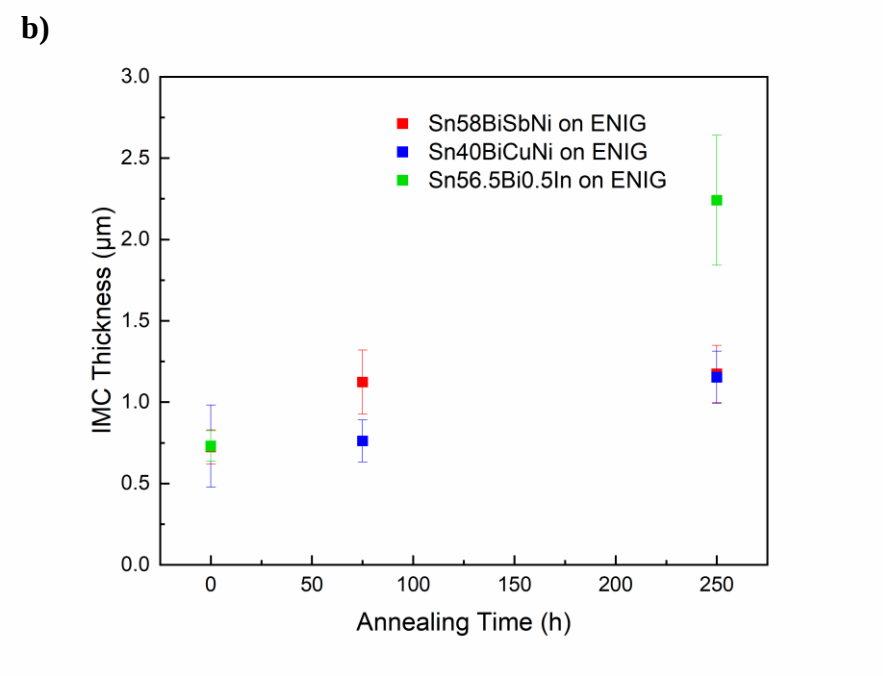

3.4.5 Mechanical Characterization & Failure Analysis of SnBiSb, SnBiCu Joints

The microstructure of fractured Sn58BiSbNi and Sn40BiCuNi joints on OSP surface finish is shown in Figure 3.12. After reflow, ductile fatigue failures were observed in both Sn58BiSbNi and Sn40BiCuNi joints, and the cracks propagate inside the bulk solder. However for fractured Sn40BiCuNi joints, the crack is very close to the intermetallic layer. After 250 hours of aging at 125°C, the fatigue reliability of Sn58BiSbNi becomes much worse, which shows as the drop of N_{50} cycles (numbers of cycles needed for the loading strength of the joint to drop 50%) to 0 on Figure 3.14, which indicates a brittle failure. The fracture path, although still inside bulk solder, moves towards the intermetallic compound layer. The brittle fractures observed in aged Sn58BiSbNi joints on OSP is peculiar, as all of the other aged SnBi-based solders tested did not experience embrittlement during aging. The reason for the embrittlement in Sn58BiSbNi during aging still needs further study. Sn40BiCuNi joints on the other hand, shows even better fatigue reliability after aging, and the fracture path moves inside the bulk solder, showing a ductile failure nature. After comparison, although Sn40BiCuNi does not have a high fatigue reliability after reflow, but the fatigue reliability of Sn40BiCuNi joints on OSP significantly improves after aging, out-performing all the other three SnBi-based alloys, only inferior to SAC305.

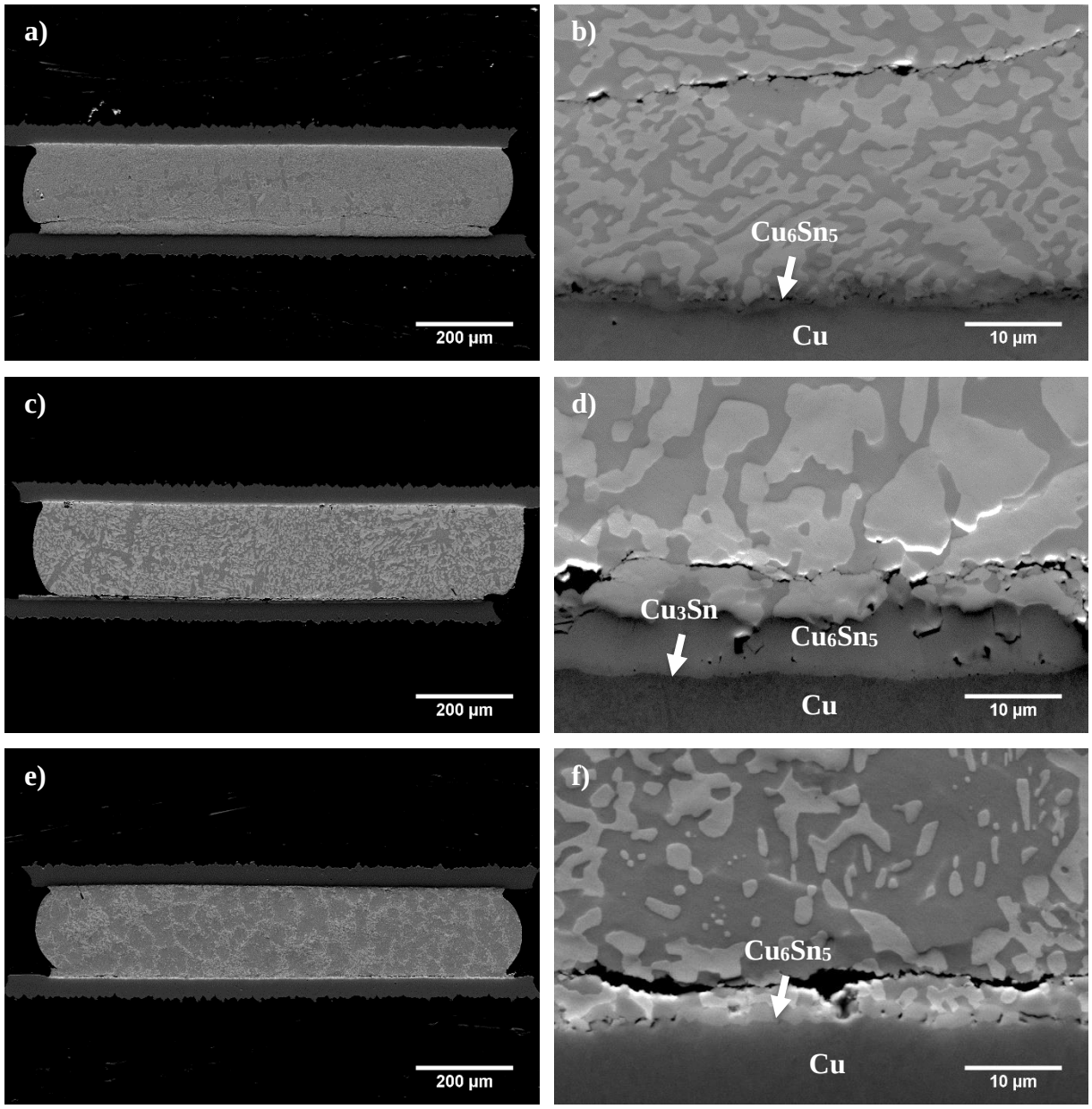

Figure 3.12. Microstructure of a) fatigue-loaded OSP-Sn58BiSbNi-OSP solder interconnects after reflow; b) higher magnification image at solder-Cu interface of a) showing the details of fractures; c) fatigue-loaded OSP-Sn58BiSbNi-OSP solder interconnects after 250°C of solid-state annealing; and d) higher magnification image at solder-Cu interface of c) showing the details of fractures; e) fatigue-loaded OSP-Sn40BiCuNi-OSP solder interconnects after reflow; f) higher magnification image at solder-Cu interface of e) showing the details of fractures; g) fatigue-loaded OSP-Sn40BiCuNi-OSP solder interconnects after 250°C of solid-state annealing; and h) higher magnification image at solder-Cu interface of g) showing the details of fractures

Figure 3.12 continued

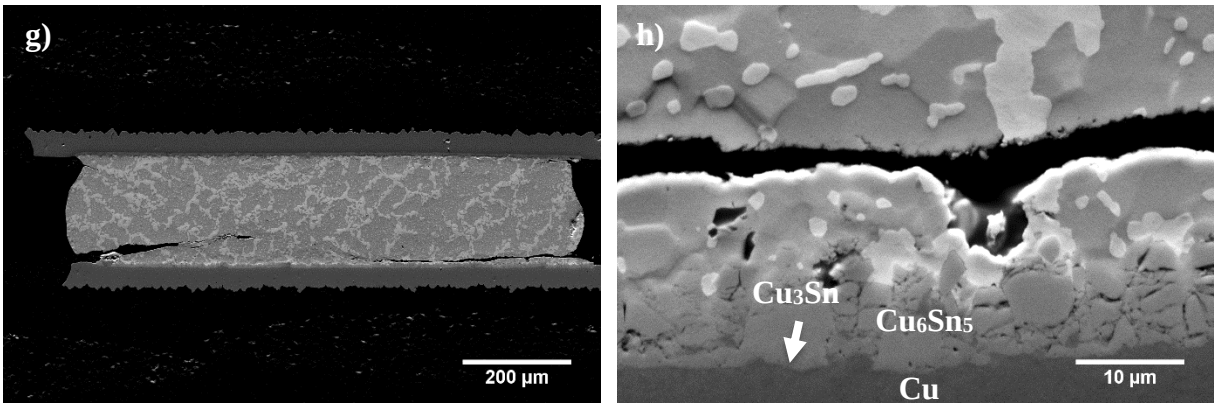

The microstructure of fractured Sn58BiSbNi and Sn40BiCuNi joints on ENIG surface finish is shown in Figure 3.13. After reflow, ductile fatigue failures were observed in both Sn58BiSbNi and Sn40BiCuNi, with both cracks propagating inside the bulk solder. After aging at 125°C, brittle failures were observed in Sn58BiSbNi joints, with the cracks propagating along the interface between bulk solder and intermetallic compound layer and the drop of N_{50} cycles to 0 shown in Figure 3.14. The same embrittlement effect was also observed in aged Sn58Bi and Sn57Bi1Ag joints in previous study, which was caused by the formation of $(Au,Ni)Sn_4$ layer. Since the same intermetallic compounds were found in Sn58BiSbNi, the formation of $(Au,Ni)Sn_4$ due to Au on ENIG surface finish is still the reason for the embrittlement in Sn58BiSbNi during aging. For Sn40BiCuNi, different intermetallic compounds form on ENIG surface finish due to Cu additions, the failure mode of the aged joints is different. Typical fatigue failure was observed in aged Sn40BiCuNi joints, with cracks along with either solder/IMC interface or inside bulk solder, but very close to the intermetallic layer. The N_{50} cycles of the aged Sn40BiCuNi joints is better than the as-reflowed ones, and Sn40BiCuNi is the only SnBi-based solder studied so far which did not experience brittle fracture after aging. However, the fatigue reliability for the aged Sn40BiCuNi joints is still very low.

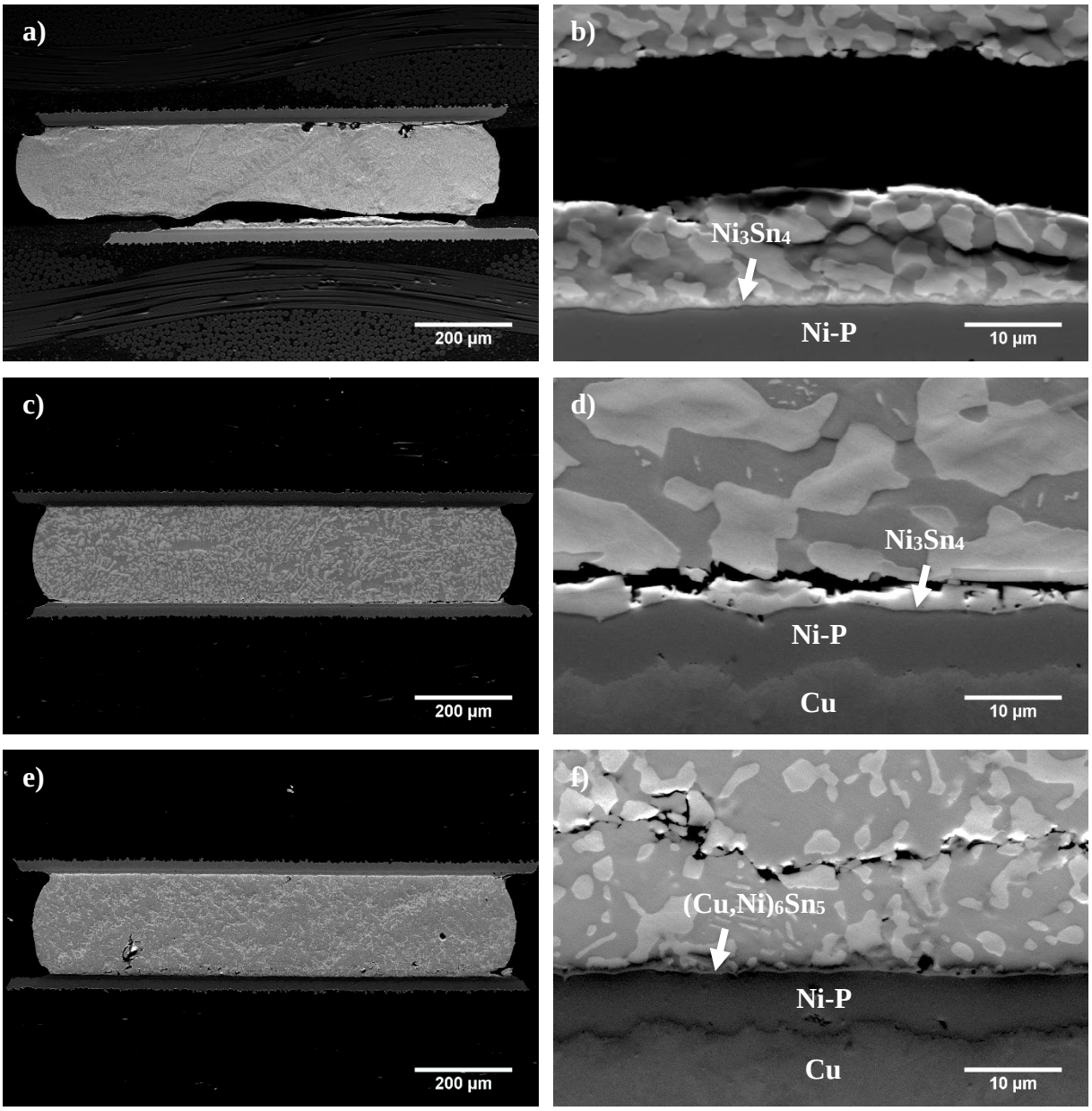

Figure 3.13. Microstructure of a) fatigue-loaded ENIG-Sn58BiSbNi-ENIG solder interconnects after reflow; b) higher magnification image at solder-Ni interface of a) showing the details of fractures; c) fatigue-loaded ENIG-Sn58BiSbNi-ENIG solder interconnects after 250°C of solid-state annealing; and d) higher magnification image at solder-Ni interface of c) showing the details of fractures; e) fatigue-loaded ENIG-Sn40BiCuNi-ENIG solder interconnects after reflow; f) higher magnification image at solder-Ni interface of e) showing the details of fractures; g) fatigue-loaded ENIG-Sn40BiCuNi-ENIG solder interconnects after 250°C of solid-state annealing; and h) higher magnification image at solder-Ni interface of g) showing the details of fractures

Figure 3.13 continued

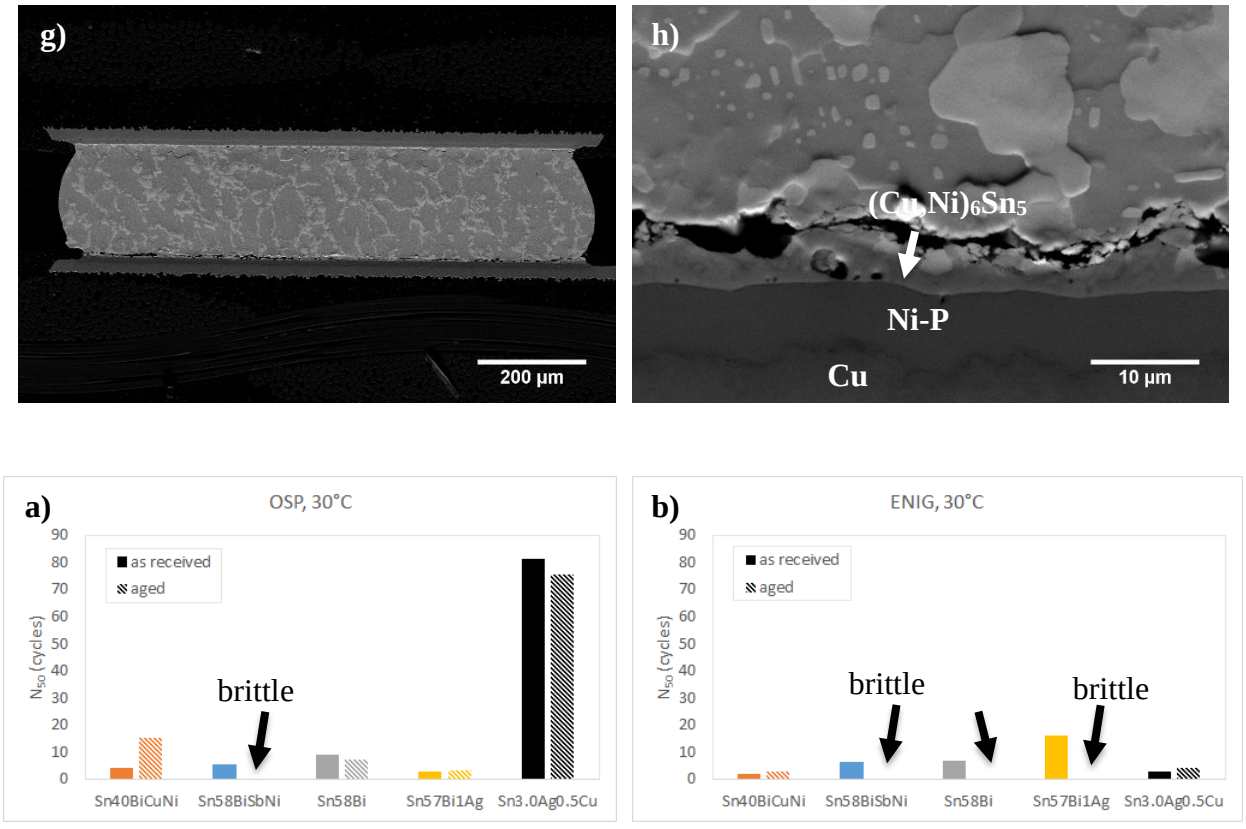

Figure 3.14. Fatigue reliability and N_{50} cycles for Sn58Bi, Sn57Bi1Ag, Sn3.0Ag0.5Cu, Sn58BiSbNi and Sn40BiCuNi after reflow and 250 hours of aging at 125°C on a) OSP and b) ENIG surface finishes

3.5 Conclusions

SnBi low temperature solders are considered as a promising candidate as substituting traditional SAC alloys to prevent component warpage in the future electronics industry. Thermodynamics calculation, intermetallic growth and fatigue reliability study were carried out in this study to understand the microstructural evolution characteristics and mechanical properties of SnBi alloys with Sb, Cu and In additions. The following conclusions could be drawn from this study:

- Cu_6Sn_5 and Cu_3Sn intermetallic compounds form on SnBi solders with Sb, Cu and In additions on OSP surface finish, all these three additions have an effect on slowing down Cu_6Sn_5 layer growth during aging at 125°C compared with Sn58Bi alloy. However, the difference in intermetallic compound growth at 85°C is negligible for Sn58Bi, Sn58BiSbNi, Sn40BiCuNi and Sn56.5Bi0.5In.

- For Sn58BiSbNi and Sn56.5Bi0.5In on ENIG surface finish, Ni_3Sn_4 forms on solder-Ni interface after reflow. However, during further annealing or even low temperature aging, Au on ENIG catalyzes $(Au,Ni)Sn_4$ layer formation and growth in both Sn58BiSbNi and Sn56.5Bi0.5In joints. Compared with Sn58Bi, Sb and In additions could significantly slow down the $(Au,Ni)Sn_4$ layer growth at 125°C, but cannot eliminate the formation of $(Au,Ni)Sn_4$ on ENIG surface finish.
- For Sn40BiCuNi alloy on ENIG surface finish, with Cu additions, $(Cu,Ni)_6Sn_5$ instead of Ni_3Sn_4 and $(Au,Ni)Sn_4$ forms at solder-Ni interface after reflow and aging. The formation and growth of $(Au,Ni)Sn_4$ is eliminated by Cu additions.
- Fatigue reliability testing reveals the Au embrittlement effect in Sn58BiSbNi-ENIG interconnects during aging. Sn40BiCuNi-ENIG joints shows better fatigue reliability due to elimination of $(Au,Ni)Sn_4$, but the fatigue life is still very low. For future low temperature solder development, Sn58BiSbNi and Sn40BiCuNi solders are not recommended to join with ENIG metallization.
- The fatigue reliability of Sn40BiCuNi on OSP significantly increases during aging and outperforms all the other SnBi-based alloys tested. However, Sn58BiSbNi still experiences embrittlement on OSP during solid-state annealing.

3.6 Acknowledgment

The authors want to acknowledge Intel Cooperation for the grant on supporting this research.

3.7 References

[1] Bath, J., Garcia, R., Uchida, N., Takahashi, H., Clark, G., & Itoh, M. (2009). Investigation and development of tin-lead and lead-free solder pastes to reduce the head-in-pillow component soldering defect. SMTA International Proceedings 2009.

[2] Boettinger, W. J., Handwerker, C. A., Newbury, B., Pan, T. Y., & Nicholson, J. M. (2002). Mechanism of fillet lifting in Sn-Bi alloys. Journal of electronic materials, 31(5), 545-550.

[3] Henshall, Gregory, Jasbir Bath, and Carol A. Handwerker, eds. Lead-free solder process development. John Wiley & Sons, 2011.

[4] Hua, F., Mei, Z., & Glazer, J. (1998, May). Eutectic Sn-Bi as an alternative to Pb-free solders. In 1998 Proceedings. 48th Electronic Components and Technology Conference (Cat. No. 98CH36206) (pp. 277-283). IEEE.

[5] Ferrer, E., & Holder, H. (2003, March). 57Bi-42Sn-1Ag: A Lead Free, Low Temperature Solder for the Electronic Industry. In JEDEX Conference, San Jose, CA, March (pp. 22-25).

[6] Aspandiar, R., Byrd, K., Tang, K. K., Campbell, L., & Mokler, S. (2015, February). Investigation of low temperature solders to reduce reflow temperature, improve SMT yields and realize energy savings. In Proceedings of the 2015 APEX Conference.

[7] Chen, O. H., Byrd, K., Mokler, S., Tang, K. K., & Aspandiar, R. (2015, May). Comparison of the Mechanical Shock/Drop Reliability of Flip Chip BGA (FCBGA) Solder Joints Formed by Soldering with Low Temperature BiSn-Based Resin Reinforced Solder Pastes. In Proceedings of the International Conference on Soldering and Reliability.

[8] Chen, O. H., Molina, A., Aspandiar, R., Byrd, K., Mokler, S., & Tang, K. K. (2015, September). Mechanical shock and drop reliability evaluation of the BGA solder joint stack-ups formed by reflow soldering SAC solder balls BGAs with BiSnAg and resin reinforced BiSn-based solder pastes. In Proceedings of SMTA International (pp. 215-222).

[9] Mokler, S., Aspandiar, R., Byrd, K., Chen, O., Walwadkar, S., Tang, K. K., ... & Sane, S. (2016, September). The application of Bi-based solders for low temperature reflow to reduce cost while improving SMT yields in client computing systems. In Proceedings of SMTA International (pp. 318-326).

[10] Silva, B. L., Xavier, M. G., Garcia, A., & Spinelli, J. E. (2017). Cu and Ag additions affecting the solidification microstructure and tensile properties of Sn-Bi lead-free solder alloys. Materials Science and Engineering: A, 705, 325-334.

[11] Sahasrabudhe, S., Mokler, S., Renavikar, M., Sane, S., Byrd, K., Brigham, E., ... & Parupalli, S. (2018, May). Low Temperature Solder-A Breakthrough Technology for Surface Mounted Devices. In 2018 IEEE 68th Electronic Components and Technology Conference (ECTC) (pp. 1455-1464). IEEE.

[12] Lee, Byeong-Joo, Chang-Seok Oh, and Jae-Hyeok Shim. "Thermodynamic assessments of the Sn-In and Sn-Bi binary systems." Journal of electronic materials 25.6 (1996): 983-991.

[13] Kim, J. H., Lee, Y. C., Lee, S. M., & Jung, S. B. (2014). Effect of surface finishes on electromigration reliability in eutectic Sn–58Bi solder joints. Microelectronic engineering, 120, 77-84.

[14] Liu, P. L., & Shang, J. K. (2005). Fracture of Sn-Bi/Ni (P) interfaces. Journal of materials research, 20(4), 818-826.

[15] Yoon, J. W., Lee, C. B., & Jung, S. B. (2002). Interfacial reactions between Sn-58 mass% Bi eutectic solder and (Cu, electroless Ni-P/Cu) substrate. Materials transactions, 43(8), 1821-1826.

[16] Lee, S. M., Yoon, J. W., & Jung, S. B. (2015). Interfacial reaction and mechanical properties between low melting temperature Sn–58Bi solder and various surface finishes during reflow reactions. Journal of Materials Science: Materials in Electronics, 26(3), 1649-1660.

[17] Zou, H. F., Zhang, Q. K., & Zhang, Z. F. (2012). Interfacial microstructure and mechanical properties of Sn-Bi/Cu joints by alloying Cu substrate. Materials Science and Engineering: A, 532, 167-177.

[18] Myung, W. R., Kim, Y., Kim, K. Y., & Jung, S. B. (2016). Drop reliability of epoxy-contained Sn-58 wt.% Bi solder joint with ENIG and ENEPIG surface finish under temperature and humidity test. Journal of Electronic Materials, 45(7), 3651-3658.

[19] Chen, L. T., & Chen, C. M. (2006). Electromigration study in the eutectic Sn-Bi solder joint on the Ni/Au metallization. Journal of materials research, 21(4), 962-969.

[20] Young, B. L., Duh, J. G., & Jang, G. Y. (2003). Compound formation for electroplated Ni and electroless Ni in the under-bump metallurgy with Sn-58Bi solder during aging. Journal of electronic materials, 32(12), 1463-1473.

[21] Tao, W. H., Chen, C., Ho, C. E., Chen, W. T., & Kao, C. R. (2001). Selective interfacial reaction between Ni and eutectic BiSn lead-free solder. Chemistry of materials, 13(3), 1051-1056.

[22] Wang, J., Liu, H. S., Liu, L. B., & Jin, Z. P. (2006). Interfacial reaction between Sn-Bi alloy and Ni substrate. Journal of electronic materials, 35(10), 1842-1847.

[23] Chiu, M. Y., Chang, S. Y., Tseng, Y. H., Chan, Y. C., & Chuang, T. H. (2002). Characterization of intermetallic compounds formed during the interfacial reactions of liquid Sn and Sn-58Bi solders with Ni substrates. ZeitschriftfürMetallkunde, 93(3), 248-252.140: SnAgCu, ENIG, IMC

[24] Pun, K. P., Islam, M. N., Rotanson, J., Cheung, C. W., & Chan, A. H. (2018). Enhancement of Sn-Bi-Ag Solder Joints with ENEPIG Surface Finish for Low-Temperature Interconnection. Journal of Electronic Materials, 47(9), 5191-5202.

[25] Li, J. F., Mannan, S. H., Clode, M. P., Whalley, D. C., & Hutt, D. A. (2006). Interfacial reactions between molten Sn–Bi–X solders and Cu substrates for liquid solder interconnects. Acta Materialia, 54(11), 2907-2922.

[26] Li, J., Mannan, S. H., Clode, M. P., Liu, C., Chen, K., Whalley, D. C., ... & Conway, P. P. (2008). Interfacial reaction between molten Sn-Bi based solders and electroless Ni-P coatings for liquid solder interconnects. IEEE Transactions on Components and Packaging Technologies, 31(3), 574-585.

[27] Li, J. F., Mannan, S. H., Clode, M. P., Chen, K., Whalley, D. C., Liu, C., & Hutt, D. A. (2007). Comparison of interfacial reactions of Ni and Ni–P in extended contact with liquid Sn–Bi-based solders. Actamaterialia, 55(2), 737-752.

[28] Dong, W., Shi, Y., Xia, Z., Lei, Y., & Guo, F. (2008). Effects of trace amounts of rare earth additions on microstructure and properties of Sn-Bi-based solder alloy. Journal of Electronic Materials, 37(7), 982-991.

[29] Myung, W. R., Ko, M. K., Kim, Y., & Jung, S. B. (2015). Effects of Ag content on the reliability of LED package component with Sn–Bi–Ag solder. Journal of Materials Science: Materials in Electronics, 26(11), 8707-8713.

[30] Guan, Z. M., Liu, G. X., & Liu, T. (2000). Kinetics of interface reaction in 40Sn-Bi/Cu and 40Sn-Bi-2Ag/Cu systems during aging in solid state. IEEE transactions on advanced packaging, 23(4), 737-742.

[31] Suganuma, K., Sakai, T., Kim, K. S., Takagi, Y., Sugimoto, J., &Ueshima, M. (2002). Thermal and mechanical stability of soldering QFP with Sn-Bi-Ag lead-free alloy. IEEE Transactions on electronics packaging manufacturing, 25(4), 257-261.

[32] Lai, Z., & Ye, D. (2016). Microstructure and Properties of Sn-10Bi-xCu Solder Alloy/Joint. Journal of Electronic Materials, 45(7), 3702-3711.

[33] Zhang, C., Liu, S. D., Qian, G. T., Jian, Z. H. O. U., & Feng, X. U. E. (2014). Effect of Sb content on properties of Sn—Bi solders. Transactions of Nonferrous Metals Society of China, 24(1), 184-191.

[34] Mokhtari, O., & Nishikawa, H. (2016). Correlation between microstructure and mechanical properties of Sn–Bi–X solders. Materials Science and Engineering: A, 651, 831-839.

[35] Mokhtari, O., & Nishikawa, H. (2014). Effects of In and Ni addition on microstructure of Sn-58Bi solder joint. Journal of electronic materials, 43(11), 4158-4170.

[36] Chen, X., Xue, F., Zhou, J., & Yao, Y. (2015). Effect of In on microstructure, thermodynamic characteristic and mechanical properties of Sn–Bi based lead-free solder. Journal of Alloys and Compounds, 633, 377-383.

[37] Li, Q., Ma, N., Lei, Y., Lin, J., Fu, H., & Gu, J. (2016). Characterization of low-melting-point Sn-Bi-In lead-free solders. Journal of Electronic Materials, 45(11), 5800-5810.

[38] Huang, Y. C., & Chen, S. W. (2011). Effects of Co alloying and size on solidification and interfacial reactions in Sn-57 wt.% Bi-(Co)/Cu couples. Journal of electronic materials, 40(1), 62-70.

[39] Zhou, S., Mokhtari, O., Rafique, M. G., Shunmugasamy, V. C., Mansoor, B., & Nishikawa, H. (2018). Improvement in the mechanical properties of eutectic Sn58Bi alloy by 0.5 and 1 wt% Zn addition before and after thermal aging. Journal of Alloys and Compounds, 765, 1243-1252.

[40] Mokhtari, O., Zhou, S., YC, C., & Nishikawa, H. (2016). Effect of Zn addition on interfacial reactions between Sn-Bi solder and Cu substrate. Materials Transactions, 57(8), 1272-1276.

[41] Wang, F., Chen, H., Huang, Y., Liu, L., & Zhang, Z. (2019). Recent progress on the development of Sn–Bi based low-temperature Pb-free solders. Journal of Materials Science: Materials in Electronics, 30(4), 3222-3243.

[42] Sakuyama, S., Akamatsu, T., Uenishi, K., & Sato, T. (2009). Effects of a third element on microstructure and mechanical properties of eutectic Sn–Bi solder. Transactions of The Japan Institute of Electronics Packaging, 2(1), 98-103.

[43] Shen, J., Wu, C., & Li, S. (2012). Effects of rare earth additions on the microstructural evolution and microhardness of Sn30Bi0. 5Cu and Sn35Bi1Ag solder alloys. Journal of Materials Science: Materials in Electronics, 23(1), 156-163.

[44] Shen, L., Tan, Z. Y., & Chen, Z. (2013). Nanoindentation study on the creep resistance of SnBi solder alloy with reactive nano-metallic fillers. Materials Science and Engineering: A, 561, 232-238.

[45] Shen, J., Pu, Y., Yin, H., & Tang, Q. (2015). Effects of Cu, Zn on the wettability and shear mechanical properties of Sn-Bi-based lead-free solders. Journal of Electronic Materials, 44(1), 532-541.

[46] Shalaby, R. M. (2013). Effect of silver and indium addition on mechanical properties and indentation creep behavior of rapidly solidified Bi–Sn based lead-free solder alloys. Materials Science and Engineering: A, 560, 86-95.

[47] Mokhtari, O., & Nishikawa, H. (2016). Correlation between microstructure and mechanical properties of Sn–Bi–X solders. Materials Science and Engineering: A, 651, 831-839.

3.8 Appendix

a)

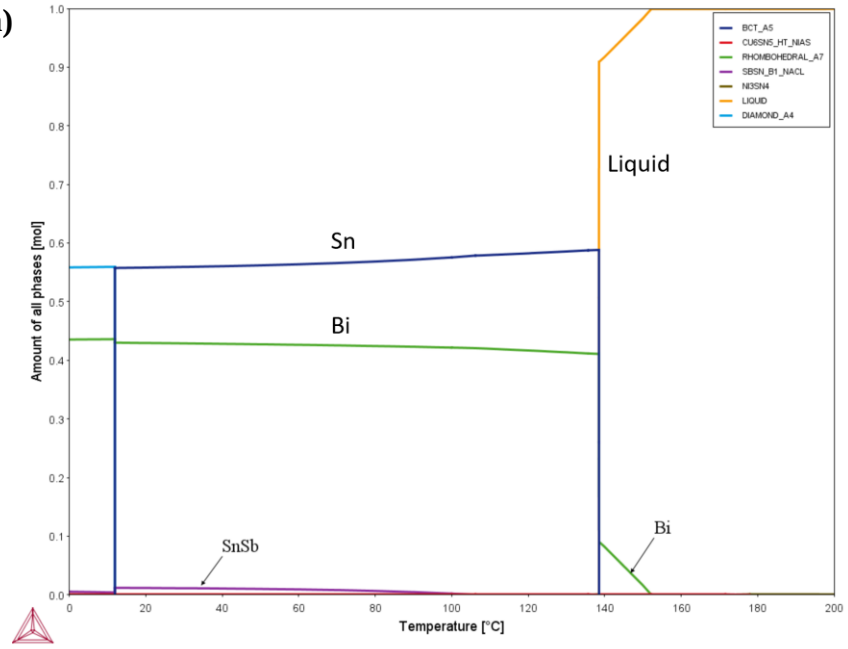

Figure 3.15. Thermodynamic simulation of phases at equilibrium in a) Sn58BiSbNi; b) Sn40BiCuNi and c) Sn56.5Bi0.5In

Figure 3.15 continued

b)

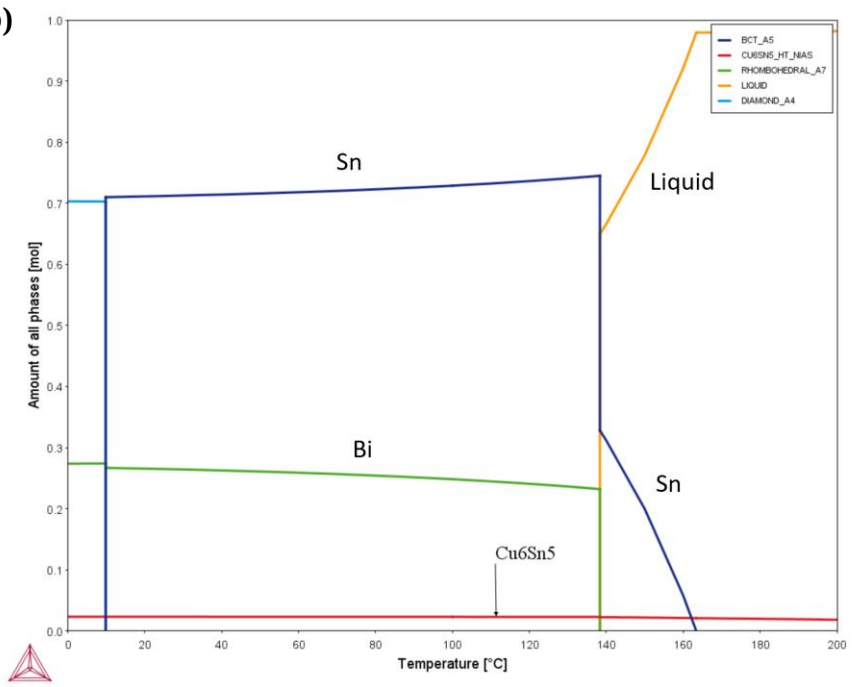

c)

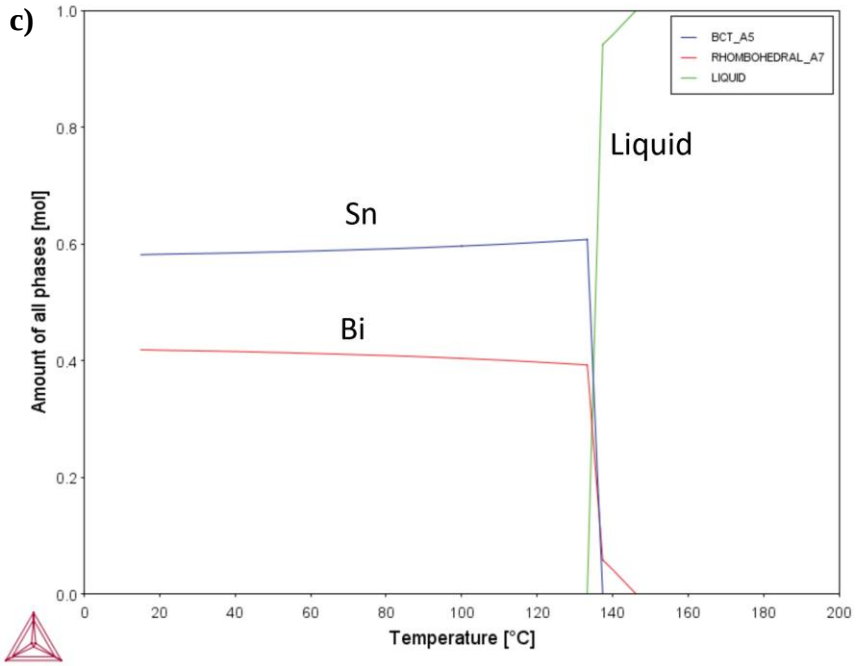

4. MICROALLOYING EFFECTS ON INTERMETALLIC COMPOUND GROWTH AND MECHANICAL RELIABILITY OF TIN-BISMUTH SOLDER JOINTS

4.1 Abstract

A new low temperature interconnect technology based on Sn-Bi alloys is being considered as a substitute for Sn-Ag-Cu (SAC) solder BGAs to form joints with significantly lower melting temperatures than homogeneous SAC joints. Microstructure development studies of reflow and aging and intermetallic growth are important in understanding mechanical reliability and failure paths in the resulting homogeneous joints. This study focused on microstructure evolution in SnBi eutectic, SnBiAg eutectic and HRL1 solders (MacDermid Alpha) homogeneous joints and hybrid joints with SAC305 formed with electroless nickel immersion gold (ENIG) and organic surface protection (OSP) surface finishes. Experimental results revealed that with more microalloying elements, HRL1 has significantly refined microstructure and slower Sn grain growth rate during solid-state aging compared with SnBi and SnBiAg eutectic alloys. Intermetallic compound growth study showed that during solid state annealing following reflow, the (50nm) Au from the ENIG finish catalyzed rapid (Au,Ni)Sn_4 intermetallic growth at the Ni-solder interface in both Sn-Bi and Sn-Bi-Ag homogeneous joints, which led to significant solder joint embrittlement during creep and fatigue loading. However, (Au,Ni)Sn_4 growth and gold embrittlement was completely eliminated for HRL1 due to Cu additions in it, and HRL1 has significantly better fatigue reliability than SnBi and SnBiAg eutectic alloys on both OSP and ENIG surface finishes.

Keywords: Tin-bismuth solder, HRL1, microstructure refinement, gold embrittlement elimination

4.2 Introduction

As integrated circuits have become larger and thinner, chip warpage during reflow has become an increasing issue, with warpage increasing with increasing reflow temperature. Tin-silver-copper (SAC) alloys, the industry standard, require peak reflow temperatures of approximately 240°C due to their high eutectic temperature (217°C). Such high reflow temperatures have been observed to cause serious warpage-induced defects, such as separation of SAC solder balls from SAC solder paste before melting (217°C) to form head-on-pillow (HoP) defects along the edges of the IC and

bridging in the center [1, 2]. A schematic illustration of chip warpage and resulting defects is shown in Figure 4.1. In HoP, the connections between solder on the board side and the ball are weak, based on Van der Waals forces. Therefore, when the component encounters large thermal or mechanical stresses during use, HoP defects can cause electrical failure in the component [3]. Solder joints in the center of the packaging may also form bridging defects, which could cause short circuit and component failure.

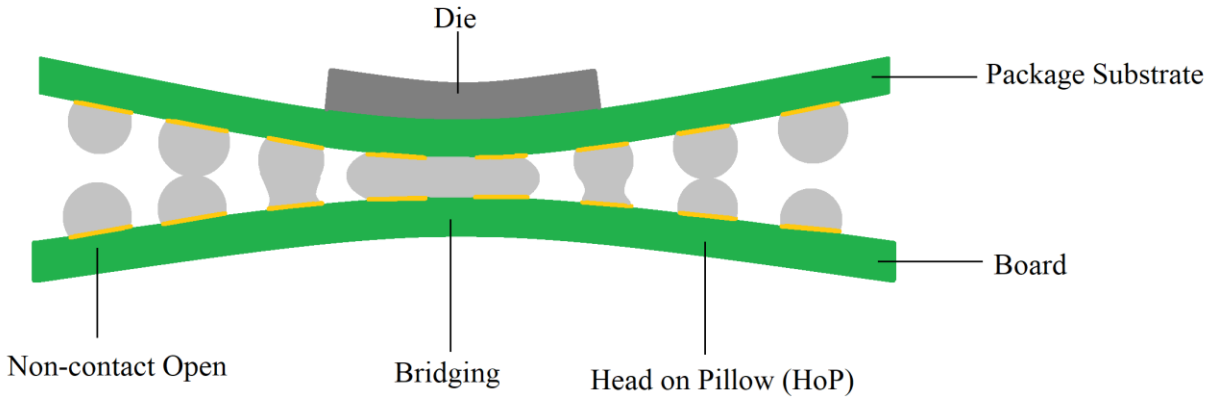

Figure 4.1. Schematic illustration of component warpage and different defects formed during reflow soldering

As a result, low temperature soldering (LTS) systems have been recommended as a solution to reduce heating-induced warpage [4-11]. Solders based on eutectic Sn-Bi solders have been used widely in low temperature soldering due to their low eutectic temperature [12], as well as low cost and toxicity. To lower the reflow temperature with the assistance of Sn-Bi-based alloys, two different kinds of geometries have been proposed. Solders based on Sn-Bi eutectic could be used instead of SAC solder paste to assemble components with SAC solder balls to form "hybrid" joints after soldering, as shown in Figure 4.2 below. Another way of achieving low temperature soldering is to replace both the ball and the paste with Sn-Bi-based alloys to form homogeneous joints after reflow, as shown in Figure 4.3. For both geometries, only melting of Sn-Bi-based alloys with their lower liquidus temperatures is required. For the Sn-Bi eutectic temperature of 139°C, a reflow temperature of approximately 160-190°C is required, lowering the peak reflow temperature by 50-80°C.

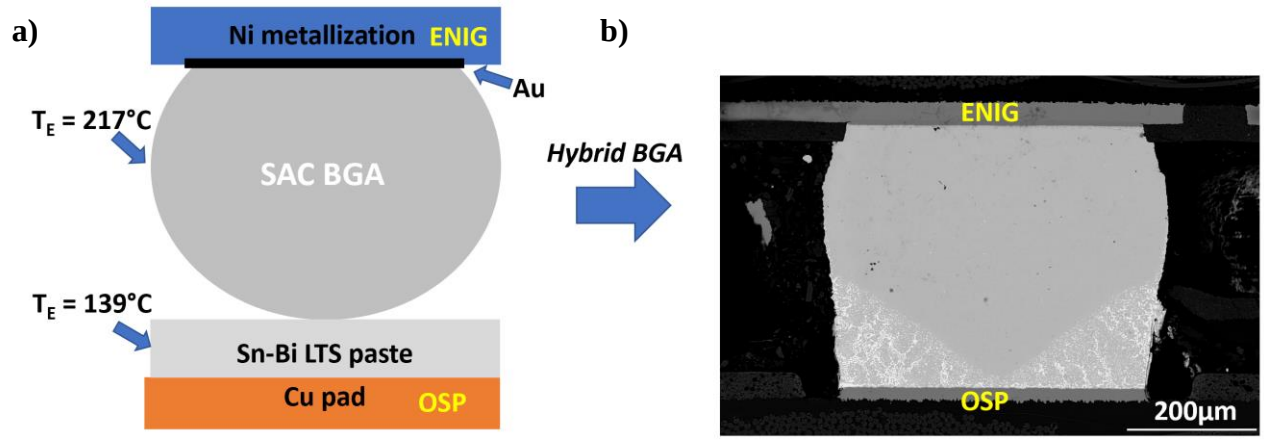

Figure 4.2. a) A schematic illustration of hybrid joints before reflow, when Sn-Bi LTS pastes substitutes SAC solder paste during surface mount procedure; b) typical microstructure of a LTS-SAC hybrid joint after reflow showing the Bi diffusion region and the un-melted SAC region

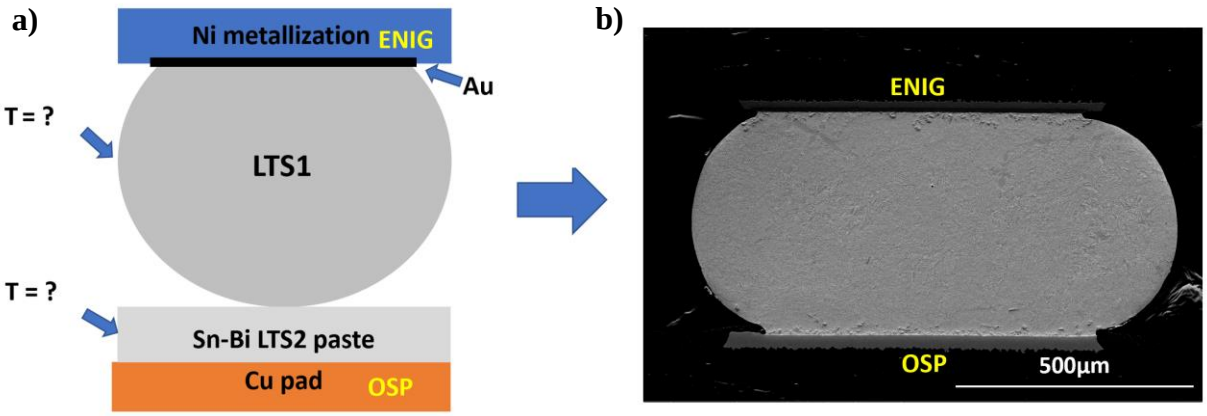

Figure 4.3. a) A schematic illustration of Sn-Bi homogeneous joints before reflow, when Sn-Bi LTS pastes substitutes both SAC solder paste and SAC BGA during surface mount procedure; b) microstructure of a Sn57Bi1Ag homogeneous joint after reflow

For the new SnBi alloys, their reliability during application is the most important issue in order to finish the transfer from SAC solders to SnBi-based alloys. However, from previous studies, compared with SAC alloys, there have been concerns about the SnBi-based alloys on the capability of the packages, such as poor drop shock resistance [13,14] and limited thermal cycling performance [15-17]. Therefore, optimization should be carried out on SnBi solders to make them stronger and more durable during application. Microalloying of other minor elements into SnBi solders is the main way to alter the microstructure and mechanical reliability of the solders. For

micro-alloying effects in Sn-Bi solders, previous research has studied the influence on solder microstructure and intermetallic compound growth for different elemental additions into Sn-Bi solders. The addition of Ag into Sn-Bi solders produces Ag_3Sn intermetallic precipitates in the solder matrix, refines the microstructure, and slows down Cu_6Sn_5 growth at the solder-Cu interface during aging [18-21]. Adding Ag into SnBi solders also increases the shear strength [22] and creep resistance [23] of the solder joints. Additions of Cu to Sn-Bi alloys results in the formation of Cu_6Sn_5 particles in the solder matrix and also refines the microstructure [24], as well as increasing the tensile strength and elongation of the solder [25]. Cu additions also increase the creep resistance [26] and shear strength [27] of the solder joints. Research on alloying Sn-Bi solders with Sb [28,29], Ni [30,31], In [32,32], Co [34], and Zn [35,36], has also been reported for assembly with Cu surface finishes. Wang et al. [37] published a review of the literature in 2019 which provides some details of earlier work.

Another one of the most important areas to be examined is intermetallic compound stability and growth with different surface finishes to understand the reliability of low temperature soldering systems, both hybrid and homogeneous because of the introduction of Bi into the system. There has been previous research on intermetallic compound growth with Sn-Bi alloys on different surface finishes, such as Sn-Bi and Sn-Bi-Ag solders on Cu [38-42], ENIG [38,41,43-45], Ni substrates [39,40,45-48], and ENEPIG [38,41,43,49]. Li et al. annealed Sn-Bi solders on Cu [50], Ni [51,52], and ENIG [51,52] at 240°C, 100°C above the Sn-Bi eutectic temperature. For Sn-Bi solders on Cu, intermetallic compounds Cu_6Sn_5 and Cu_3Sn formed at the solder-surface finish interface during 240°C annealing with two different growth rates observed depending on annealing time reflecting a change in mechanism of intermetallic growth [49]. For Sn-Bi solders on Ni substrates, Ni_3Sn_4 forms along the interface during annealing at 240°C [51,52], while Sn-Bi solders in contact with ENIG surface finish result in the formation of Ni_3Sn_4 and Ni_3P intermetallic compounds at the solder-surface finish interface during annealing at 240°C [51,52].

For all the previous research done on SnBi-based solders, the main gap between the work done and the unknown region contains two parts. For the microstructural evolution and intermetallic compound growth study, most of the previous research mainly focused on the intermetallic compound growth at either very high temperature (above the Sn-Bi eutectic temperature) or low application temperatures (room temperature, 85°C, 100°C). There has been little research focused on intermetallic compound growth under harsh, solid-state aging environments (homologous

temperatures > 0.75), or supported by thermodynamic simulation, measurements of the order of intermetallic growth with isothermal annealing, or growth rate of intermetallic compound layer in Sn-Bi solders on different surface finishes. For all the previous study, they focused on mainly the characterization of tensile properties of the alloy itself instead of solder interconnects. For all the mechanical testing on solder interconnects, mainly creep and ball shear testing were conducted, which lacks systematic study on the reliability of the joints, such as monotonic and fatigue loading tests.

The development of SnBi-based low temperature solders contains four generations [53] listed as follows:

- First generation solder is the eutectic 42Sn-58Bi solder;
- Second generation solder is the eutectic 42-58Bi and microalloying additives, such as Ag;
- Third generation solder is a non-eutectic alloy with lower Bi content (49-51wt.%) and multiple microalloying elements at about 2wt.%;
- Fourth generation solder is a near eutectic solder, having higher Bi contents (56-58wt.%) and multiple microalloying elements at about 2wt.%.

Among all the different SnBi-based solders, HRL1 (MacDermid Alpha) as a third generation solder, with Cu, Ag and other microalloying elements, showed much better drop shock resistance and thermal cycling reliability compared to the other first and second generation solders. Therefore, the purpose of this study is to systematically characterize the microstructure evolution of the solder itself, the microstructure evolution in contact with SAC alloys, the intermetallic compound growth on Cu-based and Ni-based surface finishes, as well as the mechanical properties (creep, monotonic, fatigue reliability) of HRL1, and compare the difference between the first generation (Sn58Bi) and second generation (Sn57.6Bi0.4Ag and Sn57Bi1Ag) solders. The purpose of the study is to determine the underlying reason of why HRL1 is superior compared to the traditional SnBi and SnBiAg alloys.

4.3 Experimental

As a starting point in estimating the possible intermetallic compounds and their compositions forming in solder joints during reflow and solid-state annealing, Thermo-Calc 2020a software was

utilized to calculate the solidification paths of Sn-Bi, Sn-Bi-Ag and HRL1 systems using TCSLD3 solder alloys database.

For the characterization of microstructure evolution in hybrid assemblies, two geometries were utilized. First model is the LTS-SAC solder paste mixtures. Sn57.6Bi0.4Ag (KOKI Co Ltd.) and HRL1 (MacDermid Alpha) were mixed with Sn0.7Cu (Nihon Superior) paste. The solder pastes were carefully weighed and stirred by hand followed by a centrifugal mixing to achieve an even distribution of solder particles.The experiments described here were performed with paste mixtures with an overall Bi composition of 30 wt.%. Differential scanning calorimetry (TA Q-100 DSC) was used to measure the heat flow curves as a function of temperature, time, and ramp rate. of different samples. After DSC, all the samples were carefully mounted in epoxy and polished with diamond suspension (Allied High Tech). The second geometry studied is hybrid SnBi-SAC305, SnBiAg-SAC305 and HRL1-SAC305 BGA assemblies by stencil printing (Yamaha YCP10 stencil printing machine), surface mount (Yamaha I-Pulse M-10 pick and place machine) and reflow (BTU Pyramax 125N reflow oven) with the peak reflow temperature of 180°C provided by Alpha Assembly Solutions. Quanta 650 FEG SEM was used to observe the microstructure evolution and Bi diffusion characteristics in all the samples. EDS and EBSD were utilized to study the Bi composition in different parts of the samples, and the Sn grain growth during isothermal hold process.

For the characterization of homogeneous joints, the test specimens consist of eight solder joints connecting two FR4 boards from Bay Area Circuits. Figure 4.4 shows the configuration and dimensions of the test specimens. The FR4 substrates are single layer PCBs with mask-defined copper pads and electroless nickel-immersion gold surface finish (ENIG) or Cu coated with an organic surface preservative (OSP) surface finish. The 730 μm diameter pads are arranged in a 7 x 7, 1:27mm pitch grid. The solder joints were assembled by reflowing 500 μm diameter Sn58Bi or Sn57Bi1Ag solder balls (Scientific Alloys), and HRL1 solder balls (MacDermid Alpha). The samples were assembled by DDM Novastar GF-12HC-HT 3-zone reflow oven. For both alloys, a maximum temperature of 180°C was used with 90 seconds of time above liquidus (139°C). After reflow, the standoff height was measured after cross-section under Quanta 650 FEG SEM for each sample prior to testing. The measured standoff heights ranged between 145 and 165μm. After assembly, the test specimens were stored at -10°C to slow any microstructural aging. To study the microstructure evolution during solid state annealing, the test specimens were annealed at 125°C

for up to 250 hours in Fisher Scientific 725F annealing furnace. After solid state annealing and mechanical reliability tests, metallographic cross-sections were prepared using standard techniques, i. e. mounting in epoxy and polishing using a progression of diamond suspensions on porous polyurethane polishing pads (Allied High Tech). Quanta 650 FEG SEM was used to observe the microstructure evolution and fracture path propagation in all the samples. Measurements of the thickness of intermetallic compound (IMC) layers were performed using ImageJ. Thickness was measured by doing length-average (t=A/l) of IMC layers on multiple SEM images due to the nonuniformity of IMC layers. EDS was utilized to identify different intermetallic compound species as well as elemental segregations in the solder interconnects.

Displacement-controlled shear fatigue tests were performed on the test specimens until failure using a custom-built micro-precision mechanical tester. The test specimen displacement for the tester is measured with a capacitance sensor mounted near the test specimen. The capacitance sensor has a resolution of 7 nm. The capacitance sensor displacement measurement is used for closed-loop control of the tester to ensure that the desired displacement and displacement rate is imposed on the test specimen. This feature is critical for solder characterization due to most solder alloys' viscoplastic behavior at room temperature, i.e., the stress response of solder alloys depend on the applied strain rate. Shear fatigue tests were performed at 30°C. The displacement profile consists of a 0.20 µm/s ramp up (7.7×10^{-4} s^{-1} strain rate) to 39 µm (15% strain) followed by a 200 s dwell, a 0.20 µm/s ramp down (7.7×10^{-4} s^{-1} strain rate) to 0 µm (0% strain), and another 200 s dwell. The displacement profile is inspired by the on/off cycle experienced by some electronics. The displacement profile is repeated until the test specimen has failed or after the test has run for 24 hours. The first ramp up is identical to a monotonic test at $7.7 \times 10\text{-}^{4}$ s^{-1}. The equivalent stress, σ, and equivalent strain, ε, for the test specimens are estimated with:

$$\sigma=(\sqrt{3}\ F)/A$$

$$\varepsilon=\delta/(\sqrt{3}\ h)$$

where F is the measured shear load, A is the total pad area, δ is the shear displacement, and h is the standoff height.

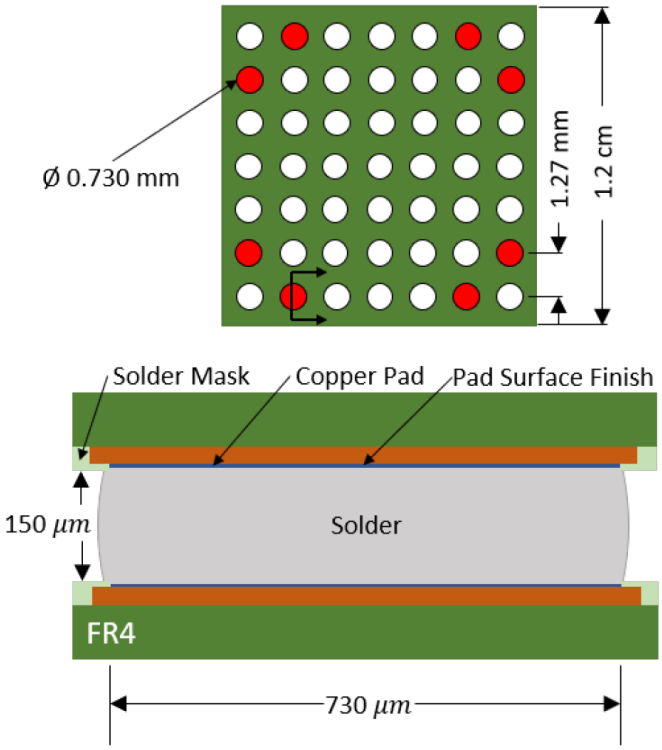

Figure 4.4. Schematic illustration of Sn-58Bi and Sn-57Bi-1Ag solder test specimens. The eight red circles indicate the locations of the solder joints in the top view of the printed circuit board (top). The cross section of an assembled single solder joint (bottom)

4.4 Results and Discussion

4.4.1 Thermodynamic Calculations of HRL1 Solder

Phase equilibrium calculations give insights into the expected phases within the bulk solder during reflow (melting at 180˚C and solidification to room temperature) and subsequent annealing at 125˚C. The solidification paths showing equilibrium phases at different temperatures of Sn57.6Bi0.4Ag and HRL1 are shown in Figure 4.5 below. For eutectic Sn58Bi solder, only (Sn) and Bi phases are present during solidification process. The second generation solders adds Ag into SnBi solder, introducing Ag_3Sn intermetallic compounds into the system as the refining regent, as show in Fig 5. However, Ag_3Sn only starts to precipitate near the eutectic temperature, and no Ag_3Sn are present in the liquid solder at reflow temperature (180°C). For HRL1, more alloying elements and amounts are introduced into the solder (up to 2wt.%), with not only Ag but Cu and other microalloying elements as well. Cu_6Sn_5, Ag_3Sn and other intermetallic compounds form inside the solder not only during solidification process, but at reflow temperature as well. With

more intermetallic compounds present inside the solder, they are expected to refine the microstructure of Sn and Bi further more compared to the first and second generation solders.

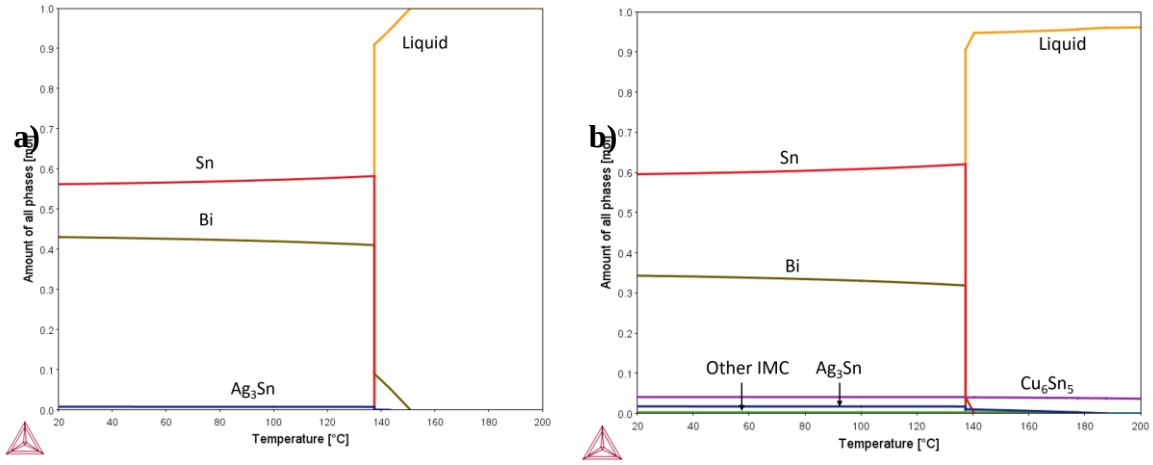

Figure 4.5. Solidification path simulation of a) Sn57.6Bi0.4Ag and b) HRL1 from 20°C to 200°C

4.4.2 Microstructure Evolution of Hybrid Systems during Reflow

In SnBi-SAC hybrid assemblies, SnBi-based solders are in contact with SAC alloys, where a Bi concentration gradient exists between the two solders. Therefore, Bi diffusion into Sn will happen during reflow and solid-state annealing process. Since Bi precipitation and re-distribution in original SAC region may influence the reliability of the hybrid joints, it is important to study the Bi diffusion and precipitation characteristics in hybrid systems during reflow and solid-state aging. To study the microstructure evolution during reflow process, Sn57.6Bi0.4Ag and HRL1 solder pastes were mixed with Sn0.7Cu paste respectively to reach an overall Bi composition of 30wt.%. DSC was then used to simulate the reflow process, with a heating rate of 20°C/min to 165°C, isothermal hold time of up to 4 hours were performed before cool down with a cooling rate of 10°C/min back to room temperature. The microstructure of Sn57.6Bi0.4Ag/Sn0.7Cu and HRL1/Sn0.7Cu mixtures at 165°C without annealing time and 4 hours are shown in Figure 4.6 below. For both solders, Sn grain growth and Sn-Bi eutectic structure development were discovered during annealing. However, due to the larger alloying amount in HRL1, both Sn-Bi eutectic structure and finer Bi precipitates in Sn are much refined than Sn57.6Bi0.4Ag. Finer Bi precipitates and more intermetallic compounds inside bulk solder is an important source for strain hardening, which improves the strength of the HRL1 hybrid joints compared with Sn58Bi and Sn57.6Bi0.4Ag joints.

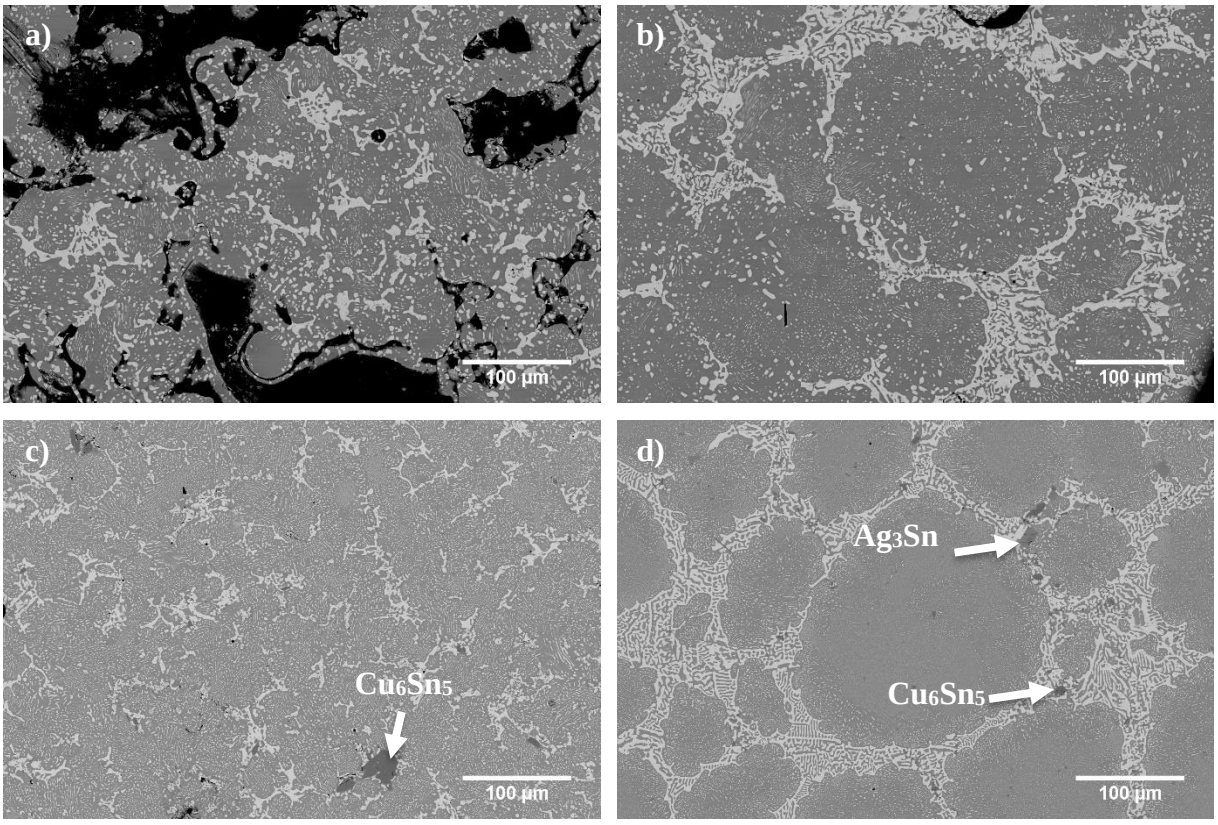

Figure 4.6. Microstructure of a) Sn57.6Bi0.4Ag/Sn0.7Cu solder paste mixtures annealed at 165°C for 0 minute; b) Sn57.6Bi0.4Ag/Sn0.7Cu solder paste mixtures annealed at 165°C for 4 hours; c) HRL1/Sn0.7Cu solder paste mixtures annealed at 165°C for 0 minute and d) HRL1/Sn0.7Cu solder paste mixtures annealed at 165°C for 4 hours

4.4.3 Bi Diffusion and Sn Grain Growth in Hybrid Assemblies during Solid-State Aging

To study the Bi diffusion and Sn grain growth in hybrid joints during solid-state aging process, Sn58Bi and HRL1 were joint with SAC305 and Cu substrates respectively to simulate actual Cu-LTS-SAC305 hybrid joint structures. The samples were aged at 125°C for up to 1500 hours to study the microstructure evolution. The microstructures of Cu-SnBi-SAC305 and Cu-HRL1-SAC305 hybrid assemblies after reflow and solid-state annealing are shown in Figure 4.7 below. For both solders, Sn dissolution from SAC305 to LTS were observed during reflow process, by formation of Sn "dendrites" in the LTS solder region. After aging, Significant Bi diffusion into SAC305 were observed. However, the Bi diffusion is very irregular in Sn for both solders. Higher magnification pictures of Bi diffusion fronts in Cu-SnBi-SAC305 and Cu-HRL1-SAC305 hybrid assemblies are shown in Figure 4.8. For both Sn58Bi and HRL1, both the morphology and composition of Bi in the diffusion zone is very irregular. Two morphologies of Bi were observed

in the diffusion zone: oriented arrays of needle-shaped precipitates in the diffusion zone and non-oriented spheroidal precipitates at diffusion front. EBSD results revealed that oriented arrays of needle-shaped precipitates distribute inside Sn grains, and non-oriented spheroidal precipitates stay at Sn grain boundaries, as shown in Figure 4.9 below. The compositional gradients of Bi inside diffusion zone for both solders both disagree with normal diffusion model. EDS analysis picked up uncommonly high Bi composition at Bi diffusion front, where non-oriented spheroidal precipitates form. A Bi-denuded zone forms between Bi diffusion front and main diffusion zone for both solders.

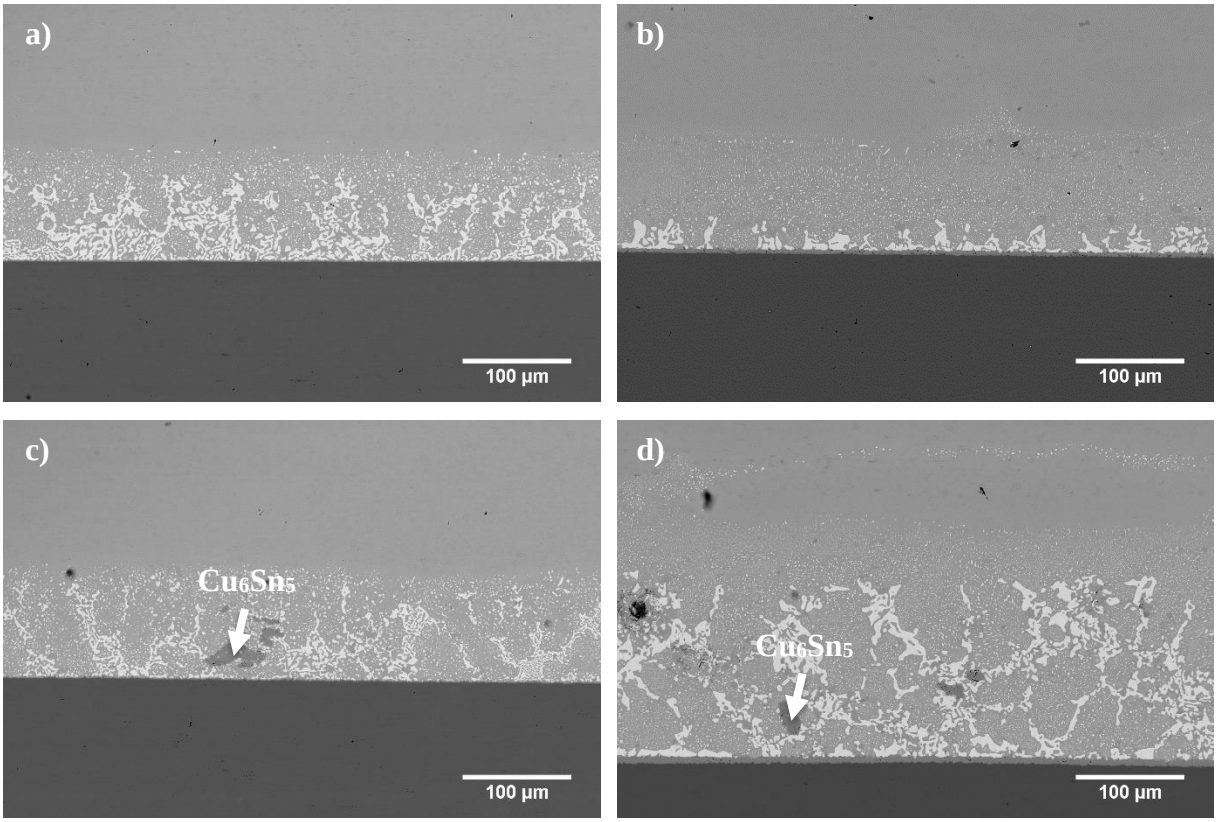

Figure 4.7. Microstructure of a) Cu-Sn58Bi-SAC305 hybrid assemblies after reflow; b) Cu-Sn58Bi-SAC305 hybrid assemblies after 1 week of aging at 125°C; c) Cu-HRL1-SAC305 hybrid assemblies after reflow and d) Cu-HRL1-SAC305 hybrid assemblies after 1 week of aging at 125°C

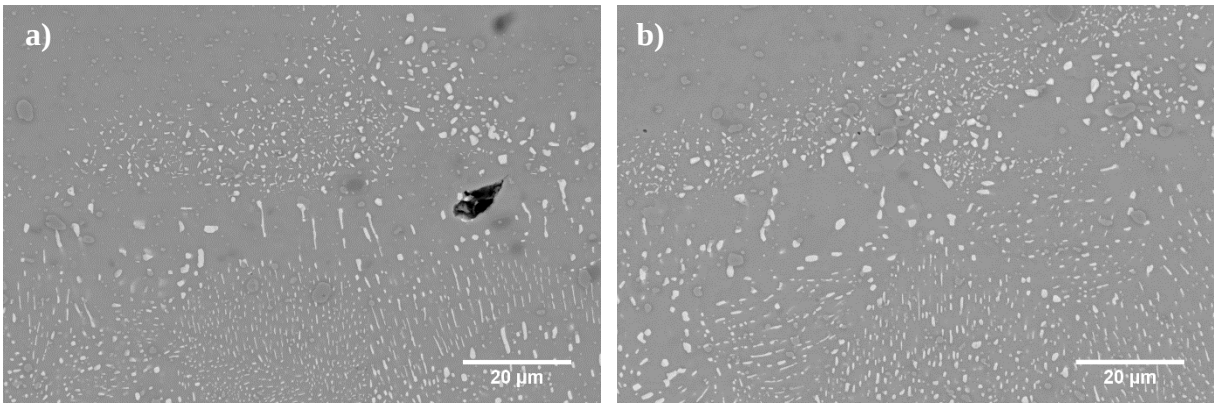

Figure 4.8. Microstructure of Bi diffusion front in a) Cu-Sn58Bi-SAC305 and b) Cu-HRL1-SAC305 hybrid assemblies after 1 week of aging at 125°C

Compared from microstructure, there is no significant difference between Sn58Bi, Sn57.6Bi0.4Ag and HRL1. Therefore, EBSD is required to differentiate the microstructure evolution between the solders during solid-state aging. Sn EBSD mappings of Bi diffusion regions in Cu-Sn58Bi-SAC305 and Cu-HRL1-SAC305 hybrid joints aged at 125°C are shown in Figure 4.9 below. After short time annealing (1 week), significant Sn grain growth are observed in Sn58Bi-SAC305 hybrid joints. HRL1-SAC305 hybrid assemblies on the other hand, still remain refined Sn grain size in Bi diffusion zone. The reason for HRL1 to have a much slower Sn grain growth rate during aging is because of the higher microalloying in HRL1, which generates fine intermetallic compound particles in the bulk solder serving as the grain growth inhibitor. After long time aging (1500 hours), only huge Sn grains exist in both Cu-Sn58Bi-SAC305 and Cu-HRL1-SAC305 hybrid joints and the Sn grain structures become the same for both hybrid joints. This is due to the coarsening of the intermetallic compound particles in bulk HRL1 during long-time aging, which significantly decreases the amount of the intermetallic compound particles in the bulk, as a result, the Sn grain growth inhabitation effect from intermetallic compound particles disappear in HRL1 after long-time aging, which finally unifies the microstructure for both Sn58Bi and HRL1 hybrid assemblies.

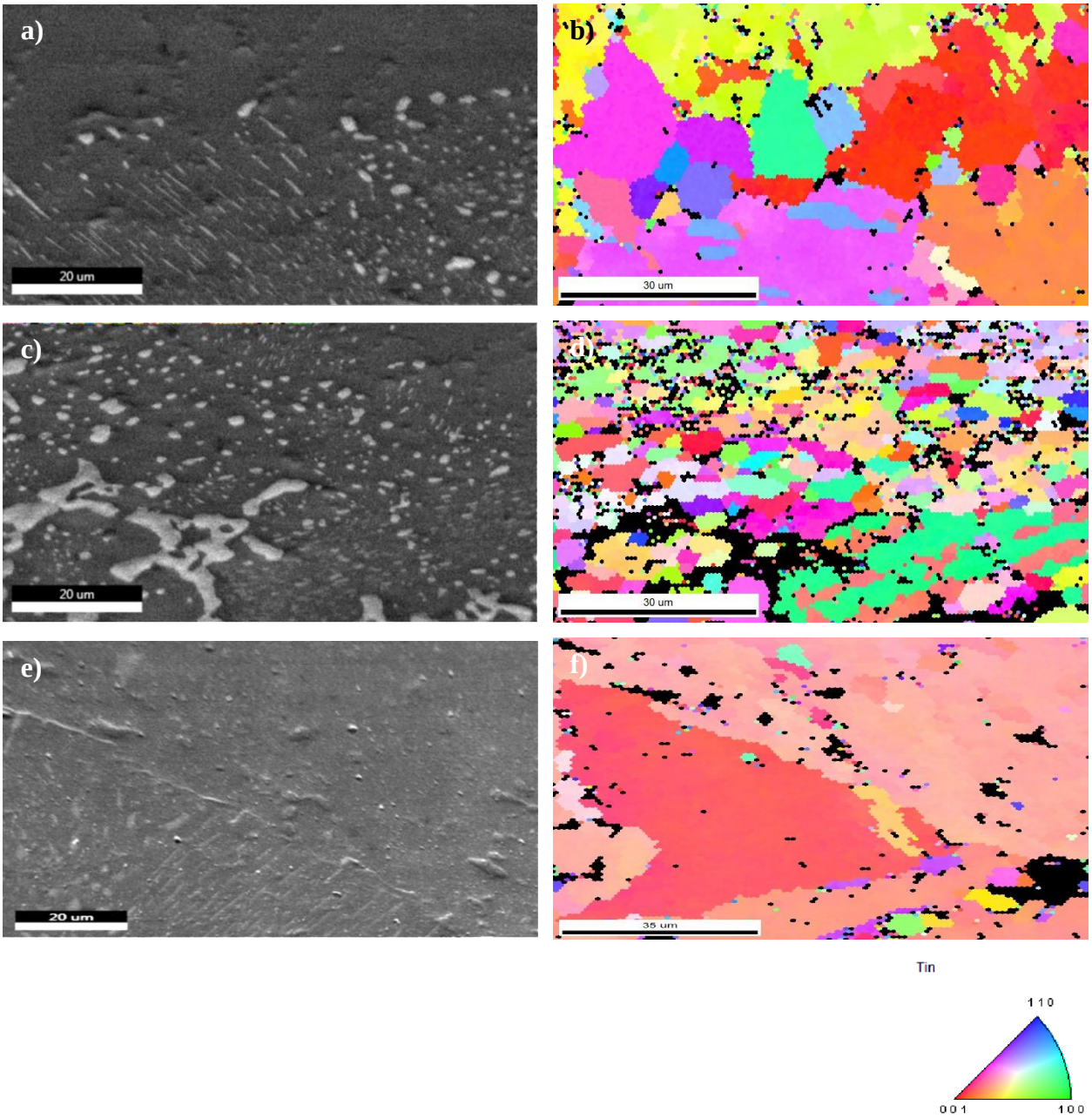

Figure 4.9. a) Microstructure of Bi diffusion front in Cu-Sn58Bi-SAC305 hybrid assemblies after 1 week of aging at 125°C; b) tin EBSD map of a); c) microstructure of Bi diffusion front in Cu-HRL1-SAC305 hybrid assemblies after 1 week of aging at 125°C; d) tin EBSD map of c); e) microstructure of Bi diffusion front in Cu-Sn58Bi-SAC305 hybrid assemblies after 1500 hours of aging at 125°C; f) tin EBSD map of e); g) microstructure of Bi diffusion front in Cu-HRL1-SAC305 hybrid assemblies after 1500 hours of aging at 125°C and h) tin EBSD map of g)

Figure 4.9 continued

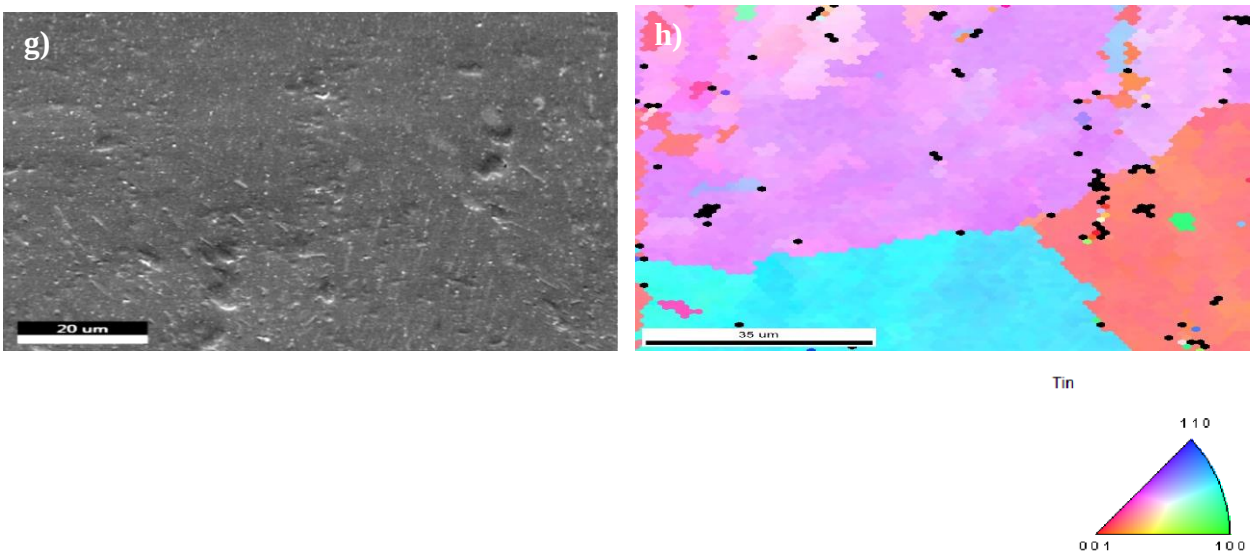

4.4.4 Intermetallic Compound Growth on ENIG Surface Finish of Homogeneous Joints during Reflow

For homogeneous joints, SnBi-based solders are not only in contact with circuit board, but also with the component side, which mostly uses Ni-based surface finishes. Therefore, the study of different intermetallic compound growth on Ni-based surface finishes and their influence on the reliability of the interconnects is also important. Sn58Bi, Sn57Bi1Ag and HRL1 are connected with ENIG surface finish to form ENIG-LTS-ENIG homogeneous joints. The intermetallic compounds found at solder-interface after reflow and aging at 125°C are shown in Figure 4.10 below. After reflow, the Sn58Bi homogeneous joints showed good wetting with ENIG surface finishes. The higher magnification view shows a thin layer of Ni_3Sn_4 at the solder-ENIG interface after reflow. However, after 250 hours of solid-state annealing at 125˚C of Sn58Bi-ENIG solder interconnects, significant $(Ni,Au)Sn_4$ intermetallic growth occured at the interface between the solder and Ni3Sn4, with the thickness increasing to approximately 50µm after 250 hours of annealing, shown in Figure 4.10. The $(Au,Ni)\ Sn_4$ microstructures are largely columnar, with Bi appearing to wet the grain boundaries of the columnar grains. The microstructure of the Sn57Bi1Ag homogeneous joints on ENIG surface finish could be seen in Figure 4.10. Same wetting and Ni_3Sn_4 formation at Sn57Bi1Ag-Ni interface could also be observed after reflow process. After 250 hours of aging, a dual layer of intermetallic compounds which contains $(Au,Ni)Sn_4$ and Ni_3Sn_4 could also be seen at Sn57Bi1Ag-Ni interface, which is the same with

Sn58Bi solder. However, the addition of Ag into SnBi solder significantly slows down the formation and growth of $(Au,Ni)Sn_4$ layer. Compared to 50μm of intermetallic compound layer thickness in annealed ENIG-Sn58Bi-ENIG interconnects, only 4μm of intermetallic compound layer thickness was formed in ENIG-Sn57Bi1Ag-ENIG interconnects after 250 hours of aging. The intermetallic compound species observed at HRL1-ENIG surface is completely different with Sn58Bi and Sn57Bi1Ag joints. The Cu additions in HRL1 forms $(Cu,Ni)_6Sn_5$ intermetallic compound instead of $(Au,Ni)Sn_4$ and Ni_3Sn_4 at solder-Ni interface after reflow and aging process, which is similar as previous research of microalloying of Cu into Sn-Ag solder which transfers $(Au,Ni)Sn_4$ and Ni_3Sn_4 to $(Cu,Ni)_6Sn_5$ on ENIG metallization during annealing [54].

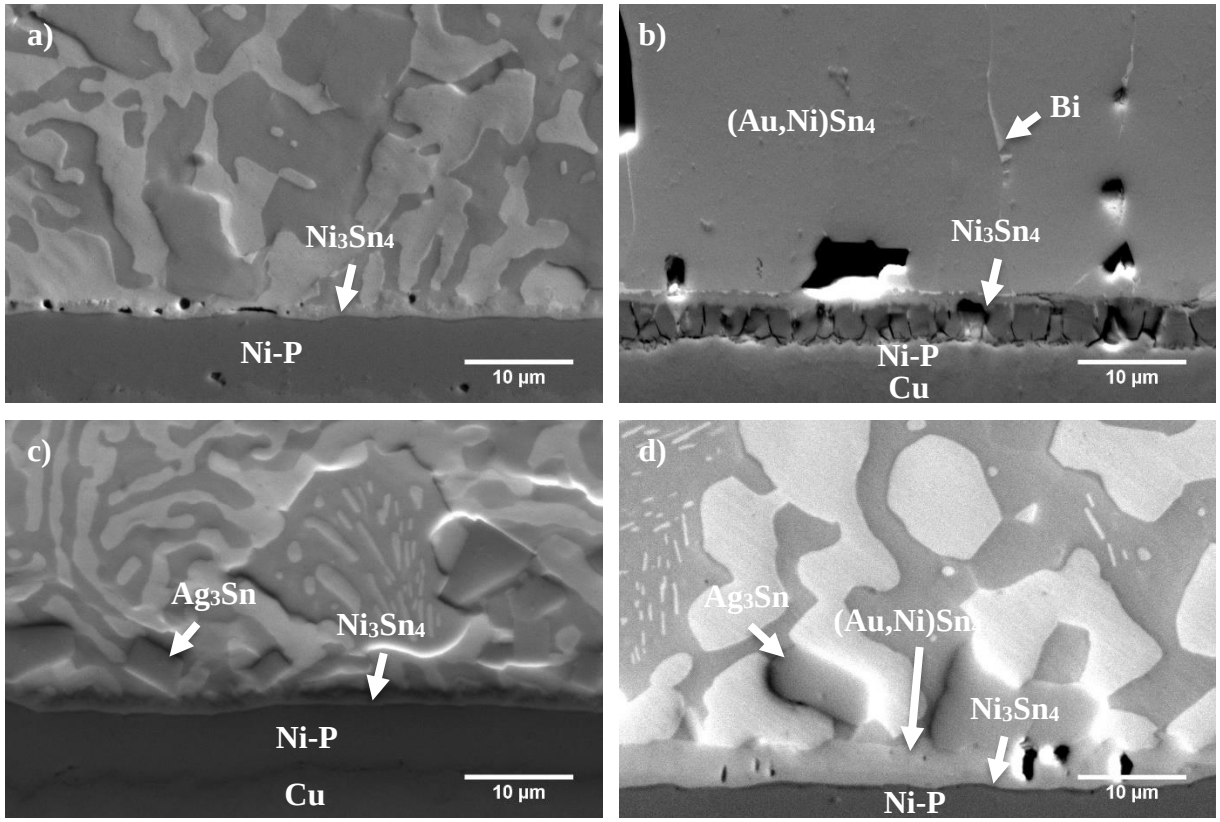

Figure 4.10. Microstructure of a) solder-Ni interface of intermetallic layers of ENIG-Sn58Bi-ENIG solder interconnects after reflow; b) solder-Ni interface of intermetallic layers of ENIG-Sn58Bi-ENIG solder interconnects after 250 hours of solid-state annealing at 125°C; c) solder-Ni interface of ENIG-Sn57Bi1Ag-ENIG solder interconnects after reflow; d) solder-Ni interface of ENIG-Sn57Bi1Ag-ENIG solder interconnects after 250 hours of solid-state annealing at 125°C; e) solder-Ni interface of intermetallic layers of ENIG-HRL1-ENIG solder interconnects after reflow and f) solder-Ni interface of intermetallic layers of ENIG-HRL1-ENIG solder interconnects after 250 hours of solid-state annealing at 125°C

Figure 4.10 continued

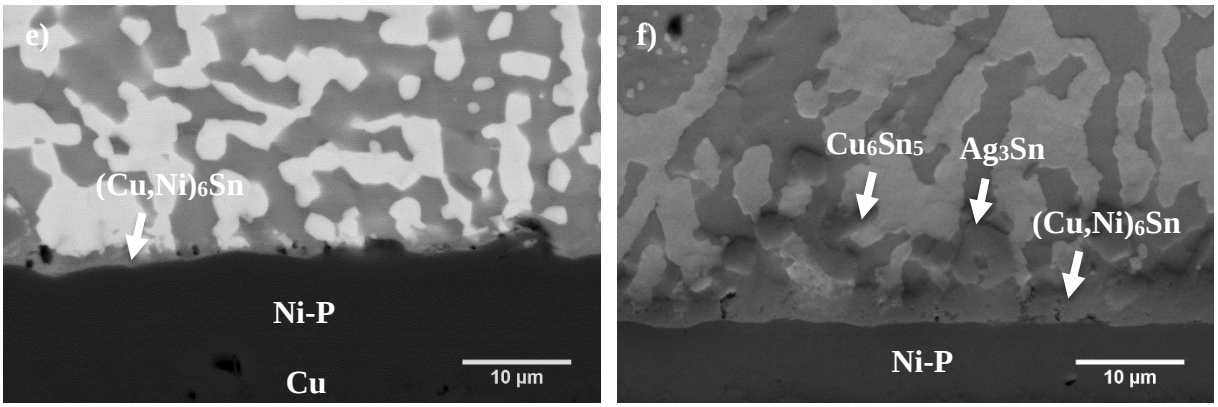

4.4.5 Mechanical Characterization in Homogeneous Interconnects on ENIG & OSP Surface Finishes

For Sn58Bi and Sn57Bi1Ag solder interconnects on ENIG surface finish, $(Au,Ni)Sn_4$ forms after 250 hours of solid-state annealing according to previous discussion. The formation of $(Au,Ni)Sn_4$ significantly embrittles both Sn58Bi and Sn57Bi1Ag solder joints, causing brittle failures inside the intermetallic compound layer, specifically, inside $(Au,Ni)Sn_4$ layer after fatigue loading, as shown in Figure 4.11 below. The N_{50} cycles (numbers of cycles needed for the loading strength of the joint to drop 50%) drop to 0 for both alloys on ENIG surface finish after aging, as shown in Figure 4.14 below. Therefore, gold in ENIG surface finish catalyzed the formation of $(Au,Ni)Sn_4$ during solid-state annealing, which significantly embrittles the Sn58Bi and Sn57Bi1Ag solder joints, causing brittle failures inside the joints. For HRL1-ENIG interconnects, since $(Au,Ni)Sn_4$ is eliminated due to Cu additions, Au embrittlement effect is also completely eliminated for HRL1 joints on ENIG surface finish. The fracture paths in HRL1-ENIG joints after reflow and aging are shown in Figure 4.12 below. Different from brittle fractures in Sn58Bi and Sn57Bi1Ag joints on ENIG, ductile fatigue failures inside bulk HRL1 solder were discovered after reflow and solid-state aging process. N_{50} cycles of aged HRL1-ENIG joints is much higher than aged Sn58Bi and Sn57Bi1Ag on ENIG, with no brittle failures observed. What is more interesting, the fatigue reliability of HRL1 on ENIG becomes better after aging.

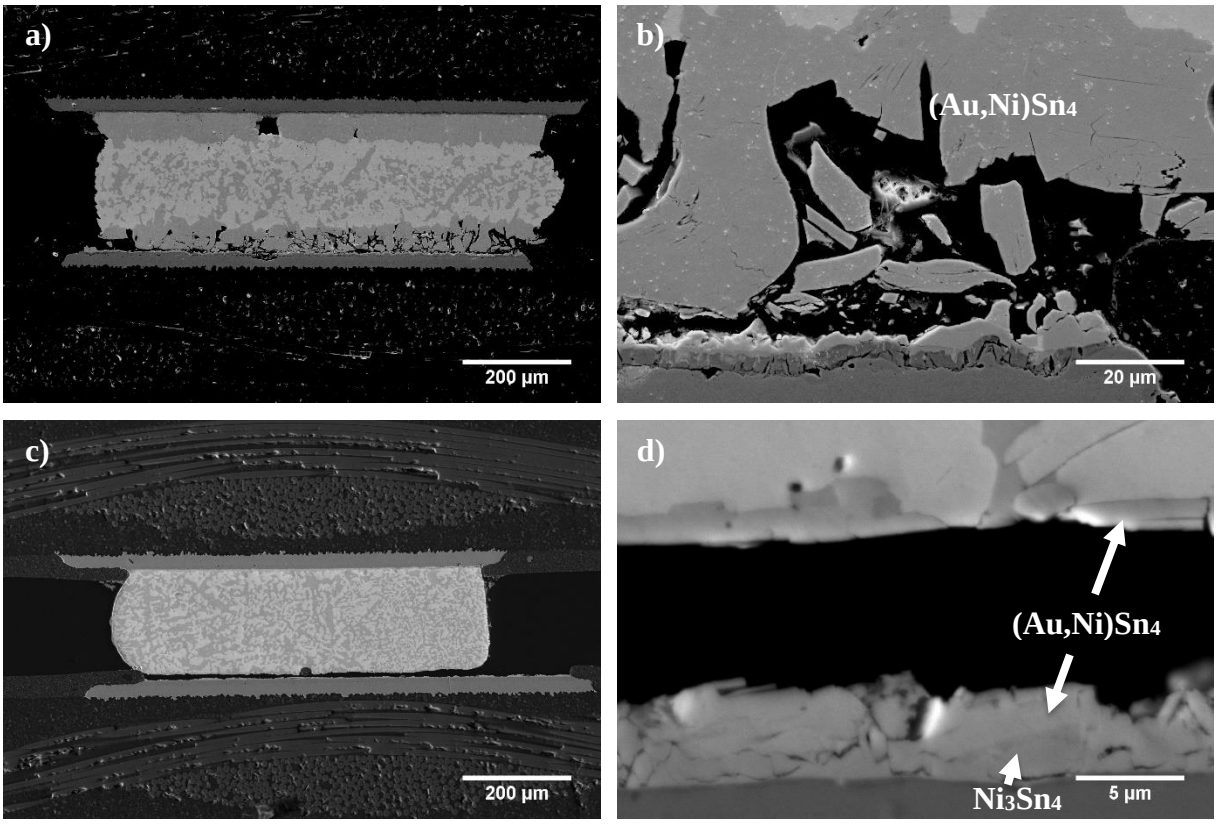

Figure 4.11. Microstructure of a) fatigue-loaded ENIG-Sn58Bi-ENIG solder interconnects after 250°C of solid-state annealing; b) higher magnification image at Sn58Bi-Ni interface of a) showing the details of fractures; c) fatigue-loaded ENIG-Sn57Bi1Ag-ENIG solder interconnects after 250°C of solid-state annealing; and d) higher magnification image at Sn57Bi1Ag-Ni interface of c) showing the details of fractures

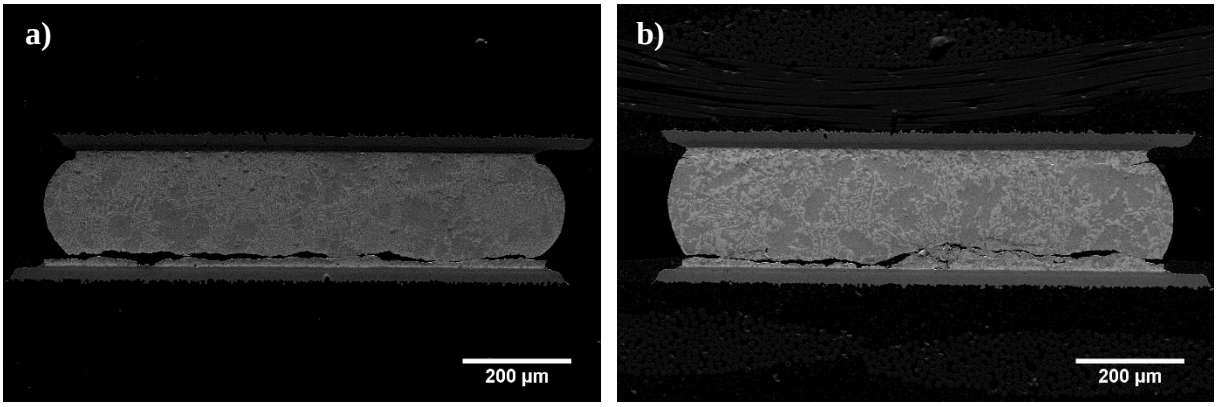

Figure 4.12. Microstructure of fractured a) ENIG-HRL1-ENIG joint after reflow and b) ENIG-HRL1-ENIG joint after 250 hours aging at 125°C

The microstructure of fractured Sn58Bi, Sn57Bi1Ag and HRL1 joints on OSP surface finish is shown in Fig 13. After reflow, ductile fatigue failures were observed in both Sn58Bi and Sn57Bi1Ag joints, with both cracks propagating inside the bulk solder. After aging at 125°C, both solder joints still experience typical fatigue failure, the fracture propagates inside the intermetallic compound layer for aged Sn58Bi joints, and inside bulk solder but very close to the intermetallic compounds for Sm57Bi1Ag joints. The fatigue reliability for both aged solders is much better than the aged ENIG interconnects, since no Au embrittlement takes place on OSP surface finish, as shown in Fig 14 below. However, the fatigue reliability is still much worse than SAC305. Although ductile fatigue failure is also observed in HRL1-OSP joints with the fracture path running inside bulk solder after reflow, after aging at 125°C, ductile fatigue failure is observed in aged HRL1-OSP interconnects and the fracture path still remains inside bulk HRL1 solder, which is different with Sn58Bi and Sn57Bi1Ag. The fatigue reliability of HRL1 is also much better than Sn58Bi and Sn57Bi1Ag on OSP after reflow and solid-state aging, and the fatigue reliability of HRL1 on OSP becomes better after aging, same as HRL1 on ENIG. However, the fatigue reliability of HRL1 is still not as good as SAC305 on OSP, which has the N_{50} value of nearly 80 cycles.

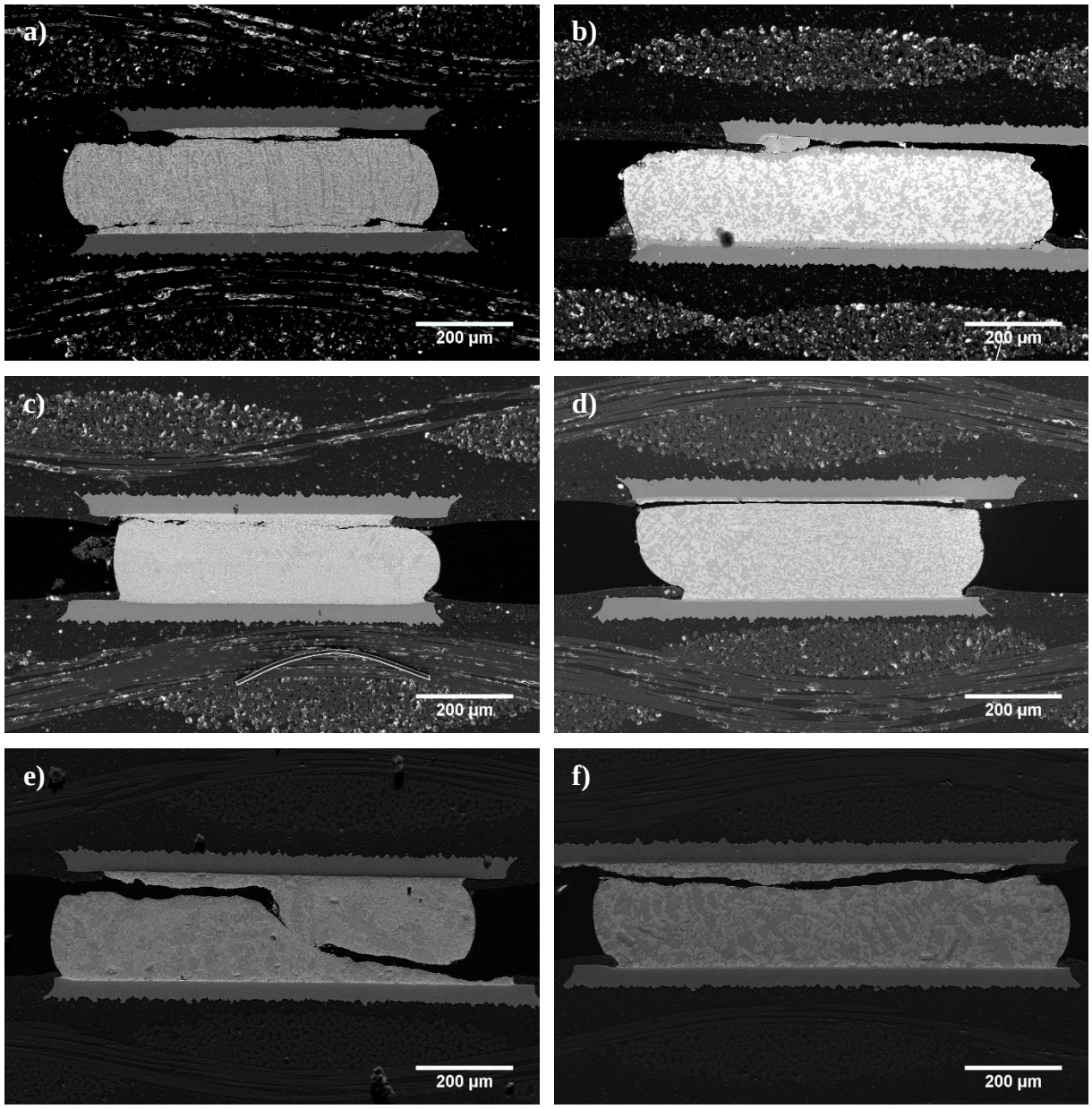

Figure 4.13. Microstructure of fractured a) OSP-Sn58Bi-OSP after reflow; b) OSP-Sn58Bi-OSP after 250 hours aging at 125°C; c) OSP-Sn57Bi1Ag-OSP after reflow; d) OSP-Sn57Bi1Ag-OSP after 250 hours aging at 125°C solder interconnects after fatigue testing; e) OSP-HRL1-OSP after reflow and f) OSP-HRL1-OSP after 250 hours aging at 125°C

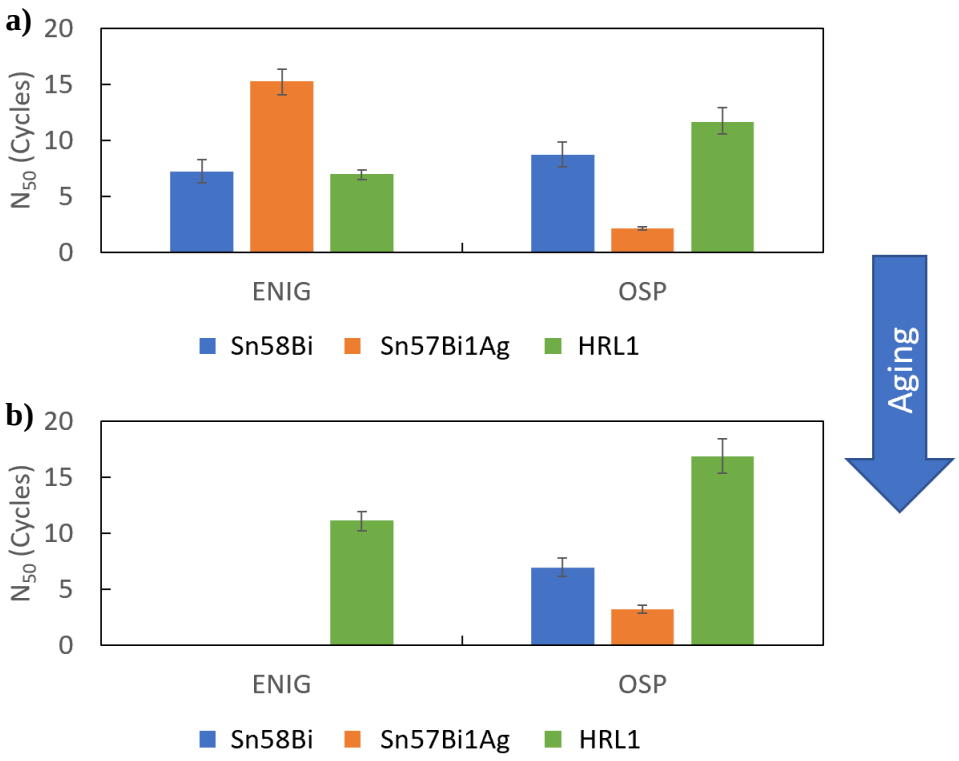

Figure 4.14. Fatigue reliability and N_{50} cycles for Sn58Bi, Sn57Bi1Ag and HRL1 on ENIG and OSP surface finishes after a) reflow and b) 250 hours of aging at 125°C

4.5 Conclusions

SnBi low temperature solders are considered as a promising candidate as substituting traditional SAC alloys to prevent component warpage in the future electronics industry. Thermodynamics calculation, Bi diffusion, intermetallic growth and fatigue reliability study were carried out in this study to understand the microstructural evolution characteristics and mechanical properties of Sn58Bi, Sn57Bi1Ag and HRL1 solders in homogeneous and hybrid joints. The following conclusions could be drawn from this study:

- HRL1 shows significant suppression of Bi precipitation & eutectic Bi coarsening during reflow, two-phase annealing & solid-state annealing, which provides more precipitate strengthening than Sn58Bi and Sn57.6Bi0.4Ag in hybrid assemblies.
- HRL1 shows significant suppression of Sn grain growth in hybrid systems during reflow, the beginning of solid-state annealing and after quite a long time of solid-state annealing due to

fine intermetallic particles inside HRL1 due to microalloying additions, which serve as Sn grain growth inhibitor during aging.

- Microstructure evolution of Bi, Sn and intermetallic compounds in the hybrid systems eventually becomes indistinguishable in Sn58Bi, Sn57.6Bi0.4Ag and HRL1 systems after long-time annealing due to the coarsening of intermetallic compounds in HRL1, but HRL1 shows significantly slower coarsening.
- HRL1 is not affected by Au embrittlement in contact with ENIG surface finish due to Cu additions and elimination of $(Au,Ni)Sn_4$ on ENIG surface finish, and shows significantly better fatigue reliability than Sn58Bi & Sn57Bi1Ag on both OSP and ENIG surface finishes, with even better fatigue reliability after solid-state aging process for both surface finishes. However, the fatigue reliability of HRL1 is still not as good as SAC305.

4.6 Acknowledgment

The authors want to acknowledge MacDermid Alpha for the grant on supporting this research.

4.7 References

[1] Bath, J., Garcia, R., Uchida, N., Takahashi, H., Clark, G., & Itoh, M. (2009). Investigation and development of tin-lead and lead-free solder pastes to reduce the head-in-pillow component soldering defect. SMTA International Proceedings 2009.

[2] Boettinger, W. J., Handwerker, C. A., Newbury, B., Pan, T. Y., & Nicholson, J. M. (2002). Mechanism of fillet lifting in Sn-Bi alloys. Journal of electronic materials, 31(5), 545-550.

[3] Henshall, Gregory, Jasbir Bath, and Carol A. Handwerker, eds. Lead-free solder process development. John Wiley & Sons, 2011.

[4] Hua, F., Mei, Z., & Glazer, J. (1998, May). Eutectic Sn-Bi as an alternative to Pb-free solders. In 1998 Proceedings. 48th Electronic Components and Technology Conference (Cat. No. 98CH36206) (pp. 277-283). IEEE.

[5] Ferrer, E., & Holder, H. (2003, March). 57Bi-42Sn-1Ag: A Lead Free, Low Temperature Solder for the Electronic Industry. In JEDEX Conference, San Jose, CA, March (pp. 22-25).

[6] Aspandiar, R., Byrd, K., Tang, K. K., Campbell, L., & Mokler, S. (2015, February). Investigation of low temperature solders to reduce reflow temperature, improve SMT yields and realize energy savings. In Proceedings of the 2015 APEX Conference.

[7] Chen, O. H., Byrd, K., Mokler, S., Tang, K. K., & Aspandiar, R. (2015, May). Comparison of the Mechanical Shock/Drop Reliability of Flip Chip BGA (FCBGA) Solder Joints Formed by Soldering with Low Temperature BiSn-Based Resin Reinforced Solder Pastes. In Proceedings of the International Conference on Soldering and Reliability.

[8] Chen, O. H., Molina, A., Aspandiar, R., Byrd, K., Mokler, S., & Tang, K. K. (2015, September). Mechanical shock and drop reliability evaluation of the BGA solder joint stack-ups formed by reflow soldering SAC solder balls BGAs with BiSnAg and resin reinforced BiSn-based solder pastes. In Proceedings of SMTA International (pp. 215-222).

[9] Mokler, S., Aspandiar, R., Byrd, K., Chen, O., Walwadkar, S., Tang, K. K., ... & Sane, S. (2016, September). The application of Bi-based solders for low temperature reflow to reduce cost while improving SMT yields in client computing systems. In Proceedings of SMTA International (pp. 318-326).

[10] Silva, B. L., Xavier, M. G., Garcia, A., & Spinelli, J. E. (2017). Cu and Ag additions affecting the solidification microstructure and tensile properties of Sn-Bi lead-free solder alloys. Materials Science and Engineering: A, 705, 325-334.

[11] Sahasrabudhe, S., Mokler, S., Renavikar, M., Sane, S., Byrd, K., Brigham, E., ... & Parupalli, S. (2018, May). Low Temperature Solder-A Breakthrough Technology for Surface Mounted Devices. In 2018 IEEE 68th Electronic Components and Technology Conference (ECTC) (pp. 1455-1464). IEEE.

[12] Lee, Byeong-Joo, Chang-Seok Oh, and Jae-Hyeok Shim. "Thermodynamic assessments of the Sn-In and Sn-Bi binary systems." Journal of electronic materials 25.6 (1996): 983-991.

[13] Wang, J., Wen, L., Zhou, J., & Chung, M. (2011, December). Mechanical properties and joint reliability improvement of Sn-Bi alloy. In 2011 IEEE 13th Electronics Packaging Technology Conference (pp. 492-496). IEEE.

[14] Ribas, M., Chegudi, S., Kumar, A., Pandher, R., Raut, R., Mukherjee, S., ... & Singh, B. (2013, December). Development of low-temperature drop shock resistant solder alloys for handheld devices. In 2013 IEEE 15th Electronics Packaging Technology Conference (EPTC 2013) (pp. 48-52). IEEE.

[15] “Lead-Free Solder Project Final Report”. Report 0401RE96, National Center for Manufacturing Sciences, May (1997).

[16] Mei, Z., Holder, H. A., & Vander Plas, H. A. (1996). Low-temperature solders. Hewlett Packard Journal, 47, 91-98.

[17] Seyyedi, J. (1993). Thermal fatigue of low-temperature solder alloys in insertion mount assembly.

[18] Dong, W., Shi, Y., Xia, Z., Lei, Y., & Guo, F. (2008). Effects of trace amounts of rare earth additions on microstructure and properties of Sn-Bi-based solder alloy. Journal of Electronic Materials, 37(7), 982-991.

[19] Myung, W. R., Ko, M. K., Kim, Y., & Jung, S. B. (2015). Effects of Ag content on the reliability of LED package component with Sn–Bi–Ag solder. Journal of Materials Science: Materials in Electronics, 26(11), 8707-8713.

[20] Guan, Z. M., Liu, G. X., & Liu, T. (2000). Kinetics of interface reaction in 40Sn-Bi/Cu and 40Sn-Bi-2Ag/Cu systems during aging in solid state. IEEE transactions on advanced packaging, 23(4), 737-742.

[21] Suganuma, K., Sakai, T., Kim, K. S., Takagi, Y., Sugimoto, J., &Ueshima, M. (2002). Thermal and mechanical stability of soldering QFP with Sn-Bi-Ag lead-free alloy. IEEE Transactions on electronics packaging manufacturing, 25(4), 257-261.

[22] Sun, H., Li, Q., & Chan, Y. C. (2014). A study of Ag additive methods by comparing mechanical properties between Sn57. 6Bi0. 4Ag and 0.4 wt% nano-Ag-doped Sn58Bi BGA solder joints. Journal of Materials Science: Materials in Electronics, 25(10), 4380-4390.

[23] Shalaby, R. M. (2013). Effect of silver and indium addition on mechanical properties and indentation creep behavior of rapidly solidified Bi–Sn based lead-free solder alloys. Materials Science and Engineering: A, 560, 86-95.

[24] Lai, Z., & Ye, D. (2016). Microstructure and Properties of Sn-10Bi-xCu Solder Alloy/Joint. Journal of Electronic Materials, 45(7), 3702-3711.

[25] Shen, J., Wu, C., & Li, S. (2012). Effects of rare earth additions on the microstructural evolution and microhardness of Sn30Bi0. 5Cu and Sn35Bi1Ag solder alloys. Journal of Materials Science: Materials in Electronics, 23(1), 156-163.

[26] Shen, L., Tan, Z. Y., & Chen, Z. (2013). Nanoindentation study on the creep resistance of SnBi solder alloy with reactive nano-metallic fillers. Materials Science and Engineering: A, 561, 232-238.

[27] Shen, J., Pu, Y., Yin, H., & Tang, Q. (2015). Effects of Cu, Zn on the wettability and shear mechanical properties of Sn-Bi-based lead-free solders. Journal of Electronic Materials, 44(1), 532-541.

[28] Zhang, C., Liu, S. D., Qian, G. T., Jian, Z. H. O. U., & Feng, X. U. E. (2014). Effect of Sb content on properties of Sn—Bi solders. Transactions of Nonferrous Metals Society of China, 24(1), 184-191.

[29] Sakuyama, S., Akamatsu, T., Uenishi, K., & Sato, T. (2009). Effects of a third element on microstructure and mechanical properties of eutectic Sn–Bi solder. Transactions of The Japan Institute of Electronics Packaging, 2(1), 98-103.

[30] Mokhtari, O., & Nishikawa, H. (2016). Correlation between microstructure and mechanical properties of Sn–Bi–X solders. Materials Science and Engineering: A, 651, 831-839.

[31] Mokhtari, O., & Nishikawa, H. (2014). Effects of In and Ni addition on microstructure of Sn-58Bi solder joint. Journal of electronic materials, 43(11), 4158-4170.

[32] Chen, X., Xue, F., Zhou, J., & Yao, Y. (2015). Effect of In on microstructure, thermodynamic characteristic and mechanical properties of Sn–Bi based lead-free solder. Journal of Alloys and Compounds, 633, 377-383.

[33] Li, Q., Ma, N., Lei, Y., Lin, J., Fu, H., & Gu, J. (2016). Characterization of low-melting-point Sn-Bi-In lead-free solders. Journal of Electronic Materials, 45(11), 5800-5810.

[34] Huang, Y. C., & Chen, S. W. (2011). Effects of Co alloying and size on solidification and interfacial reactions in Sn-57 wt.% Bi-(Co)/Cu couples. Journal of electronic materials, 40(1), 62-70.

[35] Zhou, S., Mokhtari, O., Rafique, M. G., Shunmugasamy, V. C., Mansoor, B., & Nishikawa, H. (2018). Improvement in the mechanical properties of eutectic Sn58Bi alloy by 0.5 and 1 wt% Zn addition before and after thermal aging. Journal of Alloys and Compounds, 765, 1243-1252.

[36] Mokhtari, O., Zhou, S., YC, C., & Nishikawa, H. (2016). Effect of Zn addition on interfacial reactions between Sn-Bi solder and Cu substrate. Materials Transactions, 57(8), 1272-1276.

[37] Wang, F., Chen, H., Huang, Y., Liu, L., & Zhang, Z. (2019). Recent progress on the development of Sn–Bi based low-temperature Pb-free solders. Journal of Materials Science: Materials in Electronics, 30(4), 3222-3243.

[38] Kim, J. H., Lee, Y. C., Lee, S. M., & Jung, S. B. (2014). Effect of surface finishes on electromigration reliability in eutectic Sn–58Bi solder joints. Microelectronic engineering, 120, 77-84.

[39] Liu, P. L., & Shang, J. K. (2005). Fracture of Sn-Bi/Ni (P) interfaces. Journal of materials research, 20(4), 818-826.

[40] Yoon, J. W., Lee, C. B., & Jung, S. B. (2002). Interfacial reactions between Sn-58 mass% Bi eutectic solder and (Cu, electroless Ni-P/Cu) substrate. Materials transactions, 43(8), 1821-1826.

[41] Lee, S. M., Yoon, J. W., & Jung, S. B. (2015). Interfacial reaction and mechanical properties between low melting temperature Sn–58Bi solder and various surface finishes during reflow reactions. Journal of Materials Science: Materials in Electronics, 26(3), 1649-1660.

[42] Zou, H. F., Zhang, Q. K., & Zhang, Z. F. (2012). Interfacial microstructure and mechanical properties of Sn-Bi/Cu joints by alloying Cu substrate. Materials Science and Engineering: A, 532, 167-177.

[43] Myung, W. R., Kim, Y., Kim, K. Y., & Jung, S. B. (2016). Drop reliability of epoxy-contained Sn-58 wt.% Bi solder joint with ENIG and ENEPIG surface finish under temperature and humidity test. Journal of Electronic Materials, 45(7), 3651-3658.

[44] Chen, L. T., & Chen, C. M. (2006). Electromigration study in the eutectic Sn-Bi solder joint on the Ni/Au metallization. Journal of materials research, 21(4), 962-969.

[45] Young, B. L., Duh, J. G., & Jang, G. Y. (2003). Compound formation for electroplated Ni and electroless Ni in the under-bump metallurgy with Sn-58Bi solder during aging. Journal of electronic materials, 32(12), 1463-1473.

[46] Tao, W. H., Chen, C., Ho, C. E., Chen, W. T., & Kao, C. R. (2001). Selective interfacial reaction between Ni and eutectic BiSn lead-free solder. Chemistry of materials, 13(3), 1051-1056.

[47] Wang, J., Liu, H. S., Liu, L. B., & Jin, Z. P. (2006). Interfacial reaction between Sn-Bi alloy and Ni substrate. Journal of electronic materials, 35(10), 1842-1847.

[48] Chiu, M. Y., Chang, S. Y., Tseng, Y. H., Chan, Y. C., & Chuang, T. H. (2002). Characterization of intermetallic compounds formed during the interfacial reactions of liquid Sn and Sn-58Bi solders with Ni substrates. ZeitschriftfürMetallkunde, 93(3), 248-252.140: SnAgCu, ENIG, IMC

[49] Pun, K. P., Islam, M. N., Rotanson, J., Cheung, C. W., & Chan, A. H. (2018). Enhancement of Sn-Bi-Ag Solder Joints with ENEPIG Surface Finish for Low-Temperature Interconnection. Journal of Electronic Materials, 47(9), 5191-5202.

[50] Li, J. F., Mannan, S. H., Clode, M. P., Whalley, D. C., & Hutt, D. A. (2006). Interfacial reactions between molten Sn–Bi–X solders and Cu substrates for liquid solder interconnects. Acta Materialia, 54(11), 2907-2922.

[51] Li, J., Mannan, S. H., Clode, M. P., Liu, C., Chen, K., Whalley, D. C., ... & Conway, P. P. (2008). Interfacial reaction between molten Sn-Bi based solders and electroless Ni-P coatings for liquid solder interconnects. IEEE Transactions on Components and Packaging Technologies, 31(3), 574-585.

[52] Li, J. F., Mannan, S. H., Clode, M. P., Chen, K., Whalley, D. C., Liu, C., & Hutt, D. A. (2007). Comparison of interfacial reactions of Ni and Ni–P in extended contact with liquid Sn–Bi-based solders. Actamaterialia, 55(2), 737-752.

[53] Ribas, M., Kumar, A., Augustine P., Choudhury, P., & Sarkar S. (2020). High-reliability, fourth generation low-temperature solder alloys. SMTA International Proceedings 2020, 364-372.

[54] Belyakov, S. A., & Gourlay, C. M. (2016). The Influence of Cu on Metastable NiSn 4 in Sn-3.5 Ag-xCu/ENIG Joints. Journal of Electronic Materials, 45(1), 12-20.

PUBLICATIONS

1. Fan Y., Wu Y., Dale T.F., Achar S., Greene C. V., Badwe N. U., Aspandiar R. F., Blendell J. E., Subbarayan G., & Handwerker C. A. (2021). Influence of Pad Surface Finish on the Microstructure Evolution and Intermetallic Compound Growth in Homogeneous Sn-Bi and Sn-Bi-Ag Solder Interconnects. Journal of Electronic Materials. Submitted.
2. Fan Y., Wu Y., Dale T.F., Achar S., Badwe N. U., Aspandiar R. F., Blendell J. E., Subbarayan G., & Handwerker C. A. (2020). Intermetallic Compound Growth and Gold Embrittlement Effect in Sn-Bi Low Temperature Solders in Contact with Electroless Nickel Emersion Gold (ENIG) Surface Finish. SMTAI 2020 Proceedings.
3. Bath J., Joshi S., Segura R., Huynh V., Boguski R., Fan Y., & Handwerker C. A. (2020). Evaluations on the Mixing and Reliability Testing of Tin-Bismuth Pastes with SnAgCu BGA Components and Reliability Failure Analysis Comparing CT (Computed Tomography) Inspection and Cross-Sectioning. IPC APEX 2020 Conference Proceedings.
4. Fan, Y., Wu, Y., Blendell, J. E., Badwe, N. U., & Handwerker, C. A. (2019). Thermodynamic and Kinetic Effects on Microstructure Evolution in Hybrid Low Temperature Solder/High-Sn Solder Joints. 2019 6th International Workshop on Low Temperature Bonding for 3D Integration (LTB-3D) pp. 23-23. DOI: 10.23919/LTB-3D.2019.8735212.